PNL-6708
UC-261

18 E

Subcontractor Report

Tethersonde and Kite Anemometer Evaluation

W. Y. Chow
R. H. Kirchhoff
University of Massachusetts

J. R. Connell, PNL Project Manager

October 1988

Prepared by the University of Massachusetts
for Pacific Northwest Laboratory
under Contract DE-AC06-76RLO 1830
with the U.S. Department of Energy

Battelle

PNL-6708

DISCLAIMER

This report was prepared as an account of work sponsored by an agency of the United States Government. Neither the United States Government nor any agency thereof, nor Battelle Memorial Institute, nor any or their employees, makes any warranty, expressed or implied, or assumes any legal liability or responsibility for the accuracy, completeness, or usefulness of any information, apparatus, product, or process disclosed, or represents that its use would not infringe privately owned rights. Reference herein to any specific commercial product, process, or service by trade name, trademark, manufacturer, or otherwise does not necessarily constitute or imply its endorsement, recommendation, or favoring by the United States Government or any agency thereof, or Battelle Memorial Institute. The views and opinions of authors expressed herein do not necessarily state or reflect those of the United States Government or any agency thereof.

PACIFIC NORTHWEST LABORATORY
operated by
BATTELLE MEMORIAL INSTITUTE
for the
UNITED STATES DEPARTMENT OF ENERGY
under Contract DE-AC06-76RLO 1830

Printed in the United States of America
Available from
National Technical Information Service
United States Department of Commerce
5285 Port Royal Road
Springfield, Virginia 22161

NTIS Price Codes
Microfiche A01

Printed Copy

Pages	Price Codes
001-025	A02
026-050	A03
051-075	A04
076-100	A05
101-125	A06
126-150	A07
151-175	A08
176-200	A09
201-225	A10
226-250	A11
251-275	A12
276-300	A13

3 3679 00056 0773

PNL-6708
UC-261

TETHERSONDE AND KITE ANEMOMETER EVALUATION

W. Y. Chow
R. H. Kirchhoff

University of Massachusetts
Amherst, Massachusetts

J. R. Connell, PNL Project Manager

October 1988

Prepared by the University of Massachusetts
for Pacific Northwest Laboratory
under Contract DE-AC06-76RLO 1830
with the U.S. Department of Energy
Agreement B-M2765-A-E

Pacific Northwest Laboratory
Richland, Washington 99352

SUMMARY

The responses of kite anemometers and tethersonde balloons to the dynamics of the wind are investigated in this study. A three-phase effort of theoretical development, experimental measurement, and comparison of data and theory was undertaken to provide further understanding of how a kite or balloon responds to atmospheric turbulence. Understanding the effect on wind velocity measurements obtained using these instruments is important to their use in, for example, identifying optimum wind turbine sites.

The theoretical development included 1) an extension of double theodolite theory, to provide a mechanism for calculating instrument displacement, and 2) linear small perturbation analysis of the effect of atmospheric turbulence on kite or balloon motion. The results of the small perturbation analyses were response equations that analyze the movement of the kite or balloon as a function of the mean elevation angle of the kite or balloon and turbulence parameters of the wind. The response equations provide the ratio of the fluctuating string tension to the mean string tension (for the kite) and the fluctuating elevation angle for the kite and balloon.

In the experimental phase, kite and balloon anemometers were flown at the Goodnoe Hills wind turbine site. In addition to the wind data measured by the airborne anemometers, a nearby meteorological tower recorded wind direction and speed. Two 8-mm cameras simultaneously recorded the position of the kite or balloon. The film records were digitized; these digital data provide a measure of kite or balloon displacement. The meteorological data recorded by the airborne and tower anemometers and the digitized data were next compared with the theoretical equations. The comparison of experimental data and theoretical expectations was a valuable one. The experimental data and the response equations for the kite did not correlate; the kite moved in an unpredictable path throughout the period of record and thus the fluctuating tension in the kite string and the fluctuating kite elevation angle could not be used to measure the atmospheric turbulence. The vortex shedding effect on the bluff-body-shaped kite is suspected of causing the erratic motion of the kite. The response equations and the linear small perturbation analysis were not able to describe the vortex-shedding effect.

The motion of the tethersonde balloon was successfully predicted by the perturbation analysis. The cup anemometer suspended below the balloon was not successful in measuring the atmospheric wind; however, the fact that the balloon motion could be successfully predicted by theory is an important step in increasing knowledge about the effect of atmospheric turbulence on balloon anemometers.

ACKNOWLEDGMENTS

The authors wish to acknowledge the extensive efforts of PNL staff who contributed to the completion of this project. Principal among these people is Dr. James Connell, whose interest in examining the usefulness of kite and balloon-borne anemometers kept the study active over several years, who designed, directed, and implemented the experiments, and who guided the analysis and conclusions described in this document. Vic Morris and Bernie Holst performed the field experiments. In addition, Elizabeth Owczarski and Ruth Keefe provided editing and word processing and polished the final report into its present form.

NOMENCLATURE

Symbol	Meaning	SI Units
C	constant	
C_d	drag coefficient	
$C_{d,\alpha}$	derivative of C_d with respect to α	
C_l	lift coefficient	
$C_{l,\alpha}$	derivative of C_l with respect to α	
F_b	buoyancy force	N
F_d	drag force	N
F_l	lift force	N
h	height	m
l	tether length	m
L	distance between two cameras	m
N	number of data points	
Q	wind speed magnitude	m/s
R	sampling rate	
R_{ab}	cross correlation between a and b	
s	displacement	m
S	Strouhal number (dimensionless)	
t'	fluctuating tension	N
T	tension	N
u	horizontal fluctuating wind speed	m/s
U	mean wind speed	m/s
v	vertical fluctuating wind speed	m/s
V	kite or balloon velocity	m/s
w	lateral fluctuating wind speed	m/s
z_o	roughness height	m
α	angle of attack	deg
θ	elevation angle	deg
ψ	azimuth angle	deg
ρ	density	kg/m^3
ϕ	bridle angle	deg
δ	standard deviation	
w	fluctuating kite frequency	Hz

CONTENTS

SUMMARY iii

ACKNOWLEDGMENTS v

NOMENCLATURE vii

1.0 INTRODUCTION 1.1

2.0 EXTENDED OOUBLE THEODOLITE THEORY 2.1

3.0 RESPONSE THEORY OF KITE TO TURBULENCE: TWO APPROACHES 3.1

3.1 FIRST APPROACH: RESPONSE EQUATION FOR t'/T 3.1

3.1.1 Steady-State Analysis 3.1

3.1.2 Dynamic Analysis 3.2

3.2 SECONO APPROACH: RESPONSE EQUATION FOR θ' 3.7

4.0 RESPONSE THEORY OF A TETHERSONDE BALLOON TO TURBULENCE 4.1

4.1 STEADY-STATE ANALYSIS 4.2

4.2 DYNAMIC ANALYSIS 4.5

5.0 KITE EXPERIMENTS AND RESULTS 5.1

5.1 SPECIAL ANALYSIS 5.2

5.2 ANALYSIS OF EXPERIMENTAL RESULTS 5.3

5.3 CONCLUSIONS 5.31

6.0 BALLOON EXPERIMENTS AND RESULTS 6.1

6.1 INTRODUCTION 6.1

6.2 ANALYSIS OF THE BALLOON EXPERIMENTAL DATA 6.2

6.3 CONCLUSIONS 6.17

7.0 REFERENCES 7.1

APPENDIX A - FEATURES AND APPLICATIONS OF THE TALA KITE A.1

APPENDIX B - FEATURES AND APPLICATIONS OF THE TETHERSONDE BALLOON B.1

APPENDIX C - LITERATURE SEARCH - REFERENCE LIST C.1

APPENDIX D - PROGRAM FINDLO LISTING D.1

APPENDIX E - DERIVATION OF EQUATION (3.16) E.1

APPENDIX F - DERIVATION OF EQUATION (4.20) F.1

FIGURES

2.1 Method of Using Two Cameras to Locate a Fixed Object in a Field 2.2

2.2 Extension of the Method Showing in Figure 2.1 . . . . . 2.3

2.3 Region Distribution 2.6

2.4 Translation Between X" and X' 2.7

3.1 Kite in Steady State 3.1

3.2 Kite in Dynamic State 3.3

3.3 Sensitivity Diagram for Equation (3.14) 3.9

4.1 Tethersonde Balloon 4.1

4.2 Balloon Under Steady-State Conditions 4.3

4.3 Balloon Under Dynamic Conditions 4.6

4.4 Sensitivity Diagram for Equation (4.15) 4.8

4.5 Sensitivity Diagram for Equation (4.21) 4.11

4.6 Balloon Streamlines 4.13

5.1 Log-Log Plot of Spectral Density Against Frequency, Kite Run 2, Elevation Angle Data, 60 Lags 5.5

5.2 Log-Log Plot of Spectral Density Against Frequency, Kite Run 2, Elevation Angle Data, 120 Lags 5.5

5.3 Log-Log Plot of Spectrum Against Frequency, Kite Run 2, Elevation Angle Data, 60 Lags 5.6

5.4 Log-Log Plot of Spectrum Against Frequency, Kite Run 2, Elevation Angle Data, 120 Lags 5.6

5.5 Log-Log Plot of Spectral Density Against Frequency, Kite Run 2, Wind Direction Data, 60 Lags 5.7

5.6 Log-Log Plot of Spectral Density Against Frequency, Kite Run 2, Wind Direction Data, 120 Lags 5.7

5.7 Log-Log Plot of Spectrum Against Frequency, Kite Run 2, Wind Direction Data, 60 Lags 5.8

5.8 Log-Log Plot of Spectrum Against Frequency, Kite Run 2, Wind Direction Data, 120 Lags 5.8

5.9 Log-Log Plot of Spectral Density Against Frequency, Tower Run 2, Wind Direction Data, 60 Lags 5.10

5.10 Log-Log Plot of Spectral Density Against Frequency, Tower Run 2, Wind Direction Data, 120 Lags 5.10

5.11 Log-Log Plot of Spectrum Against Frequency, Tower Run 2, Wind Direction Data, 60 Lags 5.11

5.12 Log-Log Plot of Spectrum Against Frequency, Tower Run 2, Wind Direction Data, 120 Lags 5.11

5.13 Kite Run 2 Tower and Kite Velocity Versus Time 5.12

5.14 Kite Run 3 Tower and Kite Velocity Versus Time 5.12

5.15 Log-Log Plot of Spectrum Against Frequency, Kite Versus Tower Run 2 . . . . . 5.14

5.16 Log-Log Plot of Spectral Density Against Frequency, Kite Versus Tower Run 2 . . . . . 5.14

5.17 Spectral Analysis Results 5.15

5.18 Kite Run 2 Versus Daniels Dimensionless Wind Speed Spectra Versus Time 5.17

5.19 Kite Run 3 Versus Daniels Dimensionless Wind Speed Spectra Versus Time 5.17

5.20 Rezero Time Series X(t) 5.19

5.21 Kite Run 2 X(t) Time Series, 1008 Points 5.20

5.22 Kite Run 2 Y(t) Time Series, 1008 Points 5.20

5.23 Kite Run 2 Z(t) Time Series, 1008 Points 5.21

5.24 Kite Run 3 X(t) Time Series, 720 Points 5.21

5.25 Kite Run 3 Y(t) Time Series, 720 Points 5.22

5.26 Kite Run 3 Z(t) Time Series, 720 Points 5.22

5.27 Kite Run 2 Velocity Time Series, 1200 Points 5.23

5.28 Kite Run 3 Velocity Time Series, 720 Points 5.23

5.29 Log-Log Plot of Spectrum and Spectral Density Versus Frequency, Experimental Kite Run 3, 70 Lags 5.25

5.30 Log-Log Plot of Spectrum and Spectral Density Versus Frequency, Experimental Kite Run 3, 35 Lags 5.25

5.31 Log-Log Plot of Spectrum and Spectral Density Versus Frequency, Experimental Kite Run 2, 50 Lags 5.26

5.32 Log-Log Plot of Spectrum and Spectral Density Versus Frequency, Experimental Kite Run 2, 100 Lags 5.26

5.33 Relationship Between θ and w 5.27

6.1 Wind Direction Time Series for Balloon Run 1 . . . . . 6.2

6.2 Wind Direction Time Series for Balloon Run 2; Part 1, 2000 Points 6.3

6.3 Wind Direction Time Series for Balloon Run 2; Part 2, 1600 Points 6.3

6.4 Log-Log Plot of Spectrum Against Frequency, Balloon Run 2, Wind Direction Data, 150 Lags 6.4

6.5 Log-Log Plot of Spectrum Against Frequency, Balloon Run 2, Wind Direction Data, 300 Lags 6.4

6.6 Log-Log Plot of Spectral Density Against Frequency, Balloon Run 2, Wind Direction Data, 150 Lags 6.5

6.7 Log-Log Plot of Spectral Density Against Frequency, Balloon Run 2, Wind Direction Data, 300 Lags 6.5

6.8 Balloon Wind Velocity: Tether Versus Tower 6.7

6.9 Balloon Displacement, X(t) Time Series, First 1700 Points 6.8

6.10 Balloon Displacement, X(t) Time Series, Second 1700 Points . . . 6.8

6.11 Balloon Displacement, Y(t) Time Series, First 1700 Points 6.9

6.12 Balloon Displacement, Y(t) Time Series, Second 1700 Points . . . 6.9

6.13 Balloon Displacement, Z(t) Time Series, First 1700 Points 6.10

6.14 Balloon Displacement, Z(t) Time Series, Second 1700 Points . . . 6.10

6.15 Balloon Velocity Time Series, First Part, 1749 Points 6.12

6.16 Balloon Velocity Time Series, Second Part, 1749 Points 6.12

6.17 Log-Log Plot of Spectral Density Against Frequency, Balloon Displacement Time Series X(t), 350 Lags 6.13

6.18 Log-Log Plot of Spectral Density Against Frequency, Balloon Displacement Time Series X(t), 175 Lags 6.13

6.19 Log-Log Plot of Spectral Density Against Frequency, Balloon Velocity, 150 Lags 6.14

6.20 Log-Log Plot of Spectral Density Against Frequency, Balloon Velocity, 300 Lags 6.14

TABLES

2.1 X' Value in Each of the 8 Regions 2.8

3.1 Sample Values of C 3.6

3.2 Individual Terms in Equation (3.12) 3.7

4.1 The Relation Between the Angle of Attack and the Lift and Drag Coefficients for an Airship with a 4:1 Aspect Ratio 4.10

5.1 Kite Data 5.4

5.2 Mean and Standard Deviation of Kite Anemometer and Tower Data Runs 2 and 3 . . . . . 5.13

5.3 Fluctuating Kite Elevation Angle by Theory Versus the Standard Deviation from PNL Data 5.18

5.4 Means and Standard Deviations of the Kite's Displacement in the X, Y, and Z Direction 5.18

5.5 Mean Kite Velocity and Standard Deviation 5.24

5.6 Mean Kite Velocity and Its Standard Deviation Calculated from the Time Series Y(t) 5.24

5.7 $\bar{w}$ and $\bar{w}^*$ for Runs 2 and 3 . . . . . 5.28

5.8 RMS t' for Tower Data 5.29

5.9 RMS t' for Kite Anemometer from Equation (3.12) 5.30

5.10 Kite Experiment RMS t' Value 5.31

5.11 Correlation Between the Two Z"s for Both Runs 2 and 3 . . . . . 5.31

6.1 Balloon Data List 6.1

6.2 Mean and Standard Deviation of Wind Velocity for Tower Runs 1 and 2 . . . . . 6.6

6.3 Mean and Standard Deviation of the Balloon Displacement from the Digitized Balloon Data 6.7

6.4 Mean and Standard Deviation of New Zeroed Balloon Displacement Series 6.11

6.5 Mean and Standard Deviation Balloon Velocity 6.11

6.6 Durations of Average Time for a Balloon Trip 6.15

6.7 Balloon Displacement Calculated by the Simple and Complex Balloon Theories 6.17

1.0 INTRODUCTION

Tethered balloon and kite anemometers have been used to measure wind velocity and turbulence in the planetary boundary layer and wind turbine environments. The utility and application of such anemometers have been described in reports by, for example, Shieh and Frost (1980); Huang, Shieh, and Frost (1981); Baker, Whitney, and Hewsin (1979); Kirchhoff and Kaminskey (1983); Daniels (1984); Kunkel (1981); and Knowles and Spilhaus (1953).(a) In some cases, balloon and kite anemometer measurements have provided useful information about the wind environment. However, the usefulness of these measurements may be limited by fundamental questions about the response of these instrument systems to the dynamics of the wind field. This study attempted to quantify the response of a kite and a balloon to the combined mean wind flow, U, and the three-dimensional turbulent wind field, u,v,w.

The study reported here was a three-phase effort of 1) theoretical estimation of instrument response to turbulence, 2) data acquisition during actual kite and balloon anemometer flights, and 3) analysis of experimental data and comparison of data with the theories developed. The theoretical analysis of kite and balloon response took two forms. First, an extension of double theodolite theory, used in surveying, was developed specifically for analyzing kite and balloon motion. Second, the response of the kite or balloon was also mathematically predicted by performing linear small perturbation analyses of the effects of atmospheric turbulence on kite or balloon motion. The parameters used in estimating turbulence for the kite were the fluctuating tension, t', in the tether as well as the fluctuating motion of the kite itself; for the balloon, the response equation is developed for the fluctuating elevation angle, θ', as a function of U, u, v, and w, and the aerodynamic forces acting on the balloon itself. For both the kite and balloon, steady-state and dynamic analyses are performed.

The experimental program was designed to measure the dynamic motion of the kite and the balloon, the kite's fluctuating tension, t', the fluctuating elevation angles, θ, of the kite and the balloon, and the three-dimensional

(a) Descriptions of the features and applications of kite and balloon anemometers are given here in Appendices A and B.

turbulent field at an adjacent meteorological tower. These measurements provided values for the dimensionless coefficients developed in the analysis of the kite and the balloon's response equations to turbulence. Kite and balloon flights were performed by Pacific Northwest Laboatory (PNL) personnel at the MOD-2 wind turbine site at Goodnoe Hills, Washington. Instruments on a 360-ft meteorological tower at the site provided free-stream meteorological data for comparison with the wind speed and direction measured by the kite and balloon. While wind measurements from the PNL tower and the kite and balloon anemometer systems were being collected, two 8-mm cameras simultaneously filmed the kite and the balloon in motion as they responded to the turbulent wind field. The films were digitized at the University Computing Center (UCC) at the University of Massachusetts at Amherst. Then, the extended double theodolite theory was used to analyze the film record and calculate the kite's and the balloon's displacement in the X, Y, and Z directions. These displacement data and velocity data were spectrally analyzed. In the final sections of the report, the kite and balloon response equations are compared with the experimentally observed motion.

As an additional investigation of the usefulness of kite and balloon anemometers, a computerized literature search of the Engineering Index using the Dialog Information Service was performed. The key words in the search were anemometer, kite, tethersonde, lifting anemometer, TALA, and balloon. Three files of Dialog were searched: FLUIDEX, DOE ENERGY, and MET/GEOASTRO. All references potentially relevant to this study are listed in Appendix C.

2.0 EXTENDED DOUBLE THEODOLITE THEORY

Double theodolite theory, used by civil engineers in surveying land, is a method by which one can determine the position of an observed object in X, Y, Z coordinates with respect to any point on the ground or other selected reference points, if the distance between two observation points and the elevation and azimuth angles at both points are known. Since this was a study of moving objects, cameras were used instead of theodolites, and an extension of the double theodolite theory was developed to analyze the motion of a kite or balloon anemometer in space. The initial X, Y, Z position of the kite or balloon was determined using double theodolite theory; by applying the extended theory, the exact position of the kite or balloon at each time step during the whole flying session was determined. The comparison of experimental data and the theoretically calculated kite or balloon positions is reported in Chapters 5 and 6.

The geometry of the kite or balloon flights is shown in Figure 2.1. The two cameras (at Positions A and B) were placed on a line perpendicular to the mean wind direction. The distance AB, as well as the initial elevation angle (θ) and azimuth angle (ψ) of each camera, were recorded. The cameras were synchronized to record kite or balloon motion simultaneously. The observer (holding the kite or balloon tether) is at Point C. The kite or balloon is flying at Point D.

According to the general sine law in Equation (2.1), Equation (2.2) may be written from Figure 2.1.

$$\frac{A}{\sin(A)} = \frac{B}{\sin(B)} = \frac{C}{\sin(C)} \tag{2.1}$$

$$\frac{AC}{\sin(\psi_2)} = \frac{L}{\sin(\Pi-\psi_1-\psi_2)} \tag{2.2}$$

where L is the distance between Points A and B and ψ_1, and ψ_2 are the azimuth angles of the cameras. Equations (2.3), (2.4) and (2.5) are derived from

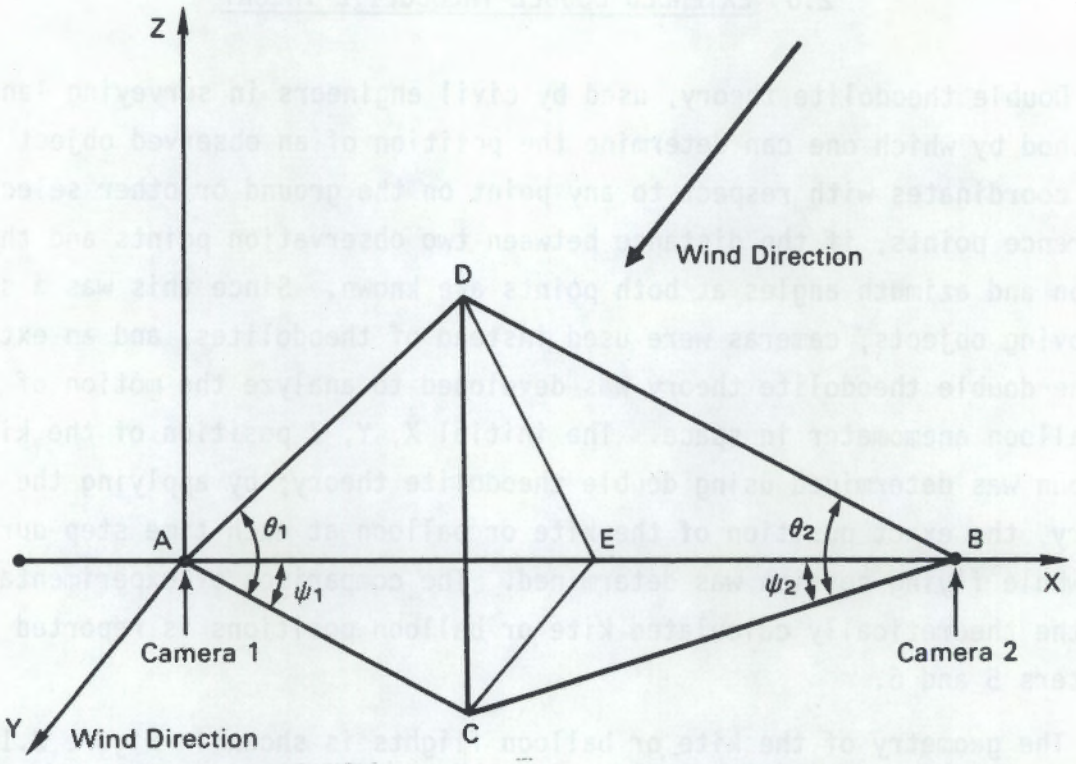

FIGURE 2.1. Method of Using Two Cameras (A and B) to Locate a Fixed Object (D) in a Field

trigonometric rules and are used to find the initial position, at Point D, of the kite or balloon in the program FINDLO (see Appendix D).

$$X = L\sin(\psi_2)\cos(\psi_1)/\sin(\Pi-\psi_1-\psi_2) \quad (2.3)$$

$$Y = L\sin(\psi_2)\sin(\psi_1)/\sin(\Pi-\psi_1-\psi_2) \quad (2.4)$$

$$Z = L\sin(\psi_2)\tan(\theta_1)/\sin(\Pi-\psi_1-\psi_2) \quad (2.5)$$

To capture the position of the kite or balloon in space, the two cameras recorded the kite's or balloon's position on two imaginary planes (see Figure 2.2), which are two faces of a box enclosing the balloon or kite flight volume. The shape of this newly formed box is not always orthogonal. An orthogonal box was then constructed based on the already existing box (see Figure 2.2). This step of building the orthogonal box is necessary for the

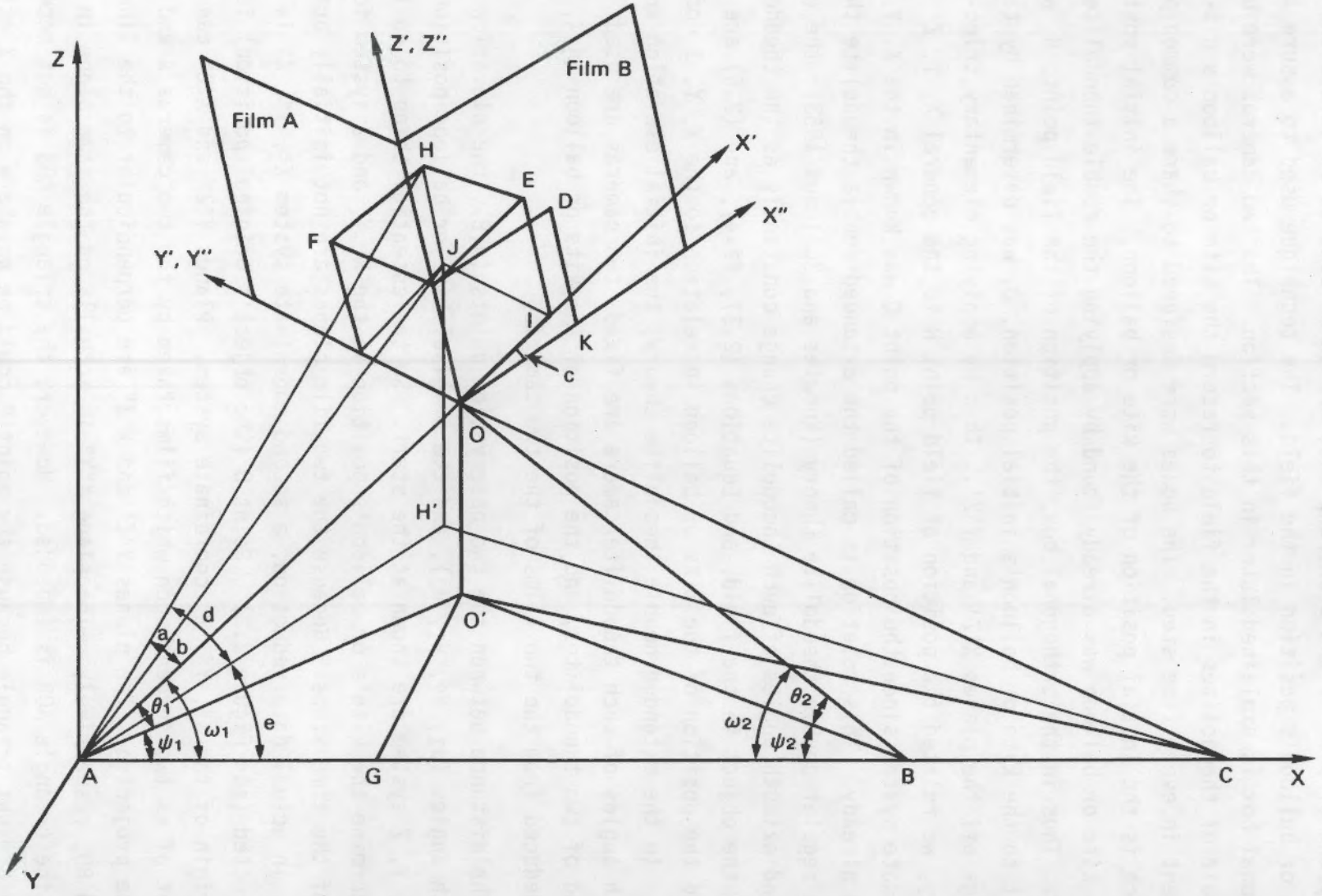

FIGURE 2.2. Extension of the Method Showing in Figure 2.1. The X', Y', and Z' plus the X", Y", and Z" coordinates are constructed.

development of some of the equations that are to be used to calculate the kite's or balloon's position in the field. The technique used to assure an orthogonal box is explained later in this section. The two cameras were used as a pair of theodolites in the field to record the kite or balloon's displacement in every time step. The boxes were designed to share a common point, O, which is the initial position of the kite or balloon. The initial position of the kite or balloon was already found by applying the double theodolite theory. Thus in the orthogonal box, the position of the field point, H, with respect to the kite or balloon's initial position, O, was determined by taking readings off the planes X'Z' and Y'Z'. Then by applying elementary trigonometry, we related the position of field point H to the general X, Y, Z coordinate system since the position of the point O was known in the X, Y, Z system already. This relation is called the extended double theodolite theory. In the regular double theodolite theory (Knowles and Spilhaus 1953), the elevation and azimuth angles of each theodolite change constantly as the theodolite tracks the object in the field, and Equations (2.3), (2.4), and (2.5) are used to find the position of the kite or balloon in relation to the X, Y, Z coordinates. In the extended double theodolite theory, the initial elevation and azimuth angles of each theodolite/camera are fixed, two cameras are used instead of two theodolites, and the position of the kite or balloon in X, Y, Z is deduced from the two films of the two cameras.

The distance between the two observation points (A,B), the elevation and azimuth angles (θ_1, θ_2, ϕ_1, ϕ_2), and the original kite or balloon position in the X, Y, Z system are known at the start. So the essential thing to do is to determine the kite's or balloon's position in the X, Y, and Z system for rest of the time steps. Because the two film planes are not initially orthogonal, in actual data reduction, a second coordinate system X", Y", Z" is constructed (see Figure 2.2). Point O (the object's original position) is the origin of the X", Y", Z" coordinate system. Planes Y"Z" and X"Z" can be thought of as two screens upon which films taken by the two cameras A and B will be projected. The planes Y"Z" and X"Z" are perpendicular to the lines AO and BO, respectively. The plane X"Y" is actually on the same plane in which the triangle AOB is imbedded. However, the triangle AOB is not necessarily a right triangle because the point B could be anywhere on the X axis. This indicates that the plane Y"X" does not necessarily have an orthogonal

relationship with the plane X"Z". Therefore the imaginary point C is introduced to create the right triangle AOC, and a third coordinate system X', Y', Z' is constructed (see Figure 2.2). The new system has the same origin (Point O) as the X", Y", Z" system, and axes Y' and Z' are the same as axes Y" and Z". Because the triangle AOC is a right triangle, then axes Y', Y", and X' are the extension of the lines CO and AO, respectively. Thus axes Y', X', and Z' are the three edges of an orthogonal box. In Figure 2.2, the X', Y', Z' system construct an orthogonal box containing the field point, H. The field point, H, is the new position of the kite (or balloon) at each time step. Based on the X', Y', Z' and X", Y", Z" coordinate systems, the extended double theodolite theory is used to determine the kite's or balloon's new position (Field Point H) in terms of X, Y, Z.

Given that the elevation and azimuth angles (θ_1, θ_2, ϕ_1, ϕ_2) and the length AB are known, Y', Z' and X", Z' are measured on Films A and B (see Figure 2.2). The accuracy of the final height of the object (Z) depends on the accuracy of Z'. If the Z' measured from Film A differs from the Z' measured from Film B, then the average values will be used as an estimate of a Z'. A few problems would cause the two Z' values to disagree. First, if the two cameras did not start simultaneously, then the two Z' values would represent two different time steps with the kite at two different positions. Second, poor film or incorrect focal length would reduce the quality of the digitized data and affect the reading of the Z' values. Finally, if the one or both cameras were not set properly so that the object was within their observable ranges, then the blank film surely would lead to the disagreement of the two Z's. Thus, in the program FINDLO

$$Z' = (Z' \text{ from film A} + Z' \text{ from Film B})/2.$$

Note that angle c between X' and X" depends on w_1 and w_2 (see Figure 2.2), because point B could be anywhere on the X axis.

In Figure 2.3, the X', Y', Z' system is divided into 8 regions. For Z' greater than zero, Region 1 has X' and Y' greater than zero, Region 2 has X' greater than zero and Y' less than zero, Region 3 has X' and Y' less than

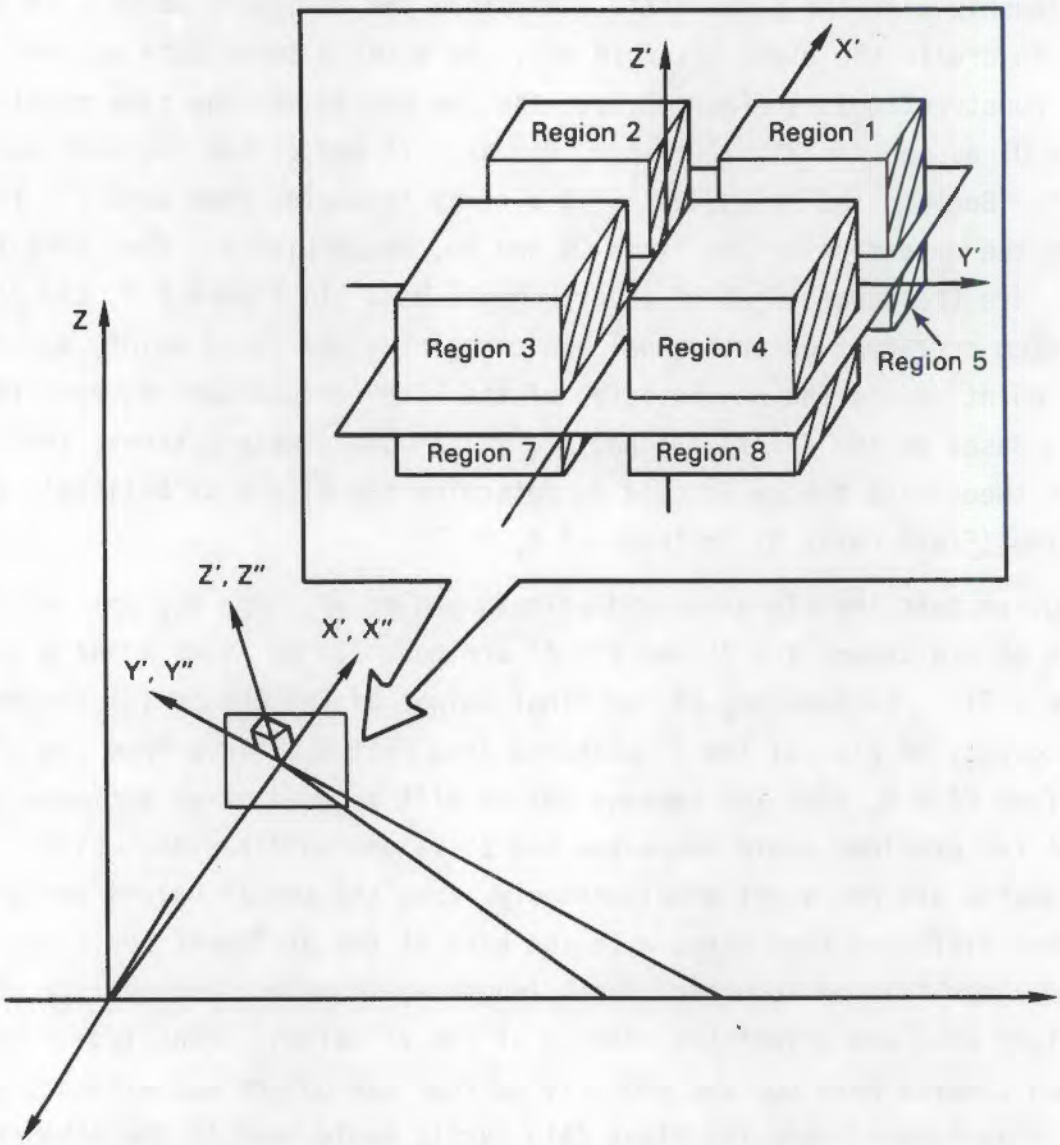

FIGURE 2.3. Region Distribution

zero, and Region 4 has X' less than zero and Y' greater than zero. At Z' less than zero, Regions 5, 6, 7, and 8 have the same X', Y' restriction as Regions 1, 2, 3, and 4, respectively. This description could be applied to X", Y", Z" system as well, since both systems have the same origin.

In Figure 2.2, the orthogonal box is in Region 2. Because both angles KOB and IOC equal 90°, then the angle c is equal to angle BOC. When length AB is less than AC, $c = \omega_1 + \omega_2 - 90°$. When length AB is greater than AC, $c = 90° - \omega_1 - \omega_2$. The value of X' interpreted from X" depends on which region the orthogonal box is in (see Figure 2.4); X' values are shown in Table 2.1.

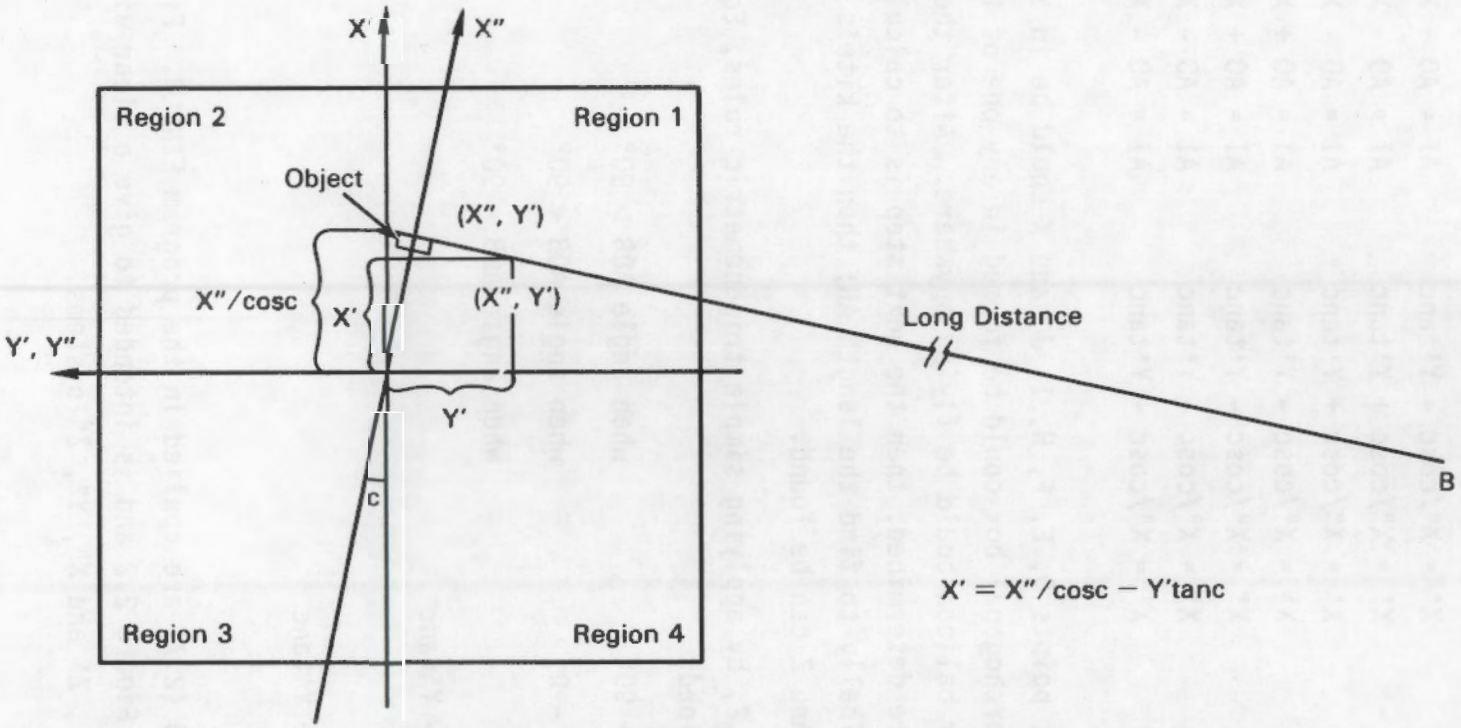

FIGURE 2.4. Translation Between X" and X' (for object in Region 1)

TABLE 2.1. X' Value in Each of the 8 Regions

Region	X'	AI
1	X' = X"/cosc - Y'tanc	AI = AO + X'
2	X' = X"/cosc - Y'tanc	AI = AO + X'
3	X' = X"/cosc + Y'tanc	AI = AO - X'
4	X' = X"/cosc + Y'tanc	AI = AO - X'
5	X' = X"/cosc - Y'tanc	AI = AO + X'
6	X' = X"/cosc - Y'tanc	AI = AO + X'
7	X' = X"/cosc - Y'tanc	AI = AO - X'
8	X' = X"/cosc - Y'tanc	AI = AO - X'

In Figure 2.2, points D, E, F, H, I, J, and K could be in any one of the 8 regions and the orthogonal box could be formed in any one of the 8 regions because the kite or balloon could be flying anywhere. After the value of X' and length of AC are determined, then the next step is to calculate angle a (Figure 2.2) and finally to find the length AH; then the kite's or balloon's position in X, Y, and Z can be found.

From Figure 2.2, by applying simple trigonometric rules, Equations (2.6) and (2.7) are obtained:

$$c = \Omega_1 + \Omega_2 - 90° \qquad \text{when angle AOB} > 90° \qquad (2.6a)$$

$$c = 90° - \Omega_1 - \Omega_2 \qquad \text{when angle AOB} < 90° \qquad (2.6b)$$

$$c = 0 \qquad \text{when angle AOB} = 90° \qquad (2.6c)$$

$$X' = X"/\cos c - Y'\tan c \qquad (2.7a)$$

$$AI = AO + X' \qquad (2.7b)$$

$$X' = X"/\cos c + Y'\tan c \qquad (2.7c)$$

$$AI = AO - X' \qquad (2.7d)$$

Equations (2.6) and (2.7) are applied in the program FINDLO. Figure 2.3 is a blow-up of part of Figure 2.2 and is intended to give a clear view of the 8 regions in X', Y', Z' and X", Y", Z" systems.

Going back to Figure 2.2:

$$AJ = [(AO + X')^2 + Y'^2]^{1/2} \tag{2.8}$$

$$a = \sin^{-1}Y'/AJ \tag{2.9}$$

$$AH = (AJ^2 + Z'^2)^{1/2} \tag{2.10}$$

$$b = \sin^{-1}Z'/AH \tag{2.11}$$

$$e = \phi_1 + a \tag{2.12}$$

$$d = \theta_1 + b \tag{2.13}$$

$$Z = AH\sin d \tag{2.14}$$

$$X = AH\cos d\cos e \tag{2.15}$$

$$Y = AH\cos d\sin e \tag{2.16}$$

Upon careful examination of Figure 2.2, one could observe that Equations (2.8) through (2.16) are independent of the 8 regions of Figure 2.3. Equations (2.6) to (2.16) are those used in the program FINDLO to locate the object's new position (see Appendix D).

After substituting Equations (2.7) through (2.13) into Equations (2.14) through (2.16), the three generalized equations shown below represent the object's location in X, Y, Z space.

$$X = [(AO + X')^2 + Y'^2 + Z'^2]^{(1/2)} \cos\{\theta_1 + \sin^{-1}Z'/[(AO + X')^2 + Y'^2 + Z'^2]^{(1/2)}\} \cos\{\phi_1 + \sin^{-1}Y'/[(AO + X')^2 + Y'^2]^{(1/2)}\} \tag{2.17}$$

$$Y = [(AO + X')^2 + Y'^2 + Z'^2]^{(1/2)} \cos\{\theta_1 + \sin^{-1}Z'/[(AO + X')^2 + Y'^2 + Z'^2]^{(1/2)}\} \sin\{\phi_1 + \sin^{-1}Y'/[(AO + X')^2 + Y'^2]^{(1/2)}\} \tag{2.18}$$

$$Z = [(AO + X')^2 + Y'^2 + Z'^2]^{(1/2)} \sin\{\theta_1 + \sin^{-1}Z'/[(AO + X')^2 + Y'^2 + Z'^2]^{(1/2)}\} \tag{2.19}$$

In Equations (2.17) through (2.19), θ_1 and AO' are constant values and X', Y', and Z' are obtained from the digitized data.

If one knows the initial elevation and azimuth angles from each camera and the distance between the two cameras, and one has a file of digitized film data, one should be able to use the FINDLO program listed in Appendix D to determine the kite or balloon motion.

3.0 RESPONSE THEORY OF KITE TO TURBULENCE: TWO APPROACHES

Two approaches to analyzing the response of the kite to the three-dimensional turbulent wind field are presented here. The analysis is performed from the frame of reference of the moving kite. The first approach is the development of a response equation for the ratio of the fluctuating string tension (t') to the mean string tension (T) as a function of the mean elevation angle (θ) of the kite, the turbulence parameters of the wind field (u,v), and the constrained motion of the kite itself. The second approach, which evolves from the first, is the development of a response equation for the fluctuating elevation angle (θ') as a function of the mean flow (U), the turbulence parameters (u,v), and the mean elevation angle (θ) and the lift and drag coefficients (C_l and C_d) of the kite.

3.1 FIRST APPROACH: RESPONSE EQUATION FOR t'/T

3.1.1 Steady-State Analysis

Figure 3.1 is a sketch of a TALA kite in steady motion in a smooth wind of speed U. The bridle maintains the angle ϕ at a constant while the angle

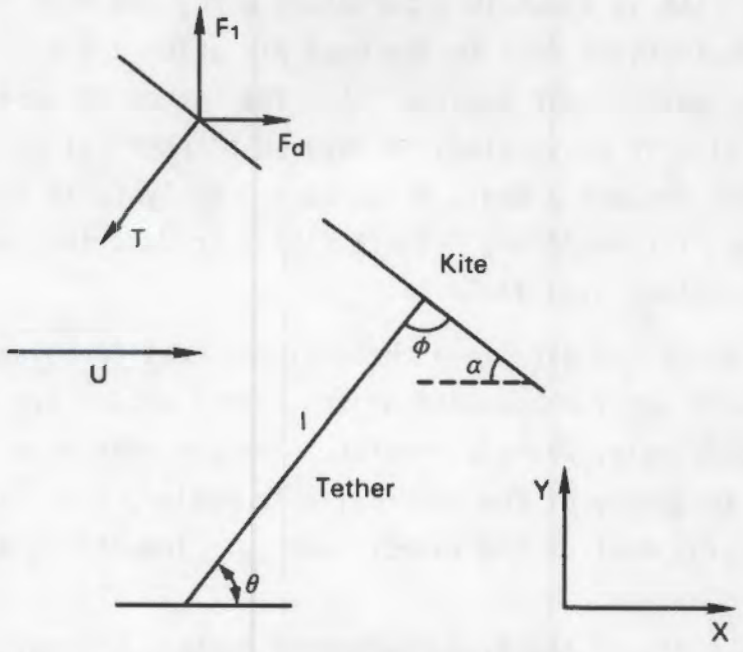

FIGURE 3.1. Kite in Steady State

of attack (α) and the elevation angle (θ) vary according to the relation

$$\theta + \alpha + \phi = 180 \qquad (3.1)$$

The free-body diagram of the kite in Figure 3.1 shows the relation of the string tension (T) to the drag and lift forces (F_d and F_l) as

$$T\cos\theta = F_d \qquad (3.2a)$$

$$T\sin\theta = F_l \qquad (3.2b)$$

or

$$T^2 = F_d^2 + F_l^2 \ . \qquad (3.2c)$$

Sheih and Frost (1980) have shown that when the catenary curve of the tether is accounted for, the height of the kite is given by $h = 0.995l\sin\theta$. They also found that T measured at the ground is within 1% of the tension at the kite.

3.1.2 Dynamic Analysis

When a TALA kite is flown in a turbulent wind, the kite responds to the turbulence in fluctuations (θ') in the mean elevation angle ($\bar{\theta}$) and fluctuations (t') in the mean tether tension (T). The tether is made of no-stretch Kevlar®, so the kite is constrained to move on a spherical surface of radius l. These observations suggest a small perturbation analysis in the spirit of Corrsin (1963) and Kirchhoff and Safarik (1974) to describe the response of the kite to a turbulent wind field.

Figure 3.2 shows the kite in a three-dimensional turbulent wind field of magnitude Q. The X and Y components of the kite's motion are given as $l\omega\sin\theta$ and $l\omega\cos\bar{\theta}$, respectively, where $\omega = d\theta/dt$. The variable ω is considered to be the dominant frequency of the vertical kite motion, i.e., it is the frequency that contains most of the kinetic energy. The string tension (t') is

®Kevlar is a trademark of the E. I. DuPont de Nemours Company, Wilmington, Delaware.

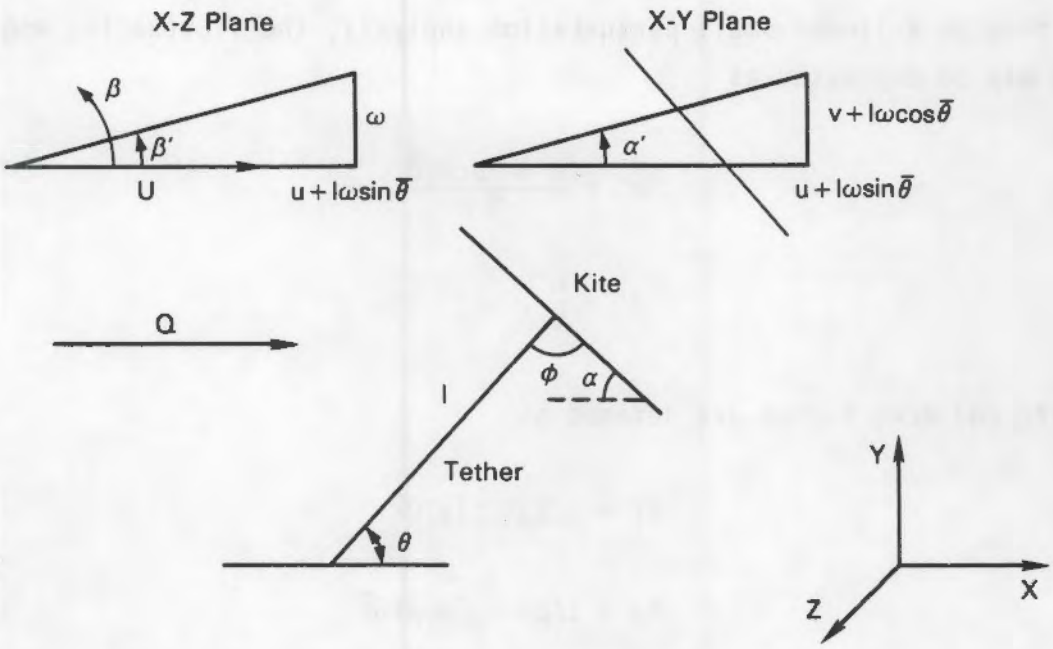

FIGURE 3.2. Kite in Dynamic State

not affected by motion in the z direction because the force coefficient of the kite in the z direction is symmetric and thus its slope at the mean kite position is zero. This fact has the effect of separating the z motion of the kite from t'. This point will be further illustrated as the analysis proceeds.

In a linear small perturbation analysis, each variable is assumed to have an instantaneous value, which is the sum of the mean plus a fluctuating value, as illustrated in Equation (3.3).

$$\theta = \bar{\theta} + \theta' \tag{3.3a}$$

$$\alpha = \bar{\alpha} + \alpha' \tag{3.3b}$$

$$T = \bar{T} + t' \ . \tag{3.3c}$$

Figure 3.2 also shows the kite subject to instantaneous change in the angles of attack α' and β' caused by turbulence. The magnitude of the speed seen by the kite, due to both the turbulence and the kite motion, may be written as

$$Q = [(U + u + l\omega\sin\bar{\theta})^2 + (v + l\omega\cos\bar{\theta})^2 + w^2](1/2) \tag{3.4}$$

Since this is a linear small perturbation analysis, the fluctuating angle of attack may be expressed as

$$\alpha' = \frac{v + l\omega\cos\bar{\theta}}{U} \tag{3.5a}$$

$$\beta' = \frac{w}{U} . \tag{3.5b}$$

The lift and drag forces are defined as

$$F_l = 1/2\rho A C_l(\alpha) Q^2 \tag{3.6a}$$

$$F_d = 1/2\rho A C_d(\alpha,\beta) Q^2 \tag{3.6b}$$

where ρ is the fluid density, A is the area of the kite, and C_l and C_d are the lift and drag coefficients. For the fluctuating motion of the kite in the z direction, the angle $\beta = \bar{\beta} + B'$; however, $\bar{\beta} = 0$, and thus $\beta = \beta'$.

The lift and drag coefficients are expanded in a Taylor series about the mean angle of attack as

$$C_l(\alpha) = C_l(\bar{\alpha}) + \left(\frac{\partial C_l}{\partial \alpha}\right)_{\bar{\alpha}} a' \tag{3.7a}$$

$$C_d(\alpha,\beta) = C_d(\bar{\alpha},\bar{\beta}) + \left(\frac{\partial C_d}{\partial \alpha}\right)_{\bar{\alpha},\bar{\beta}} \alpha' + \left(\frac{\partial C_d}{\partial \beta}\right)_{\bar{\alpha},\bar{\beta}} \beta' + \ldots \tag{3.7b}$$

Since $\bar{\beta} = 0$, $C_d(\bar{\alpha},\bar{\beta}) = C_d(\bar{\alpha})$. Although the exact form of $C_d(\beta)$ is not known, $C_d(\beta)$ will be a symmetric function in β. Thus $(\partial C_d/\partial\beta)_{\bar{\alpha},\bar{\beta}} = 0$. This is the why kite fluctuations in the z direction are not reflected in t' when only linear terms are maintained in the analysis.

In terms of the perturbation quantities in Equation (3.3) and the Taylor series expansion of the lift and drag coefficients in Equation (3.7), Equation (3.2) can be written as

$$(\bar{T} + t')^2 = (1/2\rho A)^2[C_d(\bar{\alpha} + \alpha) + C_l(\bar{\alpha} + a')]^2 Q^2 \quad . \tag{3.8}$$

Substituting Equations (3.4), (3.5), (3.6), and (3.7) into (3.8), expanding in a Taylor series and a binomial series, neglecting higher order terms, and subtracting Equation (3.2) from this expansion yields, after some algebraic manipulation, the following response equation for the fluctuating string tension (t')

$$\frac{t'}{\bar{T}} = 2\left(\frac{u}{U} + \frac{l\omega\sin\bar{\theta}}{U}\right) + C\left(\frac{v}{U} + \frac{l\omega\cos\bar{\theta}}{U}\right) \tag{3.9}$$

where the constant C is given as

$$C = \left[\frac{\cos^2\bar{\theta}}{C_d(\bar{\alpha})}\left(\frac{\partial C_d}{\partial\alpha}\right)_{\bar{\alpha}} + \frac{\sin^2\bar{\theta}}{C_l(\bar{\alpha})}\left(\frac{\partial C_l}{\partial\alpha}\right)_{\bar{\alpha}}\right] \quad . \tag{3.10}$$

Equation (3.9) demonstrates that the fluctuating tension (t') is a function of the turbulent fluctuations (u,v) and the kite motion ($l\omega$). If the kite motion is small relative to the turbulence, then Equation (3.9) becomes a function of the turbulence only. Using the definitions

$$\frac{u'}{U} = \frac{u}{U} + \frac{l\omega\sin\alpha}{U} \tag{3.11a}$$

$$\frac{v'}{U} = \frac{v}{U} + \frac{l\omega\cos\alpha}{U} \tag{3.11b}$$

the RMS value of Equation (3.9) may be written

$$\frac{(\overline{t'^2})^{0.5}}{\bar{T}} = \left(\frac{4\overline{u'^2}}{U^2} + C^2\,\frac{\overline{v'^2}}{U^2} + 4C\,\frac{\overline{u'v'}}{U^2}\right)^{0.5} \quad . \tag{3.12}$$

The overbar represents the time average.

The constant C can be evaluated for some sample cases. For example, we assumed that $C_l = \sin 2\bar{\alpha}$, $C_d = \sin^2\bar{\alpha}$ and $\phi = 90°$; then, Equations (3.1), (3.7), and (3.10) were used to construct Table 3.1 for the constant C. These results clearly show an intuitively reasonable conclusion that as the elevation angle ($\bar{\theta}$) increases, the string tension (t') becomes a stronger function of the vertical turbulence fluctuations (v), while at low elevation angles, the string tension is a stronger function of the horizontal fluctuation (u).

A sample calculation for $(\overline{t'^2})^{0.5}/\bar{T}$, assuming $\bar{\theta} = 40°$, h = 200 ft, z_o = 3 cm, $u/U = 1/\ln(z/z_o)$, $v/U = 0.52u/U$, and $\overline{uv} = (0.31)uv$, for the case of no kite motion, yields:

$$\frac{(\overline{t'^2})^{0.5}}{\bar{T}} = 0.2990 \ .$$

If the kite is assumed to move at a frequency of 0.001 Hz, close to the peak of the power spectral density of horizontal fluctuation (Lumley and Panofsky 1964), then the above value is modified to

$$\frac{(\overline{t'^2})^{0.5}}{\bar{T}} = 0.5287 \ .$$

The dominant term in each of the above sample calculations is $4\overline{u'^2}/U^2$; however, the other two terms in the expressions are too large to be ignored. Table 3.2 shows the magnitude of each of the contributing terms in the string tension.

TABLE 3.1. Sample Values of C

$\bar{\alpha}°$	$\frac{1}{C_l}\left(\frac{\partial C_l}{\partial \alpha}\right)_{\bar{\alpha}}$	$\frac{1}{C_d}\left(\frac{\partial C_d}{\partial \alpha}\right)_{\bar{\alpha}}$	$\bar{\theta}°$	C
10	5.4950	11.3400	80	5.6712
20	2.3840	5.4950	70	2.7479
30	1.1550	3.4641	60	1.7323
40	0.3527	2.3840	50	1.1920
45	0.0000	0.0000	45	1.0000
50	-0.3527	1.6782	40	0.8391
60	-1.1547	1.1547	30	0.5774

TABLE 3.2. Individual Terms in Equation (3.12)

	ω = 0 Hz	ω = 0.001 Hz
$4\bar{u}'^2/U^2$	0.0688	0.1852
$C^2\bar{v}'^2/U^2$	0.0067	0.0404
$4C\overline{u'v'}/U^2$	0.0139	0.0539

The experimental verification of these sample calculations appears in Chapter 5.

3.2 SECOND APPROACH: RESPONSE EQUATION FOR θ'

By observing the flying kite in turbulence, one sees clearly that the changes in elevation angle and azimuth angle of the tether are directly related to the motion of the kite in the turbulent wind field. Because the turbulent velocity parameter u in the mean flow direction X is normally greater than the turbulent parameters in the other directions and because the change of the elevation angle is directly related to the kite's motion in the mean flow direction, a second small perturbation analysis of the response of the kite to the three-dimensional turbulent wind field was performed. A response equation was obtained for the fluctuating elevation angle (θ') as a function of the mean elevation angle ($\bar{\theta}$) of the kite, the turbulence parameters of the wind field (u,v), and the constrained motion of the kite itself.

The steady-state relationship of the string tension (T) to the lift and drag forces (F_l and F_d) was shown in Equation (3.2). For the calculation of the fluctuating elevation angle (θ'), Equation (3.2) may be rewritten as

$$T = F_d/\cos\theta \qquad (3.2d)$$

$$F_l = F_d\tan\theta \ . \qquad (3.2e)$$

The variables have instantaneous values as defined in Equation (3.3), the lift and drag forces are defined as in Equation (3.6), and the force coefficients are expanded in a Taylor series about the mean angle of attack as in Equation (3.7).

Because this is a linear small perturbation analysis of the response equation for the fluctuating elevation angle (θ'), the fluctuating angle of attack may be expressed as

$$a' = \theta' + \frac{v}{U} \tag{3.13}$$

Substituting Equations (3.3), (3.6), (3.7), and (3.13) into (3.2d and e), expanding in a Taylor series and a binomial series, and neglecting higher-order terms, after some algebraic manipulation, we see that the response equation for the fluctuating elevation angle (θ') is

$$\theta' = \frac{\left(\frac{C_l}{C_d} - \tan\theta\right)\frac{2u}{U} + \left(\frac{C_{l,\alpha}}{C_d} - \frac{C_{d,\alpha}}{C_d}\tan\theta\right)\left(\frac{v}{U}\right)}{\left(\tan\theta\,\frac{C_{d,\alpha}}{C_d} + \sec^2\theta - \frac{C_{l,\alpha}}{C_d}\right)\left(1 + \frac{2u}{U}\right) + \frac{C_{d,\alpha}}{C_d}\sec^2\theta\left(\frac{v}{U}\right)}. \tag{3.14}$$

For a more detailed derivation of Equation (3.14) see Appendix E.

As defined in Section 3.1, $C_l = \sin 2\bar{\alpha}$, $C_d = \sin 2\bar{\alpha}$, and $\phi = 90°$. The variables $C_{l,\alpha}$ and $C_{d,\alpha}$ are the derivatives of C_l and C_d and are defined as $C_{l,\alpha} = 2\cos 2\alpha$ and $C_{d,\alpha} = \sin 2\alpha$.

A sample calculation for θ', assuming $\bar{\theta} = 52°$, $u/U = 0.11131$, $v/U = 0.52u/U$, $C_l = \sin 2\bar{\alpha}$, $C_d = \sin^2\bar{\alpha}$, $C_{l,\alpha} = 2\cos 2\alpha$, $C_{d,\alpha} = \sin 2\alpha$, $\phi = 90°$, and $\alpha = 180° - \bar{\theta} - \phi$, yields:

$$\theta' = 0.12077 \text{ rad}.$$

If $u/U = 0.12538$, $v/U = 0.52u/U$, and all other parameters remain in the same values, Equation (3.14) yields:

$$\theta' = 0.14970 \text{ rad}.$$

The sensitivity diagram given as Figure 3.3 shows the relationship between θ' and all the other parameters. It is clear from the diagram that θ' is very sensitive to changes in $\bar{\theta}$ and not very sensitive to changes in all other parameters.

Since the fluctuating elevation angle of the kite can be found from Equation (3.14) and the length of the string attached to the kite is known, then the kite's displacement (s) in the direction of mean wind flow can be calculated:

$$s = \theta' l \ . \tag{3.15}$$

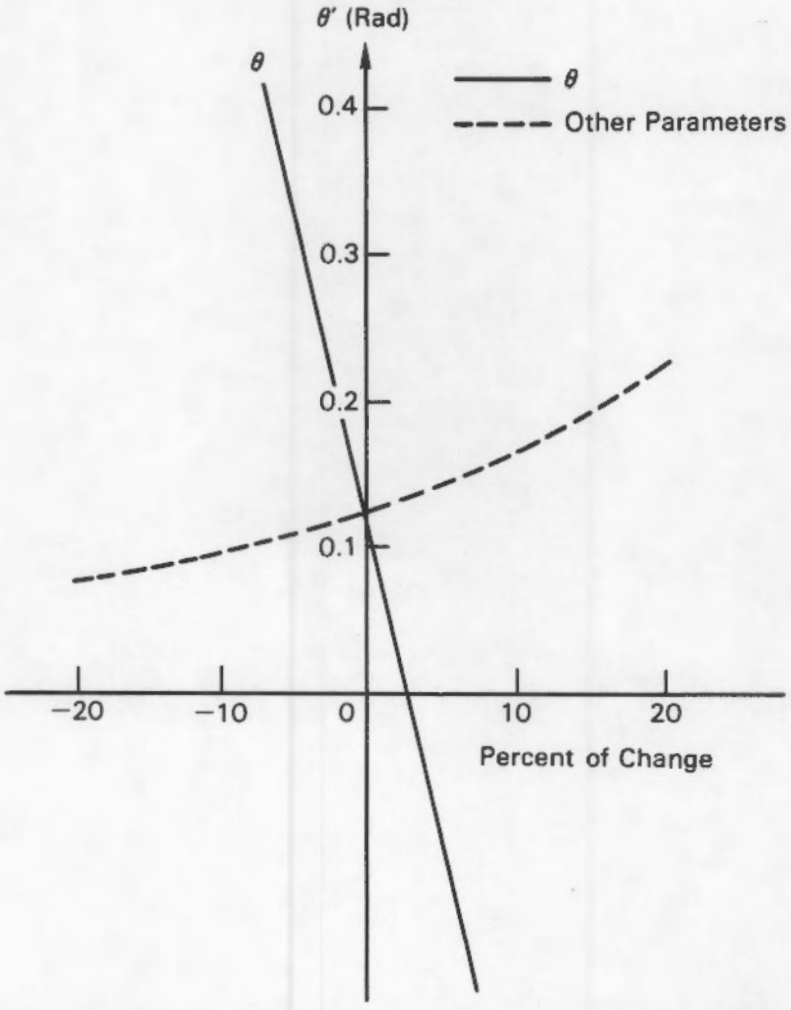

FIGURE 3.3. Sensitivity Diagram for Equation (3.14)

4.0 RESPONSE THEORY OF A TETHERSONDE BALLOON TO TURBULENCE

In this chapter, a linear perturbation analysis of the response of the balloon to the three-dimensional (u,v,w) turbulent wind field, performed from the frame of reference of the moving balloon, is presented. The result of the analysis is a response equation for the fluctuating elevation angle (θ') as a function of the mean elevation angle ($\bar{\theta}$), the mean wind velocity (U), the turbulence parameters (u and v) and the constrained motion of the balloon itself.

The balloon has a symmetric shape and an aspect ratio of 4:1. A sketch of the balloon is presented in Figure 4.1. More detail about the features and applications of the tethered balloon are given in Appendix B.

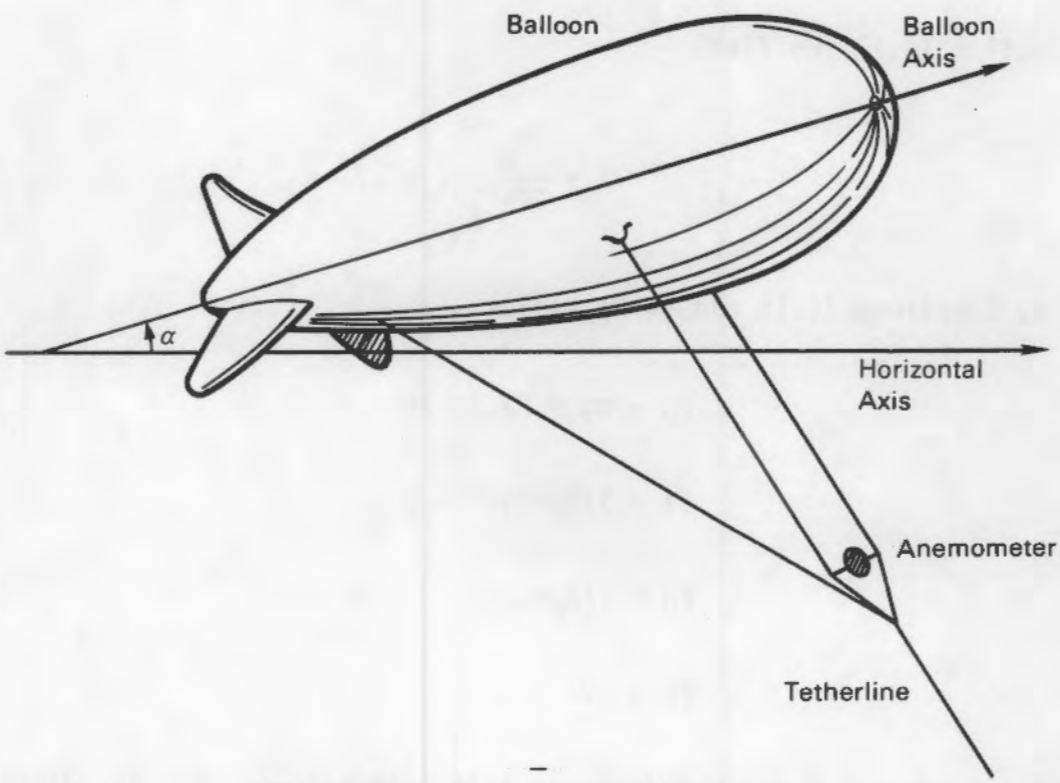

FIGURE 4.1. Tethersonde Balloon

4.1 STEADY-STATE ANALYSIS

Figure 4.2a shows a situation where the lift force (F_l), drag force (F_d), tension of the string (T), weight of the balloon (mg), and buoyancy force (F_b) are in equilibrium. In Figure 4.2a, the angle of attack (α) equals zero. Figure 4.2b also shows F_l, F_d, F_b, mg, and T in equilibrium but α is not equal to zero. The turbulence in the wind field is excluded from the steady-state analysis. For $\alpha = 0$, the lift force (F_l) was said to be zero because of the symmetry of the balloon.

A state force balance shows

$$F_d = T\cos\theta_1 \tag{4.1}$$

$$T\sin\theta_1 + mg = 0 \ . \tag{4.2}$$

From Equation (4.1), we find

$$T = \frac{F_d}{\cos\theta_1} \ . \tag{4.3}$$

Combining Equations (4.1) and (4.2) yields

$$F_b - mg = F_d \tan\theta_1 \tag{4.4}$$

$$F_l = 1/2\rho AC_l U^2 = 0$$

$$F_d = 1/2\rho AC_d U^2 \tag{4.5}$$

$$F_b = \rho V$$

where C_d, C_l, ρ, and V are the drag and lift coefficients, the air density, and the volume of the balloon, respectively.

a. Case Where $\alpha = 0$

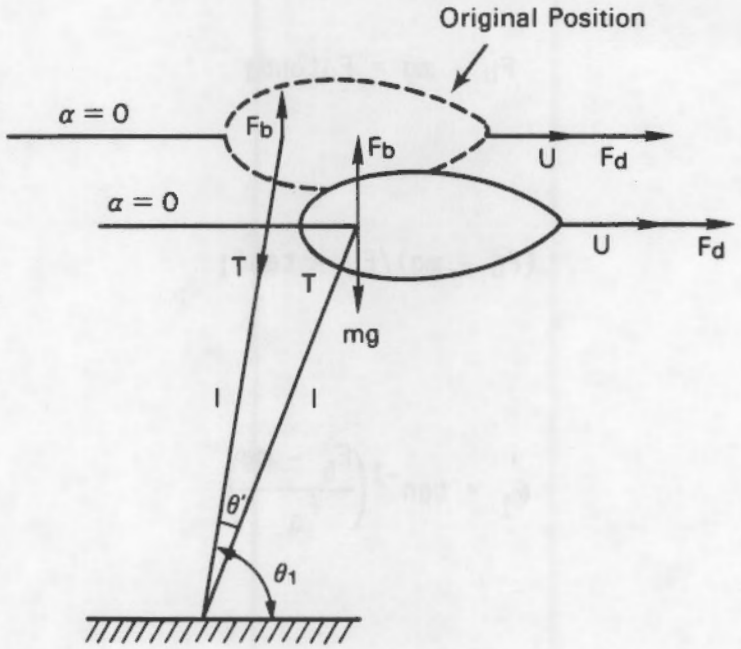

b. Case Where $\alpha \neq 0$

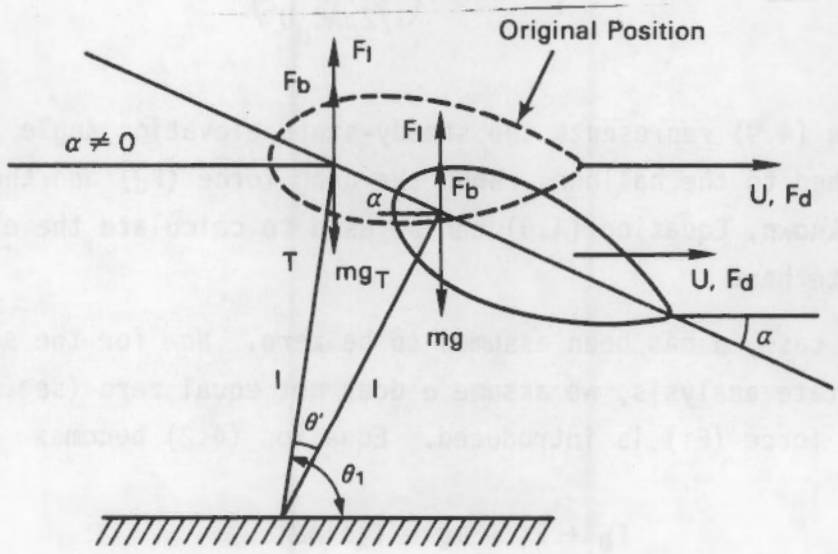

FIGURE 4.2. Balloon Under Steady-State Conditions

Given that

$$F_b - mg = F_d \tan\theta_1 \tag{4.6}$$

so

$$(F_b - mg)/F_d = \tan\theta_1 \tag{4.7}$$

and so

$$\theta_1 = \tan^{-1}\left(\frac{F_b - mg}{F_d}\right) \tag{4.8}$$

then

$$\theta_1 = \tan^{-1}\left(\frac{\rho V - mg}{1/2\rho A C_d U^2}\right) . \tag{4.9}$$

Equation (4.9) represents the steady-state elevation angle (θ_1) of the tether attached to the balloon. When the drag force (F_d) and the mass of the balloon are known, Equation (4.9) can be used to calculate the elevation angle (θ_1) of the tether.

In this case, α has been assumed to be zero. Now for the second case of the steady-state analysis, we assume α does not equal zero (see Figure 4.2b), and the lift force (F_l) is introduced. Equation (4.2) becomes

$$F_b + F_l - mg = T_1 \sin\theta_1 . \tag{4.10}$$

Inserting Equation (4.1) into Equation (4.9), we have

$$F_b + F_l - mg = T_1 \sin\theta_1/\cos\theta_1 . \tag{4.11}$$

Inserting Equation (2.6) into Equation (4.9) yields

$$\theta = \tan^{-1} \frac{\left(V\rho + 1/2\rho AC_l U^2 - mg\right)}{\left(1/2\rho AC_d U\right)^2} . \qquad (4.12)$$

Equation (4.12), like Equation (4.9), could be used to determine the elevation angle (θ_1) if F_l, F_d, and the mass of the balloon were known.

4.2 DYNAMIC ANALYSIS

There are horizontal, vertical, and lateral (u, v, and w) turbulent velocity fluctuations in an actual wind field. In Chapter 3 it was stated that because a kite is symmetric it has a symmetric force coefficient in the lateral direction. Since the body of the balloon is also symmetric, the balloon also has a symmetric force coefficient in the lateral direction. The magnitudes of the mean wind speed (U), the horizontal and vertical turbulence (u,v), and the lift and drag forces (F_l, F_d) are the major sources of the fluctuation of the balloon in a wind field (see Figure 4.3). As it was for the steady-state case, the dynamic analysis of the balloon was carried out in two parts: for $\alpha = 0$ and $\alpha \neq 0$. Also as in the steady-state analysis, when $\alpha = 0$, the lift force (F_l) is zero. The vertical turbulence (v) is neglected because of the symmetry of the body; only the horizontal turbulence (u) is included (see Figure 4.3a).

From Figure 4.3a, we see that

$$F_d = T_1 \cos\theta_1 \qquad (4.1)$$

$$F_b = T_1 \sin\theta_1 + mg \qquad (4.2)$$

$$F_d = 1/2\rho AC_d Q^2 \qquad (4.3)$$

$$F_b = \rho V .$$

a. Case Where $\alpha = 0$

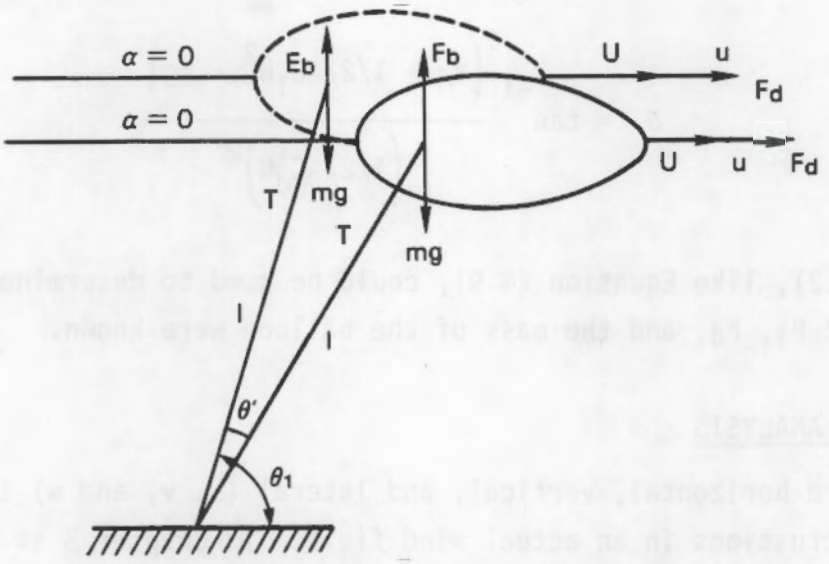

b. Case Where $\alpha \neq 0$

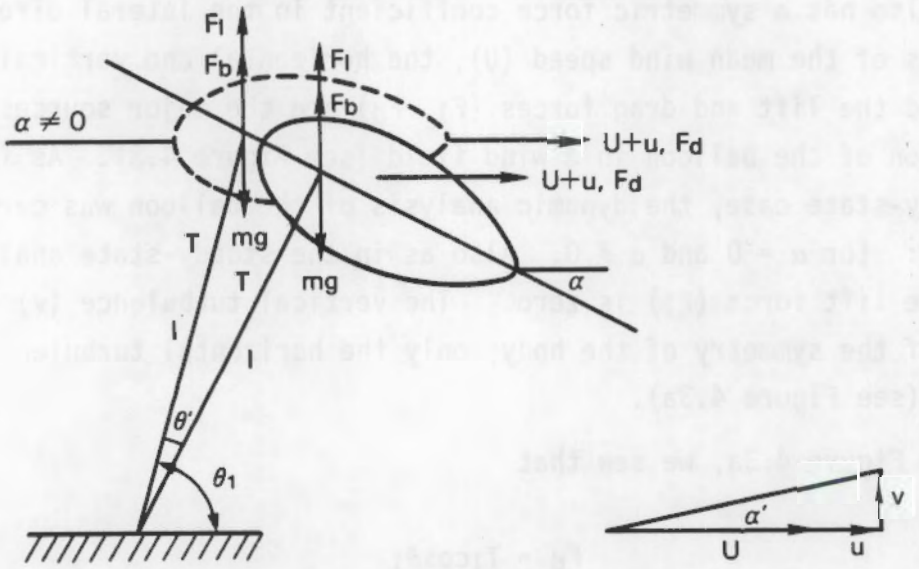

FIGURE 4.3. Balloon Under Dynamic Conditions

The variables C_l, C_d, θ_1, t, and U in turbulence were assumed to have instantaneous values that are the sum of a mean plus a fluctuating value. Thus,

$$C_l(\alpha) = C_l(\bar{\alpha}) + C_{l,\alpha}(\alpha')$$
$$C_d(\alpha) = C_d(\bar{\alpha}) + C_{l,\alpha}(\alpha') \ .$$

Where the angle of attack has a nonzero value

$$\theta_1 = \bar{\theta}_1 + \theta_1' \tag{4.13a}$$
$$T = \bar{T} + t' \tag{4.13b}$$
$$Q^2 = (U + u)^2 + v^2 + w2 \ . \tag{4.13c}$$

If Equations (4.1) and (4.2) are combined, then

$$F_b - mg = F_d \tan\theta_1$$
$$\tan(\theta_1 + \theta_1') = \tan\theta_1 + (\theta_1')\sec^2\theta_1 \ . \tag{4.14}$$

According to Equations (4.13), (4.5), and (4.7),

$$\rho A - mg = 1/2\rho A C_d(U^2 + 2Uu + u^2)\tan(\theta_1 + \theta_1')$$
$$\rho A - mg = 1/2\rho A C_d(U^2 + 2Uu + u^2)(\tan\theta_1 + (\theta_1')\sec^2\theta_1) \ . \tag{4.15}$$

Expanding Equation (4.15) in a Taylor series and a binomial series, and neglecting higher order terms, we see that after some algebraic manipulation, Equation (4.15) becomes

$$\theta_1' = \frac{-2\tan\theta_1 \frac{u}{U}}{\sec^2\theta_1\left(1 + \frac{2u}{U}\right)} \ . \tag{4.16}$$

If the length of the tether is known, then the fluctuating displacement of the balloon can be calculated as

$$s = \theta_1^{\dagger} \cdot l \tag{4.17}$$

A sensitivity diagram (Figure 4.4) shows the relationship between the movement of the balloon and such independent variables as the changing of the elevation angle (θ_1), the length of the tether (l), and the intensity of the turbulence (u/U). Clearly, the displacement of the balloon is extremely sensitive to the elevation angle (θ_1). Changes in u/U and L do not have nearly as much impact on the displacement of the balloon as the change in θ_1.

The vertical turbulence (v) and the lift force (F_l) were added in the second case of the dynamic analysis (Figure 4.3b), that is, the case of $\alpha \neq 0$.

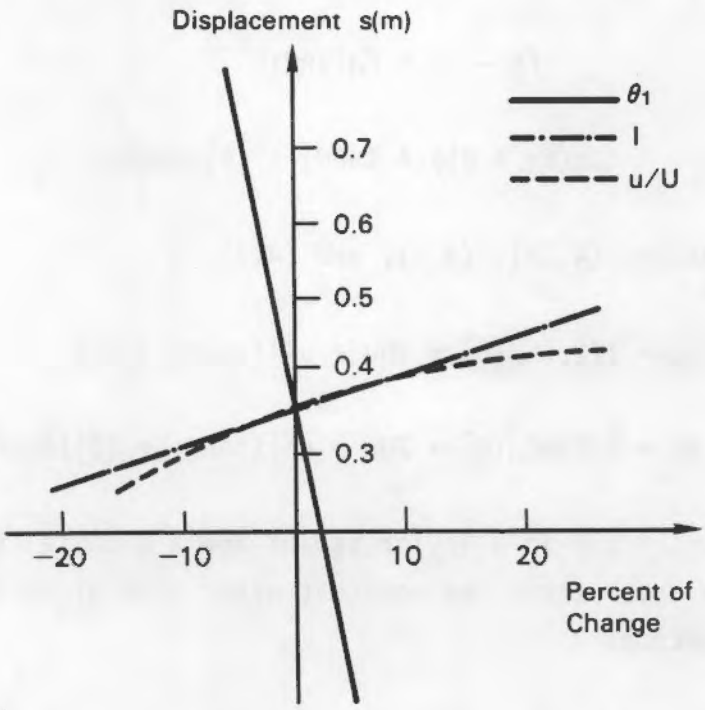

FIGURE 4.4. Sensitivity Diagram for Equation (4.15)

Summation of forces in the vertical direction gives

$$F_b - mg + F_l = T\sin\theta_1$$

$$F_d = T\cos\theta_1 \qquad (4.18)$$

$$F_b - mg + F_l = F_d\tan\theta_1 \ .$$

Insert Equation (4.5):

$$\rho V - mg + 1/2\rho AC_l U^2 = 1/2\rho AC_d U^2 + \tan\theta_1 \ . \qquad (4.19)$$

Apply Equation (4.13):

$$\rho V - mg + 1/2\rho A(C_l(\bar{\alpha}) + C_{l,\alpha}(\alpha'))((U + u)^2 + v^2) =$$

$$1/2\rho A(C_d(\bar{\alpha}) + C_{d,\alpha}(\alpha'))((U + u)^2 + v^2)\tan(\theta + \theta') \ . \qquad (4.20)$$

Then, from Equation (4.14)

$$\tan(\theta_1 - \theta') = \tan\theta_1 + (\theta')\sec^2\theta_1; \qquad (4.14)$$

expanding Equation (4.20) and dropping the higher-order and F_b and mg-directly cancelling terms, we have,

$$\theta' = \frac{\left(\frac{C_l}{C_d} - \tan\theta_1\right)\left(\frac{2u}{U}\right) + \left(\frac{C_{l,\alpha}}{C_d} - \frac{C_{d,\alpha}}{C_d}\tan\theta_1\right)\left(\frac{v}{U}\right)}{\left(\tan\theta_1\frac{C_{d,\alpha}}{C_d} + \sec^2\theta_1 - \frac{C_{l,\alpha}}{C_d}\right)\left(1 + \frac{2u}{U}\right) + \frac{C_{d,\alpha}}{C_d}\sec^2\theta_1\left(\frac{v}{U}\right)}. \qquad (4.21)$$

The derivation of Equation (4.21) is described in more detail in Appendix F.

In Equation (4.21)

$$C_{l,\alpha} = \frac{\partial C_l}{\partial\alpha} \qquad (4.22)$$

$$C_{d,\alpha} = \frac{\partial C_d}{\partial \alpha} , \qquad (4.23)$$

where α has to be in radians.

Lang (1948) and Hoerner (1965, 1975) have provided the data for the lift and drag coefficients (Table 4.1). Fuselage 7 of Lang (1948) has the same aspect ratio, 4:1, as the tethersonde balloon tested here.

When the range of the angle of attack is known, $C_{l,\alpha}$ and $C_{d,\alpha}$ can be calculated from Equations (4.22) and (4.23). For example, if $2 < \alpha < 4$, from Table 2.1,

$$\alpha = 2 \qquad C_l = 0.0118 \qquad C_d = 0.0288$$

$$\alpha = 4 \qquad C_l = 0.0239 \qquad C_d = 0.0293$$

$$C_{l,\alpha} = (0.0239 - 0.0118)/((4 - 2)(3.14/180))$$

$$C_{d,\alpha} = (0.0293 - 0.0288)/((4 - 2)(3.13/180)).$$

TABLE 4.1. The Relation Between the Angle of Attack and the Lift and Drag Coefficients for an Airship with a 4:1 Aspect Ratio (Lange 1948; Hoerner 1965, 1975)

Angle of Attack	C_l	C_d
0	0	0.0265
2	0.0118	0.0288
4	0.0239	0.0293
6	0.0368	0.0297
10	0.0598	0.0363
15	0.0941	0.0464

Equation (4.17) is again used to calculate the displacement of the balloon. A sensitivity diagram (Figure 4.5) shows the relationship between the displacement (s) and the change of the elevation angle (θ_1), u/U, and the length of the tether (l). In Figure 4.5, the balloon displacement is very sensitive to the change the elevation angle (θ_1), as in Figure 4.4.

Figures 4.4 and 4.5 have shown that the absolute value of the slope of curve (1) (change in θ) is much greater than the absolute slope values of curves (2) and (3) (change in l and u/U, respectively). Obviously, the elevation angle is the major influence on the balloon's displacement. Variations of u/U and l do not change the displacement of the balloon nearly as much as if elevation angle had changed in Figures 4.4 and 4.5. Equation (4.16) is the essential form of the function of (θ') that represents the response of the balloon to the wind turbulence. Equation (4.21) is an improved, expanded form of Equation (4.16) in which lift and drag coefficients (C_l, C_d), $C_{d,\alpha}$, and $C_{l,\alpha}$ are included.

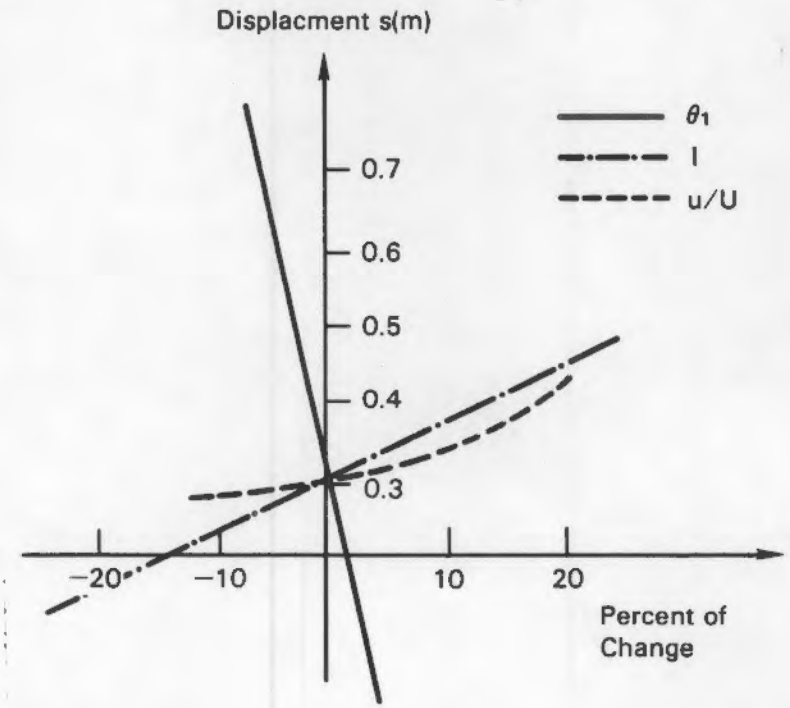

FIGURE 4.5. Sensitivity Diagram for Equation (4.21)

Kirchhoff (1985) has shown a steady flow analysis over an airship with an aspect ratio of 4:1 (Figure 4.6). The balloon under investigation here has a anemometer suspended about 1 m under it and located about 1 m from its front end. Knowing the position of the anemometer with respect to the balloon and using Figure 4.6, one can see that the anemometer is in the region between the two isotachs indicated as Q=1.05 and Q=1.01. That is, the average wind speed measured by the anemometer suspended under the balloon is between 1% and 5% of the average free-stream wind speed to which the balloon is actually subjected.

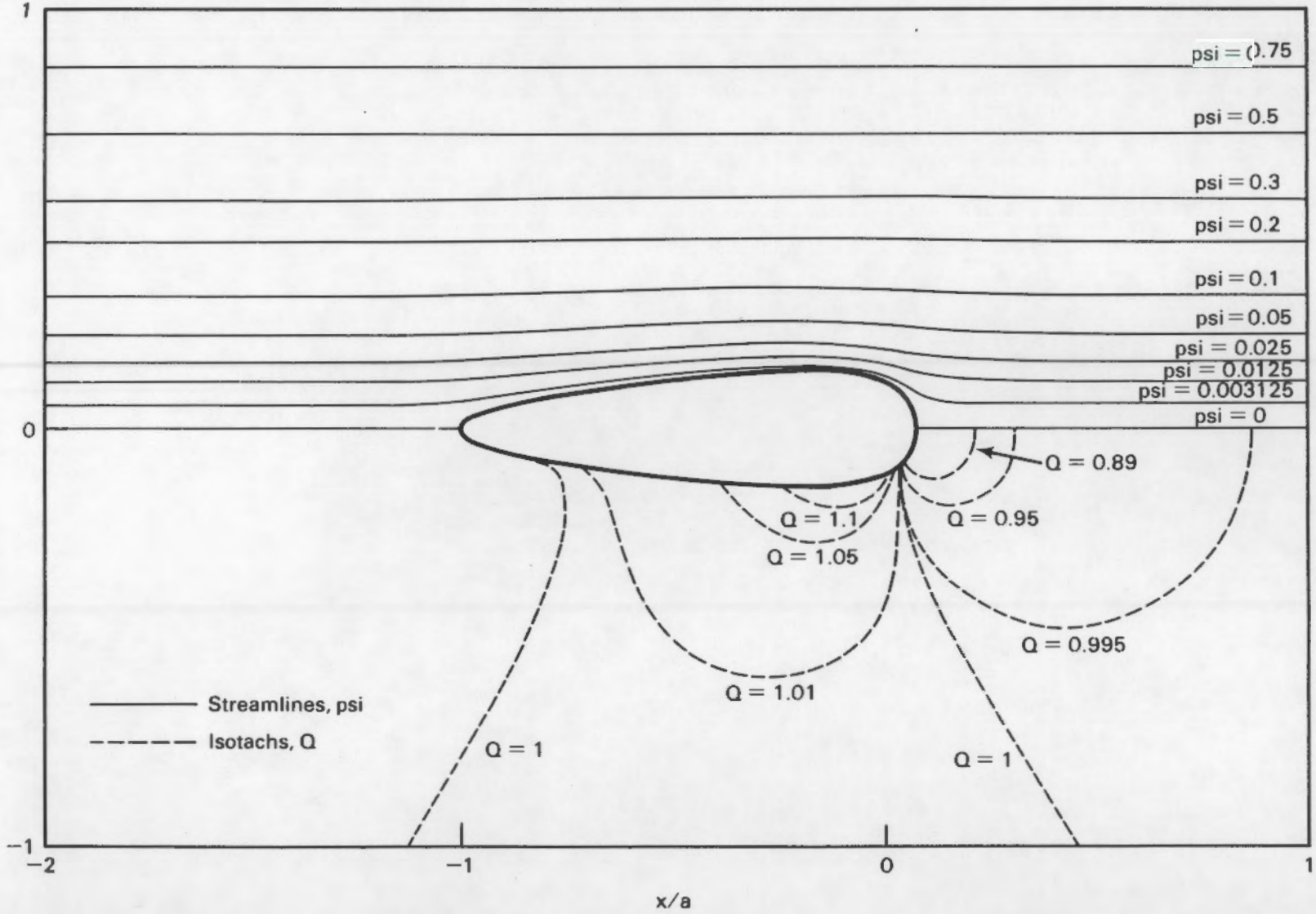

FIGURE 4.6. Balloon Streamlines

5.0 KITE EXPERIMENTS AND RESULTS

To obtain data for use in verifying the response equations developed in Chapters 3 and 4, kite and balloon anemometers were flown in the field adjacent to the PNL meteorological tower at the Goodnoe Hills wind turbine site. As explained in the discussion of extended double theodolite theory in Chapter 2, synchronized cameras were used instead of theodolites to record kite and balloon motion. Analysis of the film records provided displacement data that, along with meteorological parameters recorded by the airborne anemometers and the PNL tower instrumentation, was used in the verification exercise. The TALA kite has an area of approximately 1 ft^2 and with its tail weighs approximately 1 oz. The angle ϕ in Figure 3.1 is a constant, maintained by the kite's bridle; the angle of attack (α) and the elevation angle (θ) vary according to the relation $\phi + \alpha + \theta = 180°$, as shown in Figure 3.1.

Four kite runs were performed. During each run, the nearby meteorological tower recorded the wind direction and wind speed, and the kite anemometer recorded the wind speed, the wind direction, and the elevation angle of the kite.

The two 8-mm cameras were placed on a line perpendicular to the mean wind direction, as was shown in Figure 2.1. The distance between the two cameras and the initial elevation angle (θ) and azimuth angle (ϕ) were recorded. To provide an easily-seen reference point, a cross with 10-in. arms made with 1.5-in.-wide tape was placed on the kite; however, the cross was difficult to see in the films because of the small (8 mm) focal length of the camera and the changing orientation of the kite.

The motion from the films was digitized at the University Computing Center (UCC) at the University of Massachusetts (U. Mass.) at Amherst. Each frame of the film was projected onto a digitizing board, and the position of the kite was located and digitized. The digitized data were first stored on a desktop computer and later transferred to a mainframe computer system on which the computations for this project were performed. Because the cross on the kite was hard to distinguish, the position of the whole kite was digitized.

By using the extended double theodolite theory developed in Chapter 2, the displacement of the kite (s), represented here as X(t), Y(t), and Z(t), and the kite velocity V(t) as a time series were calculated from the digitized kite film data.

Since randomness is one of the major characteristics of turbulence, the Statistical Package for Social Science (SPSS) was employed to perform a spectral analysis of the displacement and velocity time series. Spectral analysis was also applied to all the kite data sets, and the results were studied and compared. Means and standard deviations for all the data sets were also calculated. Tower wind-speed data were plotted against kite anemometer wind-speed data as time series, and similarities and differences were examined. The results calculated from the tower and kite anemometer data by the kite response equations developed in Chapter 3 are compared with the results calculated from the digitized film data by the same theory. The spectral analysis of the kite anemometer wind speed data were also compared to some previous work of Daniels (1984).

5.1 SPECTRAL ANALYSIS

Turbulent flows are always dissipative. Viscous shear stress performs deformation work, which increases the internal energy of the fluid at the expense of kinetic energy of the turbulence. Turbulence needs a continuous supply of energy to make up for the viscous losses. Thus, some kind of indicator of how energy transforms within the turbulence is needed. Spectra and spectral density have been frequently used as the energy indicators in wind energy research and the study of turbulence (Daniels 1984, Connell 1982). The spectra and spectral density functions of SPSS were the most suitable tools for this study.

Spectral analysis is a concept in which each variable, thought of as a time series or function over time, can be meaningfully represented by pure sine waves summed over different frequencies, with a different amplitude and phase at each frequency. Spectral analysis proceeds by Fourier transforming the data to obtain the coefficients of the sinusoids at a discrete set of frequencies, grouping neighboring frequencies into frequency bands, and estimating various frequencies from the Fourier-transformed data in one frequency

band at a time. Frequencies are grouped together in bands to enhance the statistical stability of the estimates. A clear description of spectral analysis has been given by Thrall and Engelman (1976).

The SPSS package was employed to perform the spectral analysis. The main features of SPSS are that it allows calculation of the spectra, spectral density, autocorrelations, cross correlations, and other functions of a time series. Five standard windows are available: the Parven, Bartlett, Tukey, Hamming, and Unit windows. The window phrase specifies the lag window or weighting function to be applied to auto- and cross covariances for smooth spectrum estimates. Test runs using all five windows indicated that those runs using the unit window gave smoother spectrum estimates and better results at lower frequencies. Therefore the unit window was chosen over other windows to perform its role in the spectral analysis.

As a rule, the number of the lags should be less than 10% of the total number of data points in a data set. Thus for each SPSS run, 10% and 5% of the data points are used as lag numbers to produce a smooth spectral estimate. The lag number affects the lowest frequency in a frequency band; the highest frequency is governed by the Nyquist sampling criteria. Since the total number of the data points does not change for a specific data set, the highest frequency in a frequency band is not affected by the lag number chosen for that data set.

For example, SPSS could be run on a time series that has 1000 data points with a data sampling rate of 2 data/s. With 10% of the total data points as the lag number, the highest and the lowest frequencies are 1 and 0.001 Hz. If lag number is changed to 5%, the highest frequency is still 1 Hz but the lowest frequency becomes 0.002 Hz. That is, larger lag numbers result in lower frequencies.

5.2 ANALYSIS OF EXPERIMENTAL RESULTS

Only the second and the third runs could be analyzed; the other run data were unusable because of the poor kite quality and incompleteness of the films. The two runs studied are referred to as Runs 2 and 3. Table 5.1 gives more detail about the two usable kite runs.

TABLE 5.1. Kite Data

Source	Experiment	Start	End	Rate	Data Points
Tower	Kite Run 2	16:07	16:17	2 data/s	1200
	Kite Run 3	17:16	17:23	2 data/s	840
Kite Anemometer	Kite Run 2	16:07	16:17	2 data/s	1200
	Kite Run 3	17:16	17:23	2 data/s	840
Films	Kite Run 2	16:07	16:17	2 data/s	1200
	Kite Run 3	17:16	17:23	2 data/s	840

Data from Runs 2 and 3 include wind direction, kite elevation angle, and wind speed. There are 1200 and 840 data points respectively for Runs 2 and 3. Spectral analysis was performed on wind direction and kite elevation of the Run 2 data. The spectra and the spectral densities were graphed on log-log papers for 120 and 60 lags. Figures 5.1 and 5.2 show the spectral densities of the kite Run 2 anemometer elevation-angle data for 60 and 120 lags and Figures 5.3 and 5.4 show the spectra of the kite Run 2 anemometer elevation-angle data for 60 and 120 lags. Figures 5.5 and 5.6 are the spectral densities and Figures 5.7 and 5.8 are the spectra of the kite Run 2 anemometer wind-direction data for 60 and 120 lags. Figures 5.1 and 5.3 show that there is a peak at about 0.017 Hz and Figures 5.2 and 5.4 also show a peak at about 0.017 Hz. This indicates there is a dominant frequency of 0.017 Hz in the elevation angle during the kite anemometer Run 2. The mean elevation angles ($\bar{X}$) of kite anemometer Runs 2 and 3 were then calculated from the kite elevation time series using

$$\bar{X} = \frac{1}{N} \sum_{i=1}^{N} X_i \qquad (5.1)$$

where N is the number of data points and X_i is the ith data point in a data set.

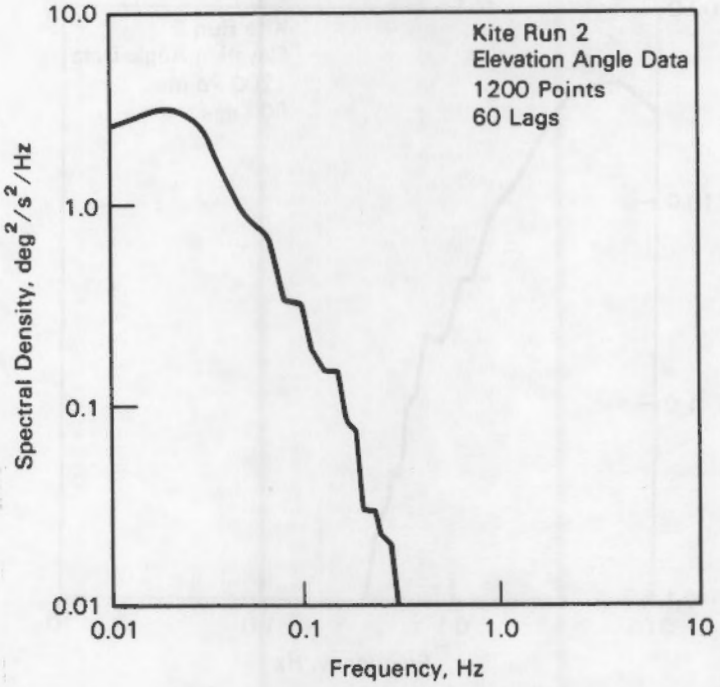

FIGURE 5.1. Log-Log Plot of Spectral Density Against Frequency, Kite Run 2, Elevation Angle Data, 60 Lags

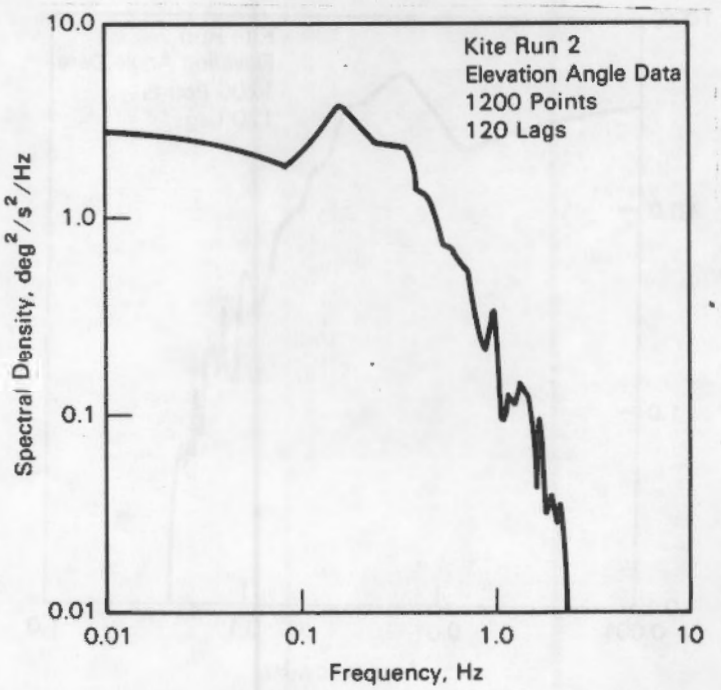

FIGURE 5.2. Log-Log Plot of Spectral Density Against Frequency, Kite Run 2, Elevation Angle Data, 120 Lags

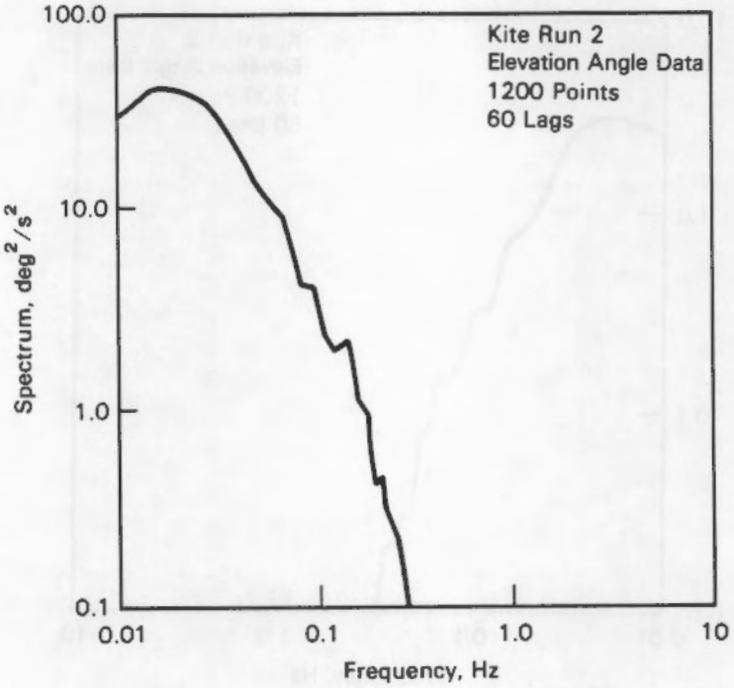

FIGURE 5.3. Log-Log Plot of Spectrum Against Frequency, Kite Run 2, Elevation Angle Data, 60 Lags

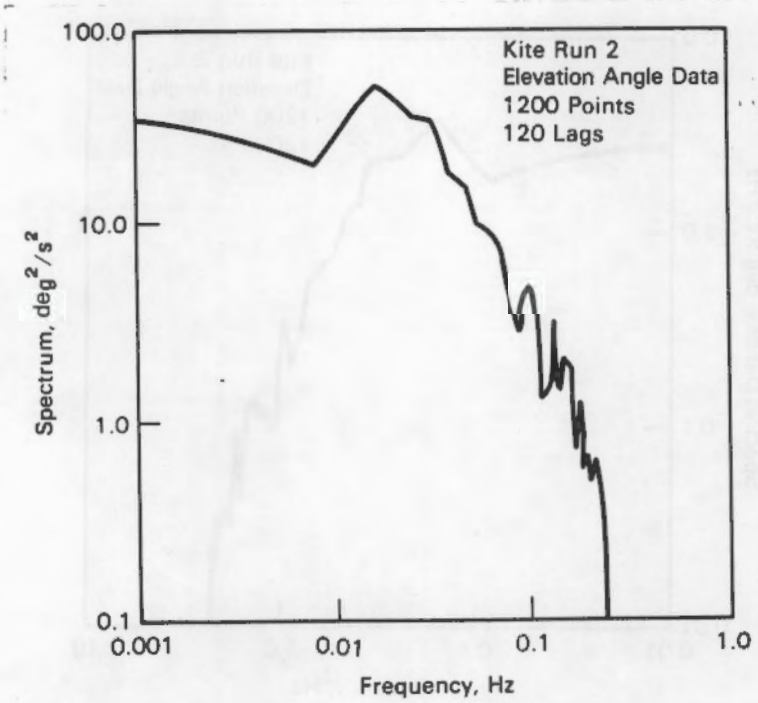

FIGURE 5.4. Log-Log Plot of Spectrum Against Frequency, Kite Run 2, Elevation Angle Data, 120 Lags

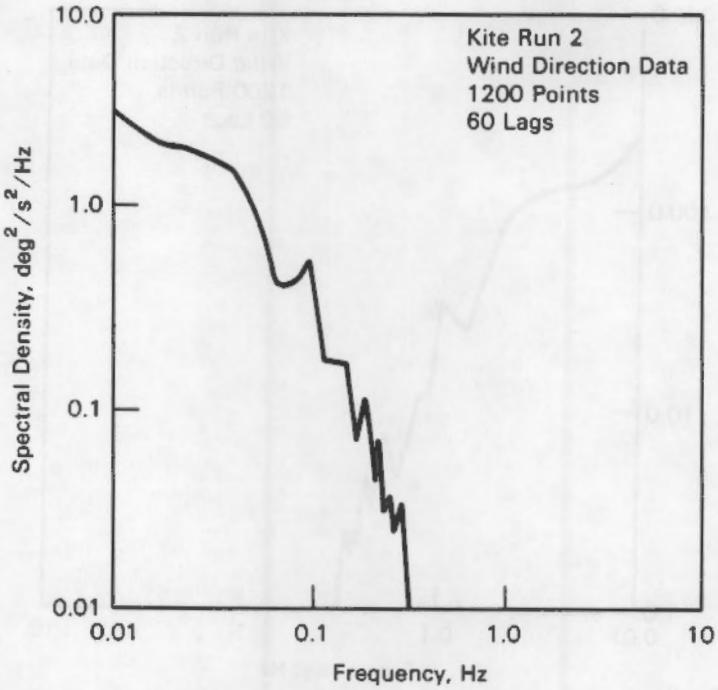

FIGURE 5.5. Log-Log Plot of Spectral Density Against Frequency, Kite Run 2, Wind Direction Data, 60 Lags

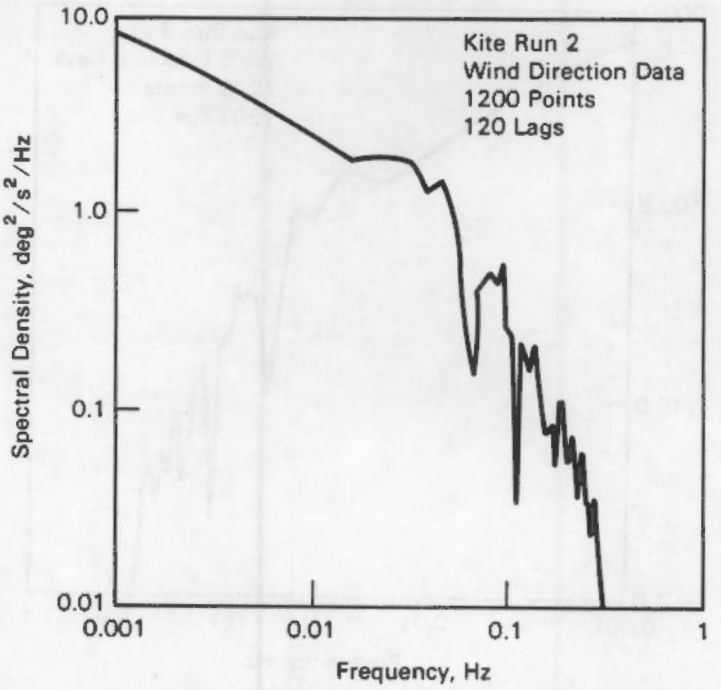

FIGURE 5.6. Log-Log Plot of Spectral Density Against Frequency, Kite Run 2, Wind Direction Data, 120 Lags

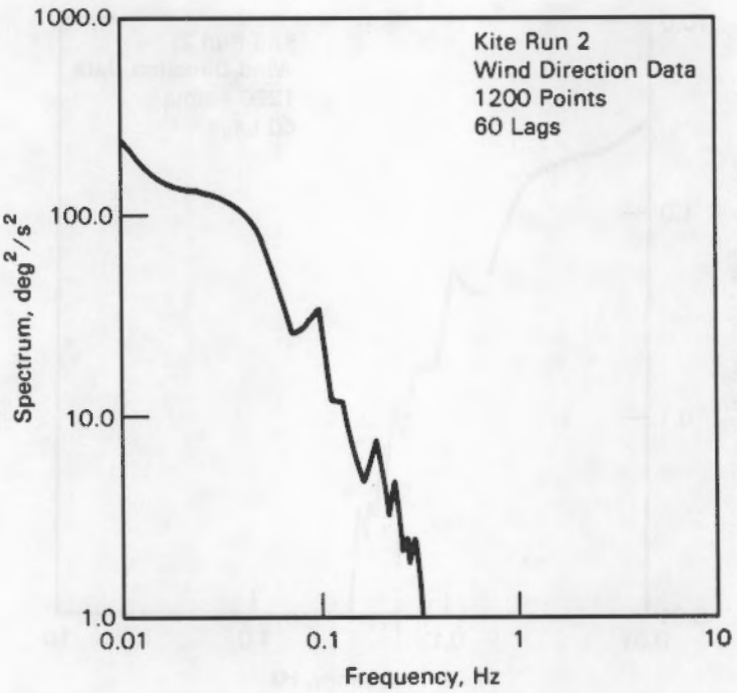

FIGURE 5.7. Log-Log Plot of Spectrum Against Frequency, Kite Run 2, Wind Direction Data, 60 Lags

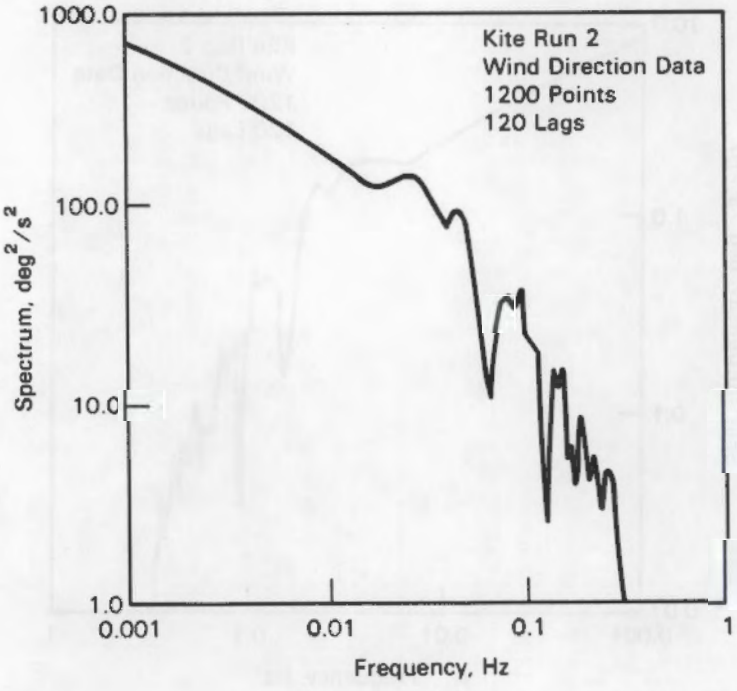

FIGURE 5.8. Log-Log Plot of Spectrum Against Frequency, Kite Run 2, Wind Direction Data, 120 Lags

The results show that the mean elevation angles for kite Runs 2 and 3 are 52.7589 and 52.2048 degrees respectively. This result will be used in the kite response equation [Equation (3.16)] to calculate the kite's fluctuating elevation angle (θ').

Figures 5.5, 5.6, 5.7 and 5.8 do not show any significant peak. It is reasonable to assume that peaks might appear at lower frequencies than the lowest frequency that SPSS could resolve.

Tower data for Runs 2 and 3 include wind direction and wind speed. Figures 5.9 and 5.10 are the spectral densities of the tower Run 2 wind direction data and Figures 5.11 and 5.12 are the spectra for the same data set. The lag number is indicated on each graph. None of these figures show any distinct spectral peaks, confirming what was observed in Figures 5.5 to 5.8, the spectral results of the wind-direction data from the kite anemometer.

The kite anemometer and tower Runs 2 and 3 wind-speed data were plotted as time series on Figures 5.13 and 5.14. By examining these time series, one can see both higher frequency components and large amplitude variations in the kite wind speed over the tower wind speed. Figure 5.13 shows a flat spot for the time between 30 and 110 s. During that period, the kite anemometer data were not transmitted to the receiver on the ground. Further analysis of the kite Run 2 wind speed data is therefore restricted to the time domain between Second 110 and Second 600.

Equations (5.1) and (5.2) are used to calculate the mean and the standard deviation of the data sets.

$$\sigma = \left(\frac{\sum (X_1 - \bar{X})^2}{N}\right)^{0.5} . \qquad (5.2)$$

The means and standard deviations for the wind-speed time series were calculated for both kite and tower data for Runs 2 and 3. The results are presented in Table 5.2.

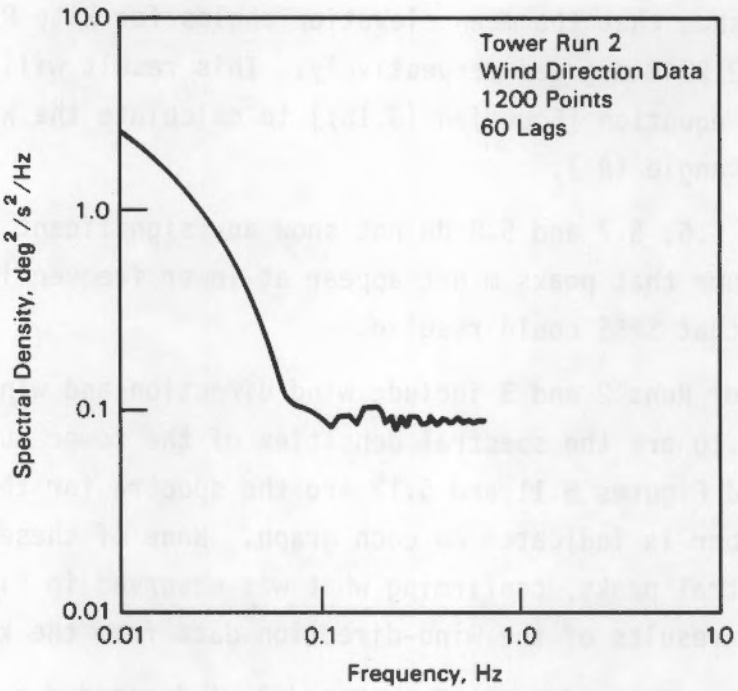

FIGURE 5.9. Log-Log Plot of Spectral Density Against Frequency, Tower Run 2, Wind Direction Data, 60 Lags

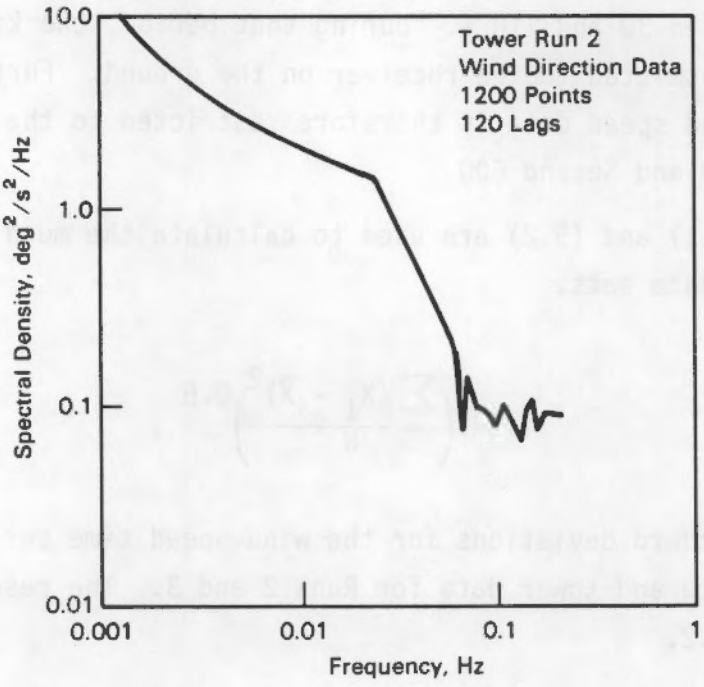

FIGURE 5.10. Log-Log Plot of Spectral Density Against Frequency, Tower Run 2, Wind Direction Data, 120 Lags

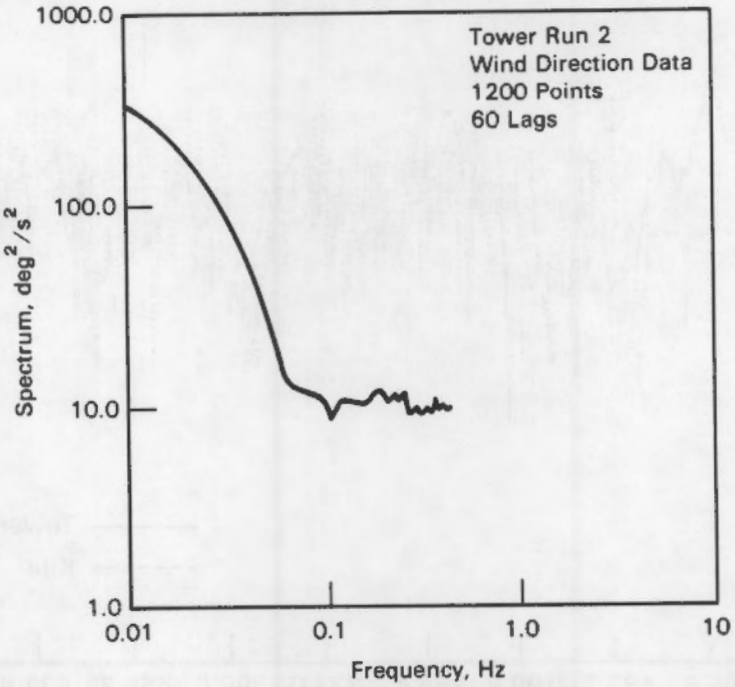

FIGURE 5.11. Log-Log Plot of Spectrum Against Frequency, Tower Run 2, Wind Direction Data, 60 Lags

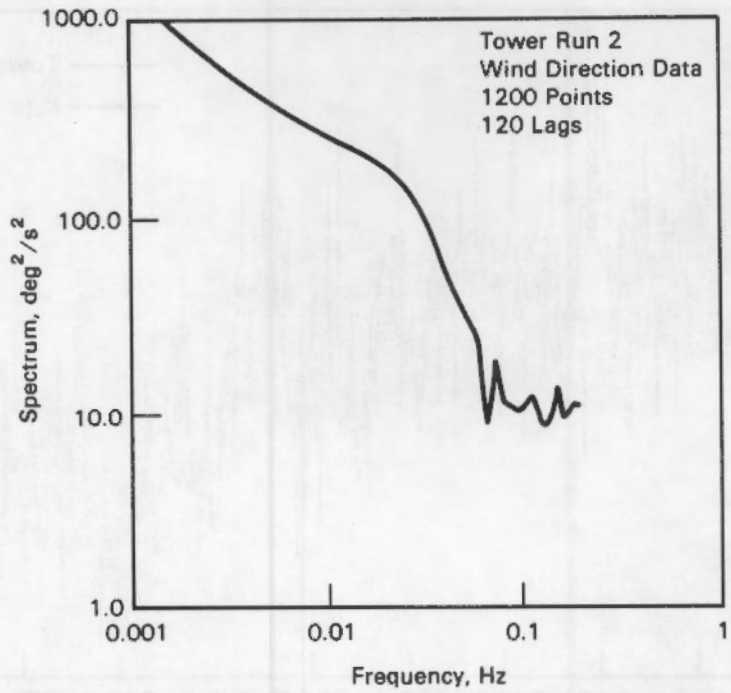

FIGURE 5.12. Log-Log Plot of Spectrum Against Frequency, Tower Run 2, Wind Direction Data, 120 Lags

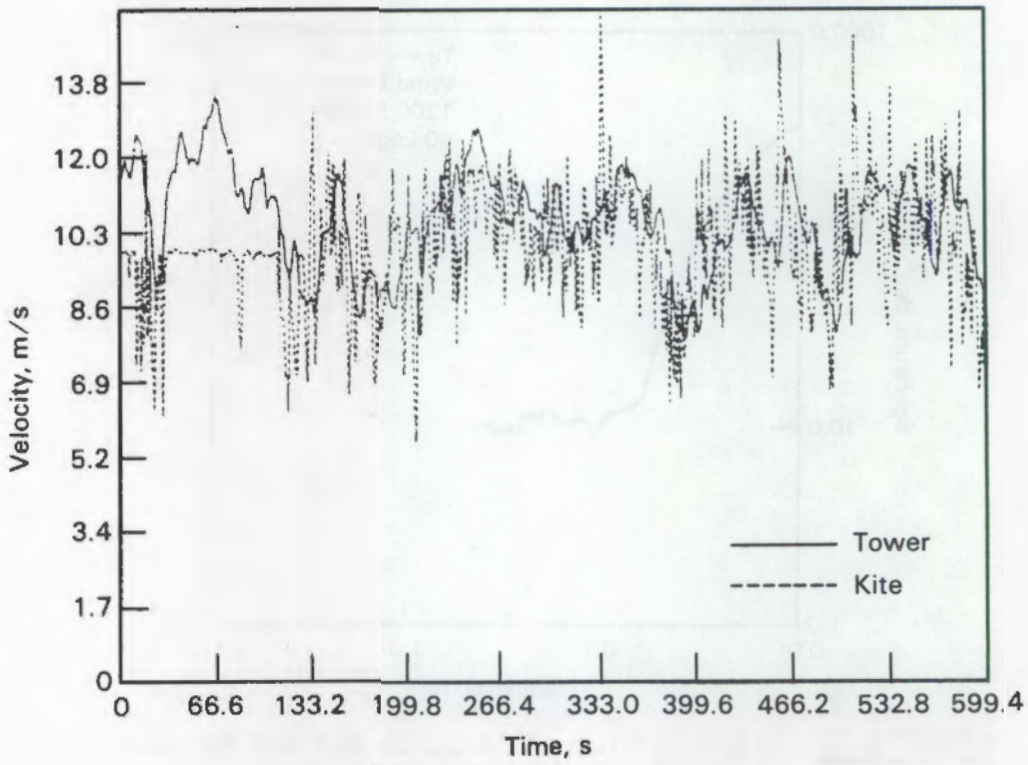

FIGURE 5.13. Kite Run 2 Tower and Kite Velocity Versus Time

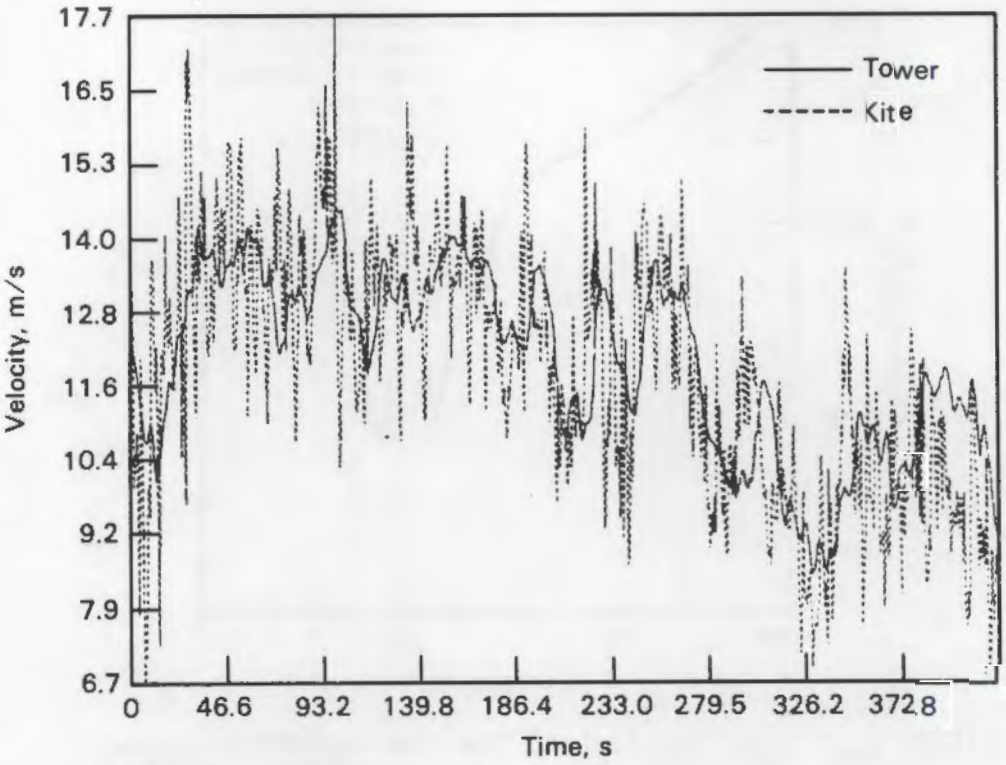

FIGURE 5.14. Kite Run 3 Tower and Kite Velocity Versus Time

TABLE 5.2. Mean and Standard Deviation of Kite Anemometer and Tower Data Runs 2 and 3

		Mean (m/s)	Standard Deviation (m/s)
Kite	Run 2	9.96	1.3685
	Run 3	11.79	2.0580
Tower	Run 2	10.60	1.1812
	Run 3	11.96	1.4998

Table 5.2 shows that the mean wind speeds from the tower and the kite are in reasonable agreement and that they are relatively strong winds. The standard deviation values presented in Table 5.2 are also reasonable; kite values are higher than the tower values as shown on the time-series Figures 5.13 and 5.14.

Figures 5.15 and 5.16 show the kite anemometer spectral analysis results with the tower spectral analysis results for Run 2 wind-speed data. A line with a slope of -5/3 has been drawn on both figures. The results on both figures generally follow the -5/3 slope; this agreement indicates that the spectral analysis results are correct and coherent. On Figures 5.15 and 5.16, the tower results fall off faster than the -5/3 slope from where the frequency readings are greater than 0.04 Hz. This occurs because the cups of the anemometer on the tower were not responding to the higher frequency fluctuations in the wind speed. On the other hand, when the frequency readings are greater than 0.04 Hz, the kite results show more energy than the -5/3 law. This energy does not come from the turbulence in the wind field; it is believed to come from another energy source. Given the kite's random movement on the films and the high energy within the kite spectrum on Figures 5.15 and 5.16, it appears that the kite is responding not only to the turbulence in the wind, but also to the shed vortex motion from its bluff body shape.

Bearman (1984) has studied the vortex-shedding effect on bluff bodies. When placed in a fluid steam, some bodies generate separated flow over a substantial proportion of their surface and hence can be classified as bluff. The TALA kite is in the category of bluff bodies. Vortex shedding and general wake turbulence induce fluctuating pressures on the surface of the generating

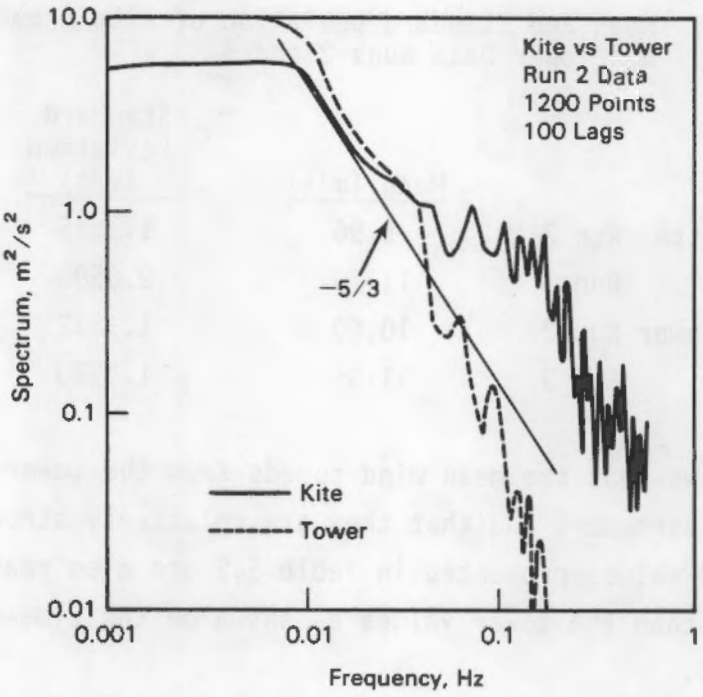

FIGURE 5.15. Log-Log Plot of Spectrum Against Frequency, Kite Versus Tower Run 2

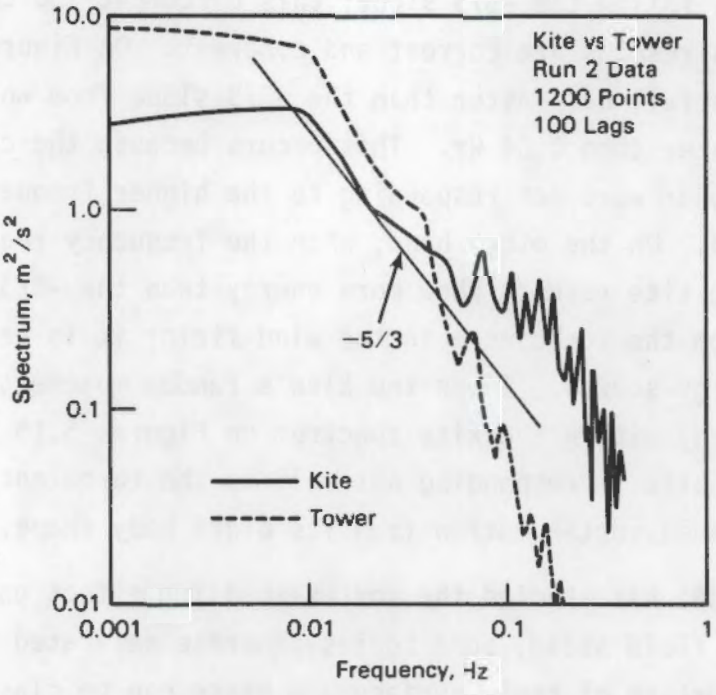

FIGURE 5.16. Log-Log Plot of Spectral Density Against Frequency, Kite Versus Tower Run 2

bluff body, and if the body is flexible these fluctuating pressures can cause oscillations. Oscillations excited by vortex shedding are usually in a direction normal to that of the free stream, and amplitudes as large as 1.5 and 2 body diameters may be recorded. Movements of a bluff body that develop exciting forces in phase with the body's velocity may also lead to large oscillation amplitudes. Galloping is one case of instability whereby some bluff bodies can extract energy from a fluid steam and sustain oscillations. Bluff body vortex shedding is believed to be the cause of the unexpected energy in the kite spectrum seen on Figures 5.15 and 5.16. The frequency range of shedding from the kite is from 0.04 to 0.8 Hz. The Strouhal number range is from $1.22 \times 10^{-3} \leq S \leq 0.24$, where $S = F_d/U$. These Strouhal numbers are lower than those observed from rigid bodies. There is insufficient experimental data available from flexibly mounted non-rigid bodies, such as kites, to provide independent evidence of the observations in these experiments.

Daniels (1984) has shown a typical Fourier analysis for a kite flying at low altitude and presented it in a dimensionless form (see Figure 5.17). Oimensionless wind speed spectral analysis results of the kite anemometer

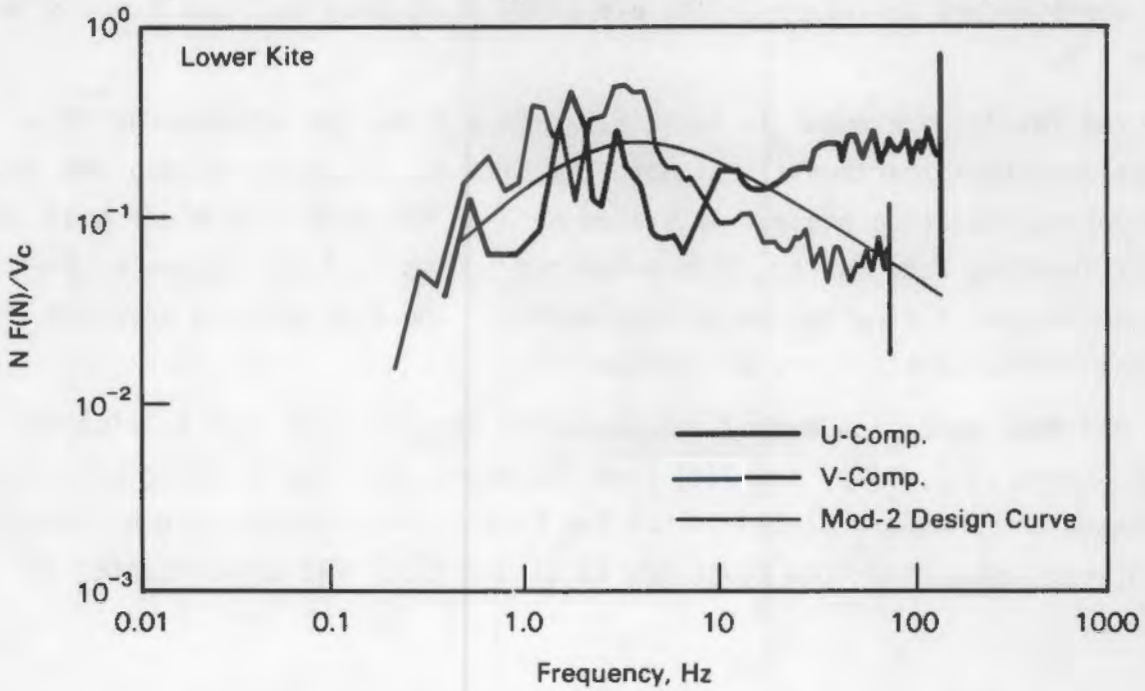

FIGURE 5.17. Spectral Analysis Results (Daniels 1984)

Runs 2 and 3 were plotted with the Daniels results against time in Figures 5.18 and 5.19. Similar high-frequency response for the kite spectra is also observed in these data.

In Chapter 3, the response of the TALA kite as a function of the fluctuating elevation angle is presented as Equation (3.14):

$$\theta' = \frac{\left(\frac{C_l}{C_d} - \tan\theta\right)\frac{2u}{U} + \left(\frac{C_{l,\alpha}}{C_d} - \frac{C_{d,\alpha}}{C_d}\tan\theta\right)\left(\frac{v}{U}\right)}{\left(\tan\theta\,\frac{C_{d,\alpha}}{C_d} + \sec^2\theta - \frac{C_{l,\alpha}}{C_d}\right)\left(1 + \frac{2u}{U}\right) + \frac{C_{d,\alpha}}{C_d}\sec^2\theta\left(\frac{v}{U}\right)} \qquad (3.14)$$

where u is the standard deviation of the tower Runs 2 and 3 wind speed, and U is the mean tower Runs 2 and 3 wind speed in Table 5.2. Thus u/U can be easily calculated from the data listed in Table 5.2; v/U = 0.52 u/U, $C_l = \sin 2\alpha$, $C_d = \sin 2\alpha$, $C_{l,\alpha} = 2\cos 2\alpha$, and $C_{d,\alpha} = \sin 2\alpha$ are the same as presented in Chapter 3. From the Runs 2 and 3 elevation angle data, the mean and the standard deviation of the kite's elevation angle can be found. Thus the fluctuating elevation angle of Runs 2 and 3 can be calculated and can be compared with the standard deviation of the elevation angle data for Runs 2 and 3 in Table 5.3.

The results presented in Table 5.3 show a large gap between the theoretical and the experimental values. Equation (3.14) overpredicted the kite's fluctuating elevation angle. As stated before, the kite is a bluff body and vortex shedding acts on it. This makes the analysis of the motion of the kite in turbulent flow extremely complicated. The poor results shown in Table 5.3 are therefore not a surprise.

The data reduction method introduced in Chapter 2 is used to find the displacement X(t), Y(t), and Z(t) from the digitized film of the kite's motion. The means and standard deviations of the kite's displacements for both Runs 2 and 3 were calculated from Equations (5.1) and (5.2) and are presented in Table 5.4.

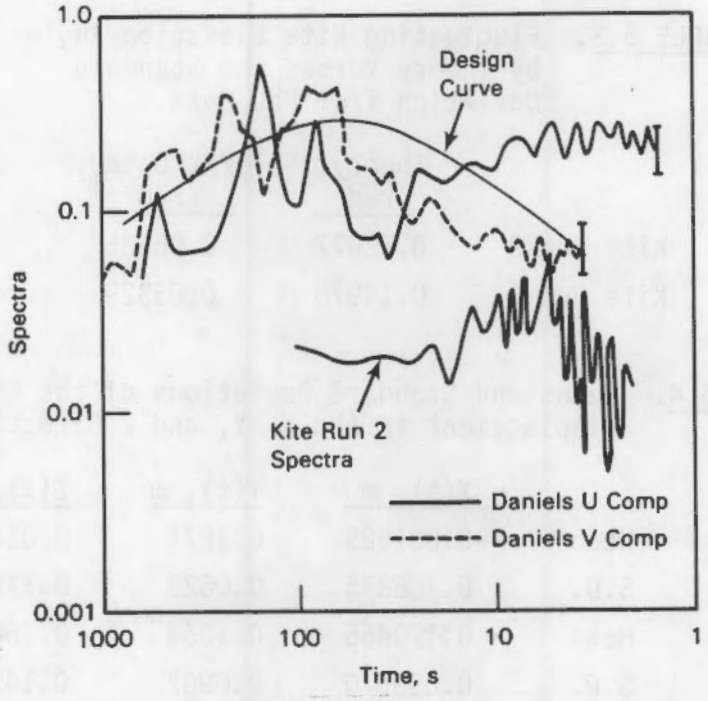

FIGURE 5.18. Kite Run 2 Versus Daniels Dimensionless Wind Speed Spectra Versus Time

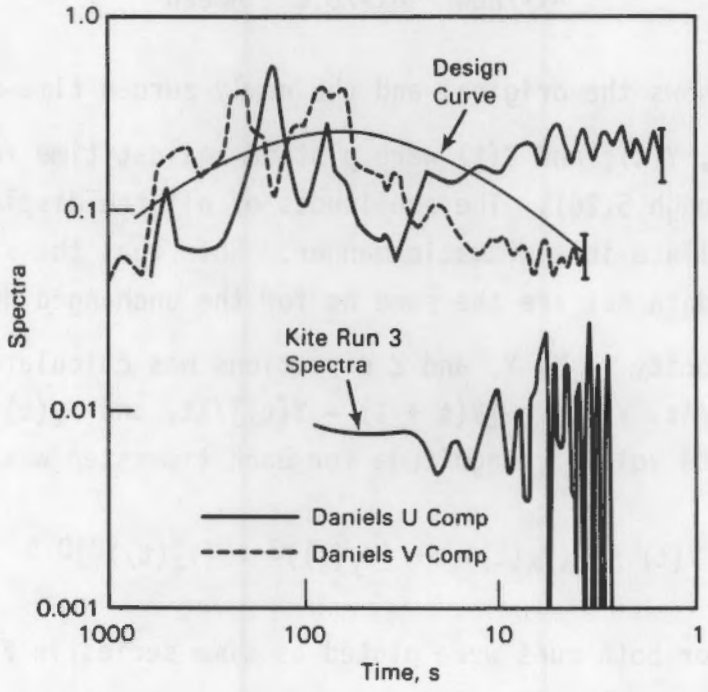

FIGURE 5.19. Kite Run 3 Versus Daniels Dimensionless Wind Speed Spectra Versus Time

TABLE 5.3. Fluctuating Kite Elevation Angle by Theory Versus the Standard Deviation from PNL Data

	Theory, rad	PNL Data, rad
Kite Run 2	0.12077	0.06486
Kite Run 3	0.14970	0.05329

TABLE 5.4. Means and Standard Deviations of the Kite's Displacement in the X, Y, and Z Direction

		X(t), m	Y(t), m	Z(t), m
Run 2	Mean	-0.061629	0.1271	0.01864
	S.D.	0.186835	0.0629	0.11528
Run 3	Mean	0.179456	0.1064	0.16097
	S.D.	0.093570	0.0967	0.14776

X(t), Y(t), and Z(t) are rezeroed by

$$X(t)_{new} = X(t)_{old} - \bar{X}_{mean} \tag{5.3}$$

and Figure 5.20 shows the original and the newly zeroed time-series curves.

The new X(t), Y(t), and Z(t) were plotted against time for Runs 2 and 3 (Figures 5.21 through 5.26). The amplitudes of all the displacement time-series plots oscillate in a dramatic manner. Note that the standard deviations for the rezeroed data set are the same as for the unchanged data set.

The kite velocity in X, Y, and Z directions was calculated from $V_x(t) = [X(t + 1) - X(t)]/\Delta t$, $V_y(t) = [Y(t + 1) - Y(t)]/\Delta t$, and $V_z(t) = [Z(t + 1) - Z(t)]/\Delta t$. The kite velocity magnitude for each time step was calculated from

$$V(t) = [(V_x(t))^2 + (V_y(t))^2 + (V_z(t))^2]^{0.5} \tag{5.4}$$

and the results for both runs were ploted as time series in Figures 5.27 and 5.28.

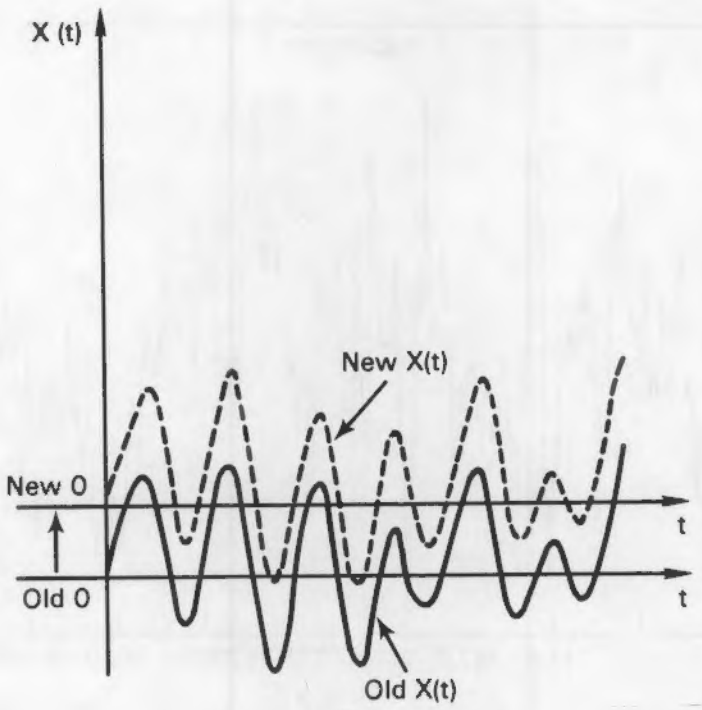

FIGURE 5.20. Rezero Time Series X(t)

For both runs, the mean and the standard deviation of the $V_X(t)$, $V_Y(t)$, and $V_Z(t)$ were obtained and their vector addition values are listed in Table 5.5. It is clear that the standard deviation values of the kite velocities of both runs are much greater than the mean values; hence, the oscillation of the kite is large. This can be seen in their time-series plots (Figures 5.27 and 5.28). Large oscillations of the kite seen on the films certainly agree with the time-series plots and the results in Table 5.5. The kite mean velocity and standard deviation values in the Y direction, which is the direction of the mean flow, U, are listed in Table 5.6.

One can see that in Tables 5.5 and 5.6 all the mean values of the kite velocity are quite small but not equal to zero. The time series X(t), Y(t), and Z(t) are calculated from the digitized kite data. When the kite sometimes left the field of view of the camera, some error was introduced into the data.

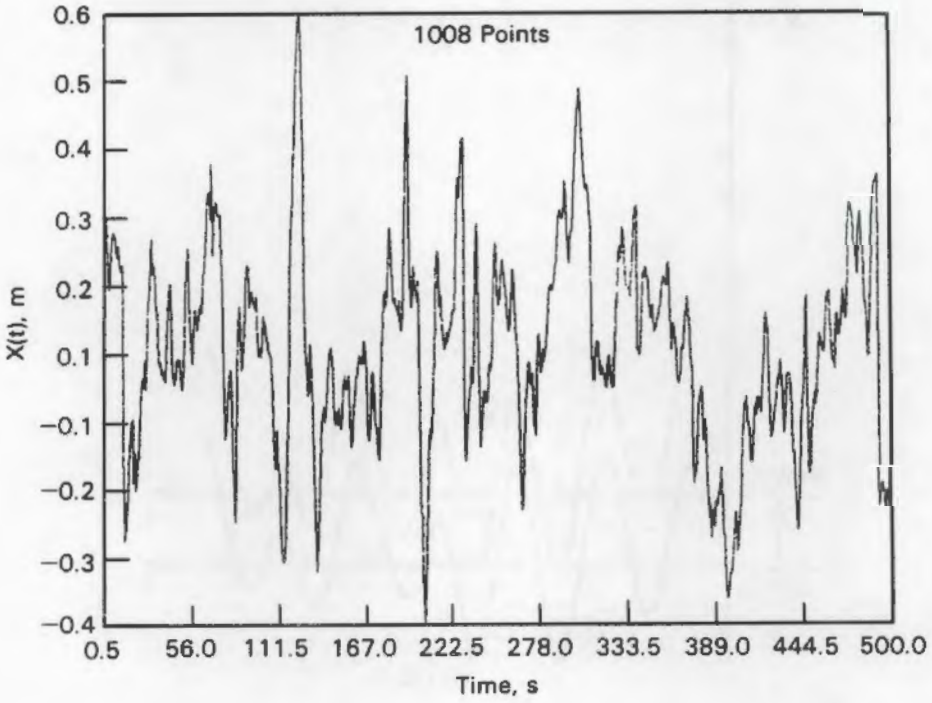

FIGURE 5.21. Kite Run 2 X(t) Time Series, 1008 Points

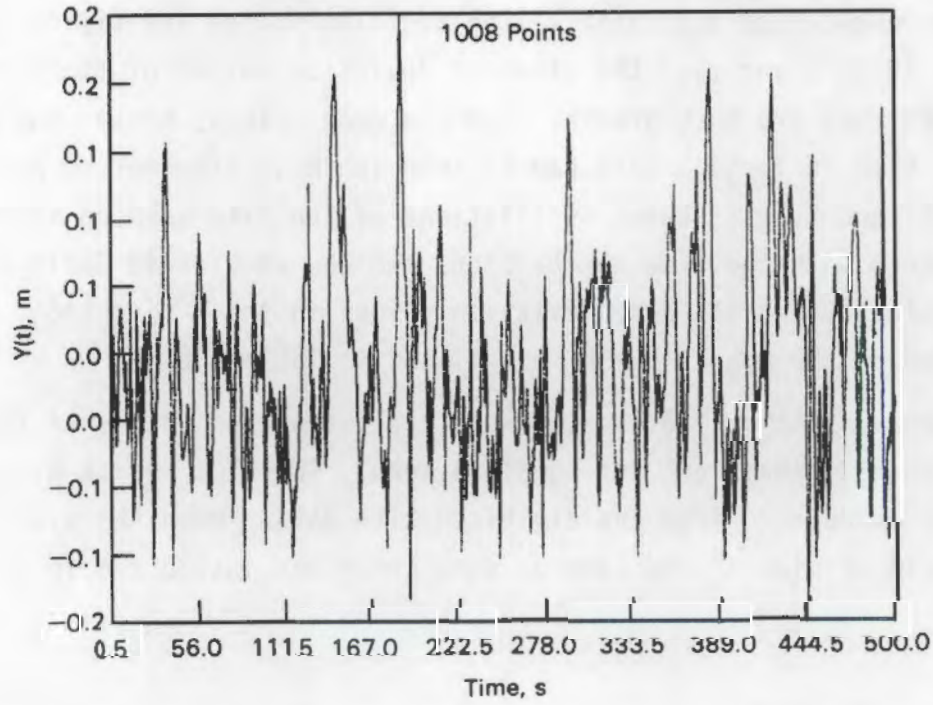

FIGURE 5.22. Kite Run 2 Y(t) Time Series, 1008 Points

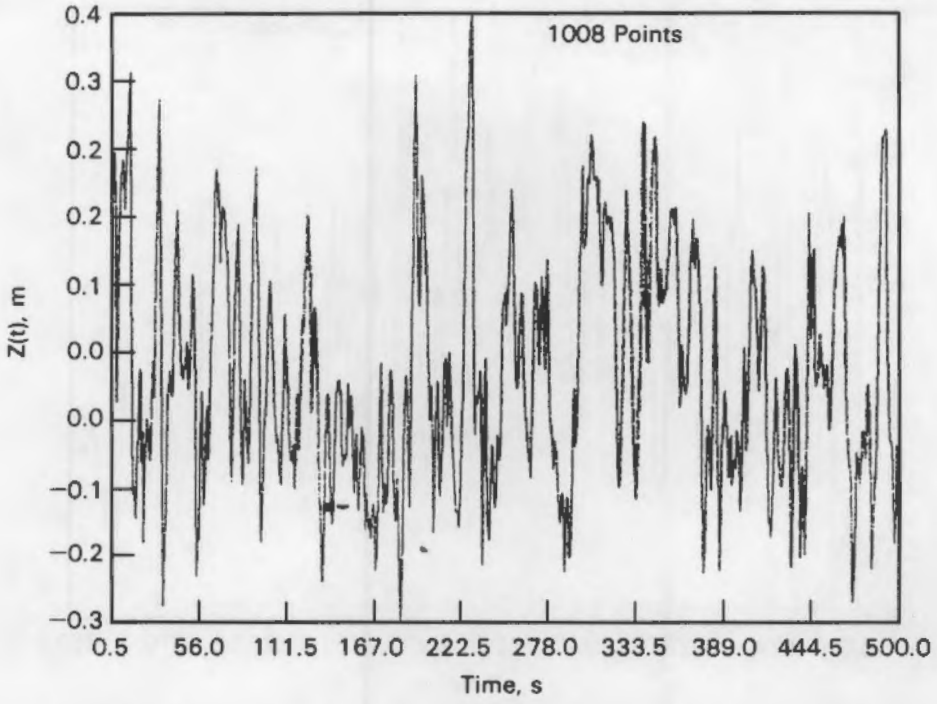

FIGURE 5.23. Kite Run 2 Z(t) Time Series, 1008 Points

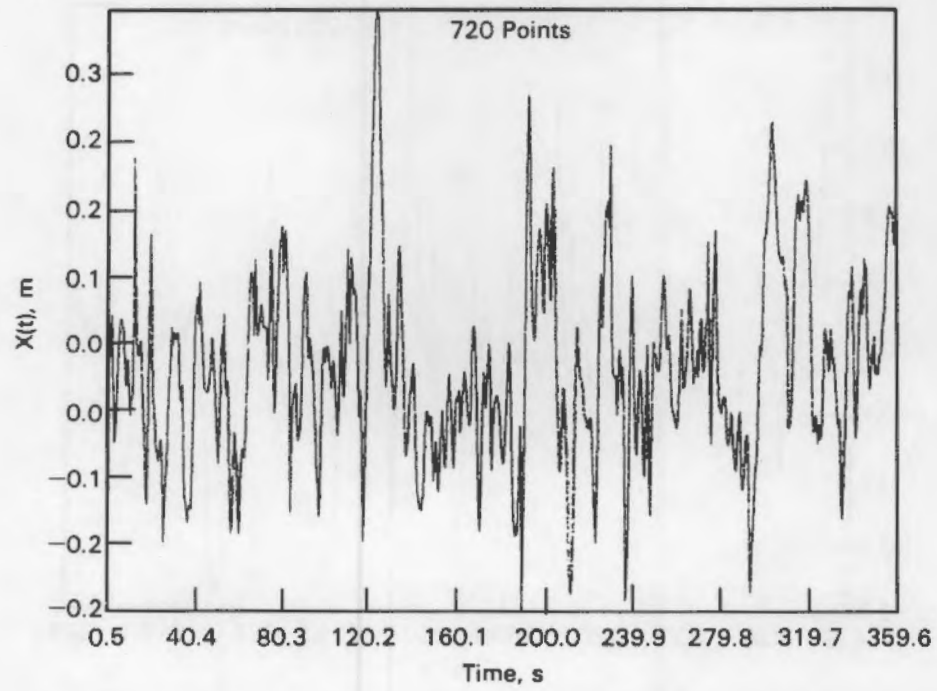

FIGURE 5.24. Kite Run 3 X(t) Time Series, 720 Points

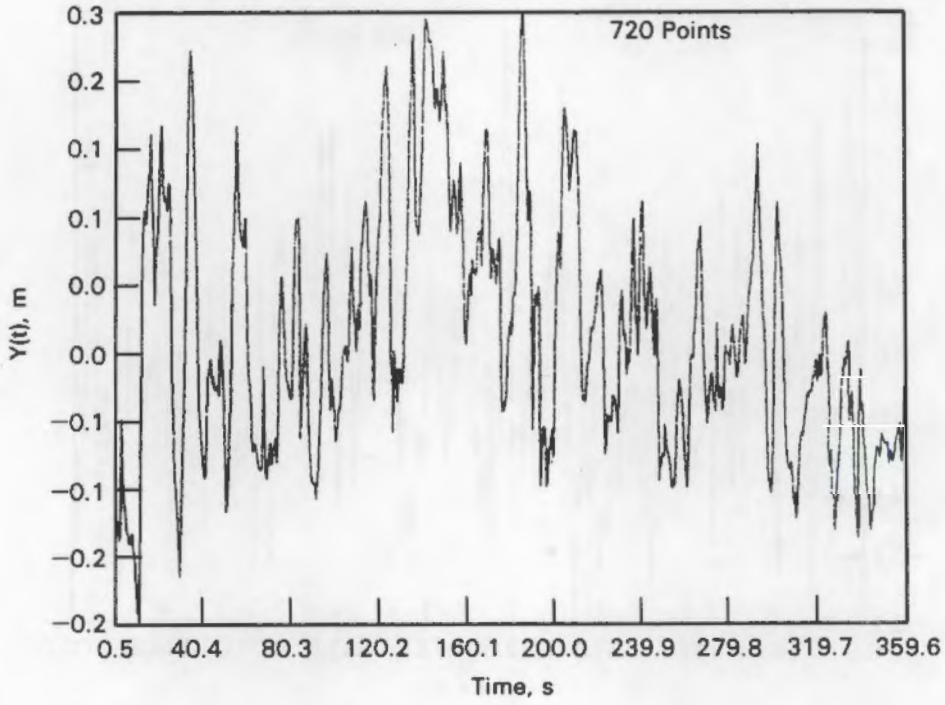

FIGURE 5.25. Kite Run 3 Y(t) Time Series, 720 Points

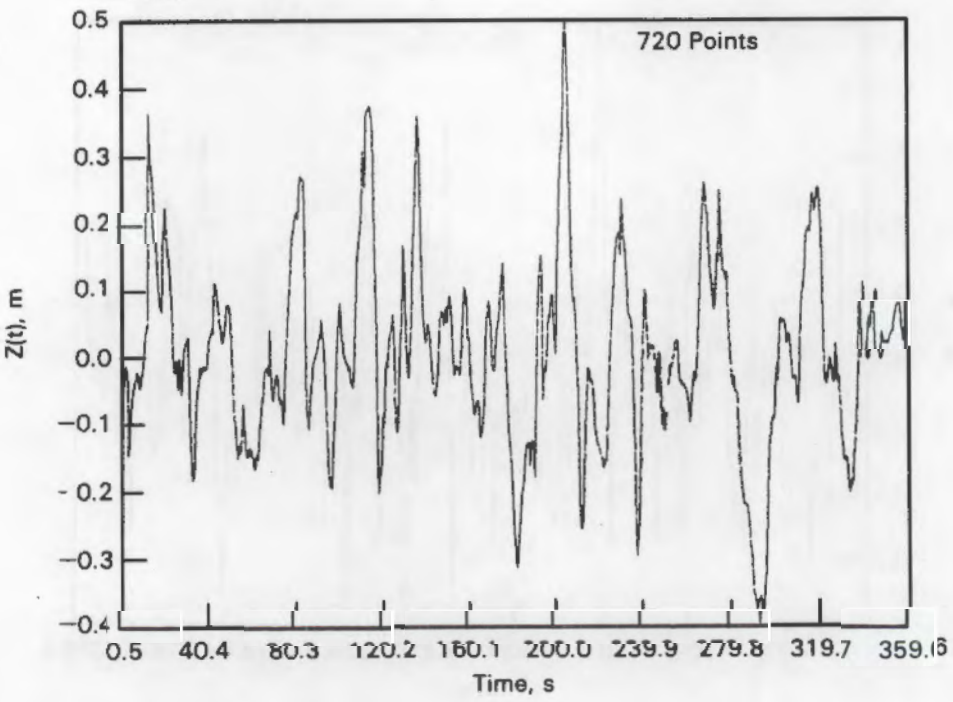

FIGURE 5.26. Kite Run 3 Z(t) Time Series, 720 Points

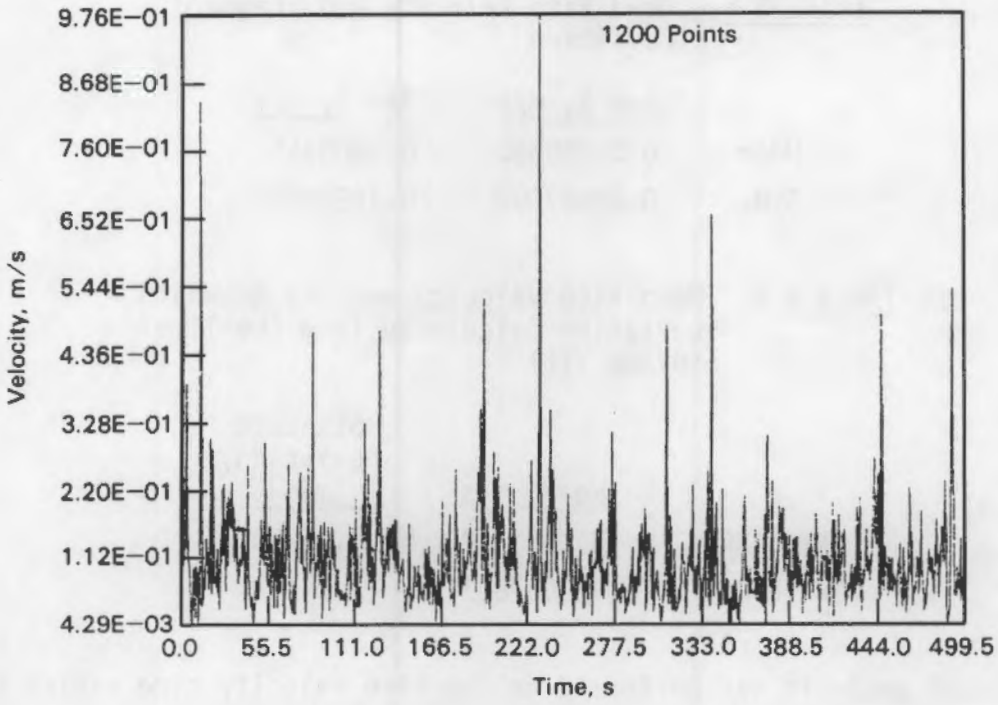

FIGURE 5.27. Kite Run 2 Velocity Time Series, 1200 Points

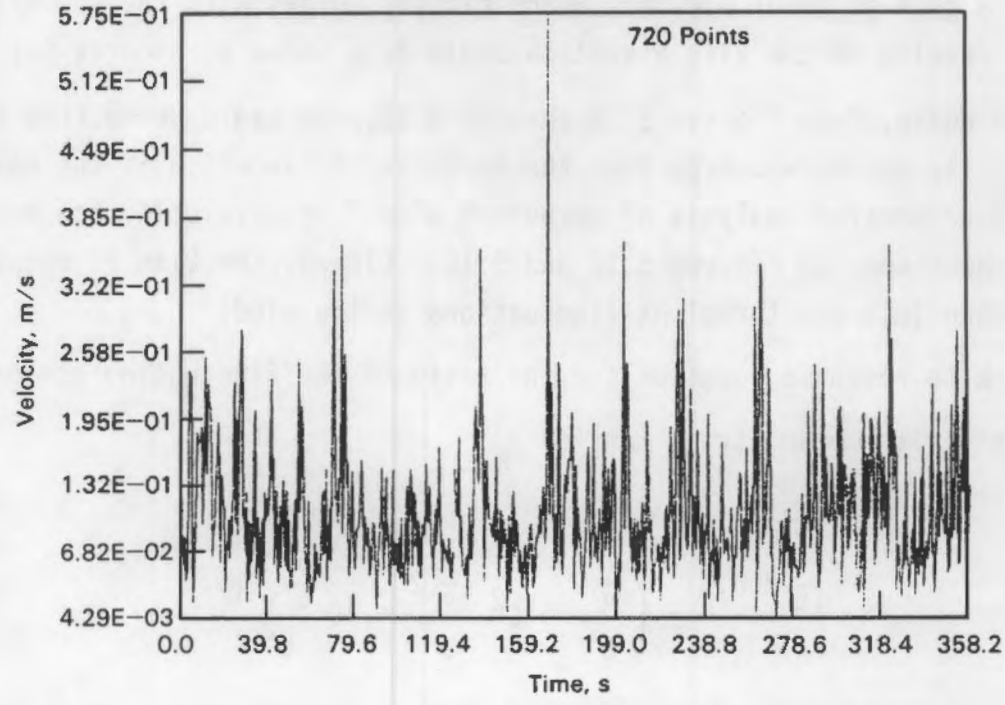

FIGURE 5.28. Kite Run 3 Velocity Time Series, 720 Points

TABLE 5.5. Mean Kite Velocity and Standard Deviation

	Run 2, m/s	Run 3, m/s
Mean	0.00059850	0.0008455
S.D.	0.22837000	0.1998480

TABLE 5.6. Mean Kite Velocity and Its Standard Deviation Calculated from the Time Series Y(t)

	Mean, m/s	Standard Deviation, m/s
Kite Run 2	0.0003232	0.16290
Kite Run 3	0.0007833	0.14380

Spectral analysis was performed on the kite velocity time series V(t) (which is calculated from kite displacement time series X(t), Y(t), and Z(t) as determined from the digitized film records, and the results were graphed (Figures 5.29 to 5.32). For Run 2 there is a peak at 0.017 Hz and for Run 3 there is a peak at about 0.02 Hz, which closely agrees with the spectral analysis results of the kite elevation-angle data shown in Figures 5.1 to 5.4.

Once again, from Figures 5.29 through 5.32, one can observe that the kite velocity has more energy than the normal -5/3 law which is the usual result of a spectral analysis of turbulent wind. Kite velocity has more energy has also been seen on Figures 5.15 and 5.16. Clearly the kite is responding to more than just the turbulent fluctuations in the wind.

The kite response equation for the ratio of the fluctuating string and tension t' to the mean string tension T

$$\frac{(\bar{t}'^2)^{0.5}}{\bar{T}} = \left(\frac{4\bar{u}'^2}{U^2} + C^2\,\frac{\bar{v}'^2}{U^2} + 4C\,\frac{\overline{u'v'}}{U^2}\right)^{0.5} \qquad (3.12)$$

are now examined and the result is checked with the experimental results.

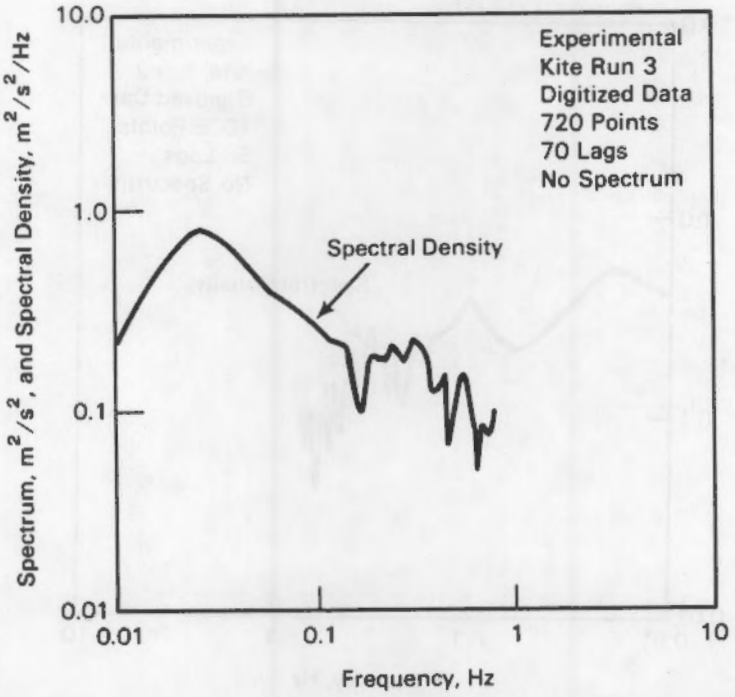

FIGURE 5.29. Log-Log Plot of Spectrum and Spectral Density Versus Frequency, Experimental Kite Run 3, 70 Lags

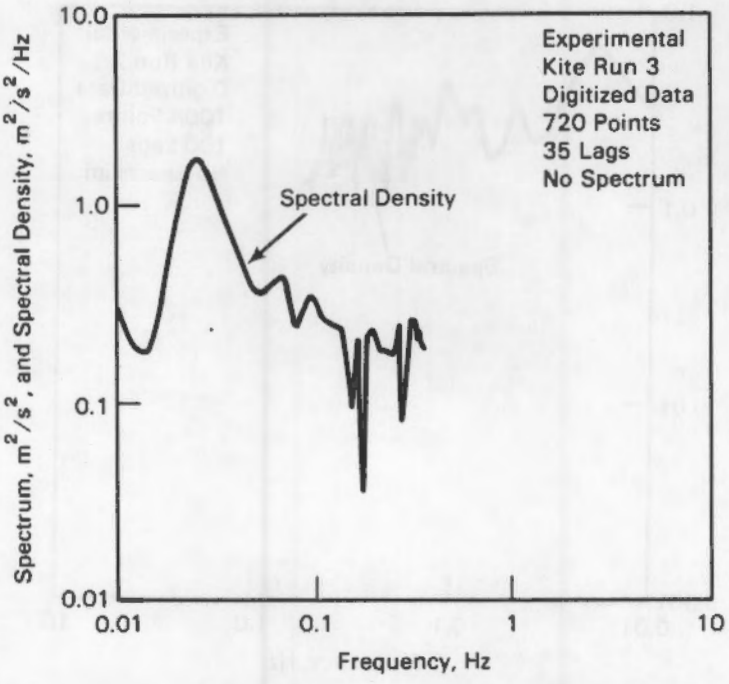

FIGURE 5.30. Log-Log Plot of Spectrum and Spectral Density Versus Frequency, Experimental Kite Run 3, 35 Lags

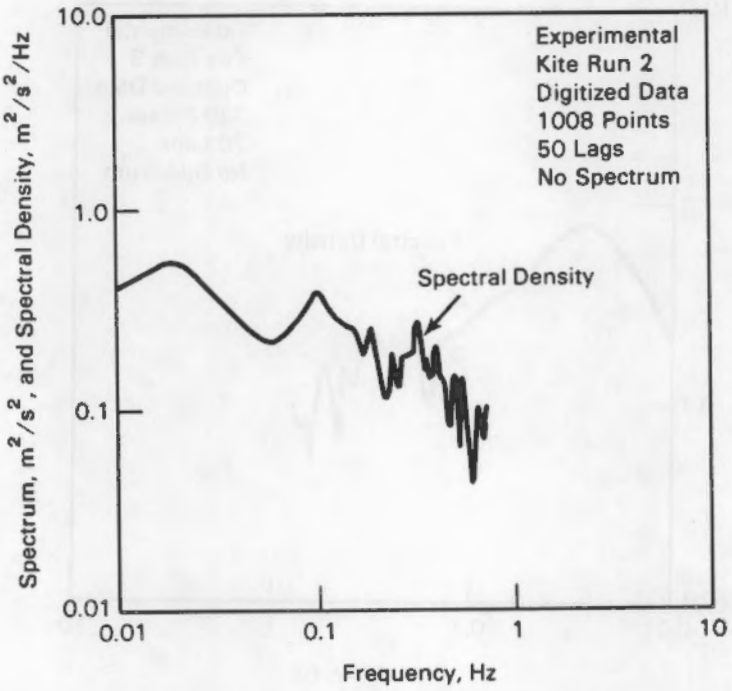

FIGURE 5.31. Log-Log Plot of Spectrum and Spectral Density Versus Frequency, Experimental Kite Run 2, 50 Lags

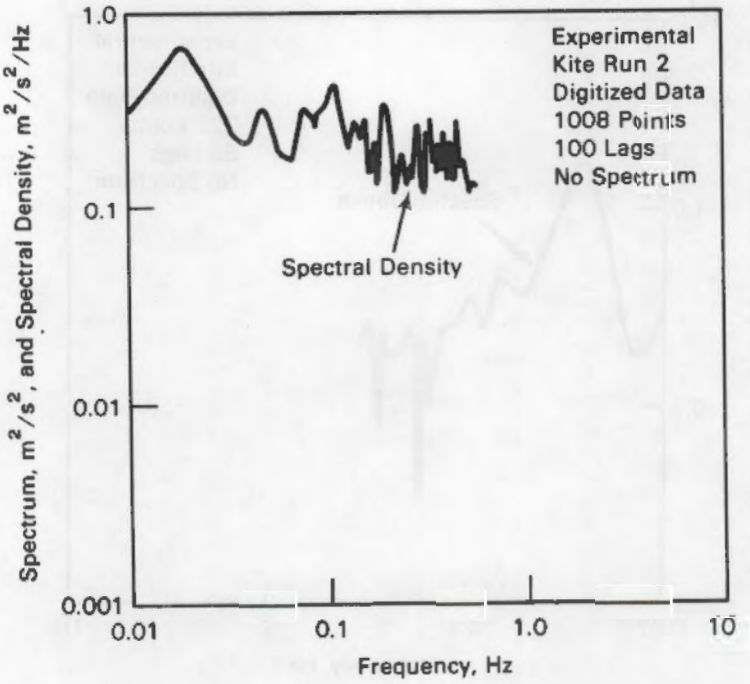

FIGURE 5.32. Log-Log Plot of Spectrum and Spectral Density Versus Frequency, Experimental Kite Run 2, 100 Lags

Recall that in Equation (3.12)

$$C = \left[\frac{\cos^2\bar{\theta}}{C_d(\bar{\alpha})}\left(\frac{\partial C_d}{\partial \alpha}\right)_{\bar{\alpha}} + \frac{\sin^2\bar{\theta}}{C_l(\bar{\alpha})}\left(\frac{\partial C_l}{\partial \alpha}\right)_{\bar{\alpha}}\right]$$

and

$$\frac{u'}{U} = \frac{u}{U} + \frac{l\omega\sin\alpha}{U}$$

$$\frac{v'}{U} = \frac{v}{U} + \frac{l\omega\cos\alpha}{U} .$$

As declared in Chapter 3, fluctuating tension (t') is a function of the turbulent fluctuation (u,v) and the kite motion ($l\omega$), where l is the string length, and Figure 5.33 is sketched as an extension of Figure 3.2 in Chapter 3.

From Figure 5.33, the relation between ω and θ can be written as

$$l\omega\Delta t = \Delta\theta l . \qquad (5.5)$$

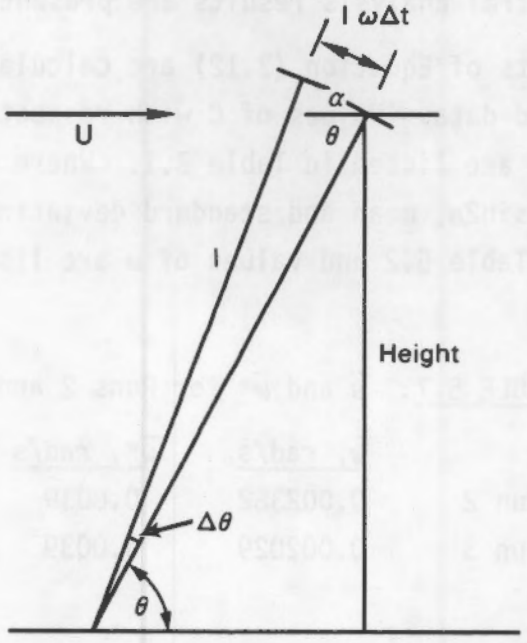

FIGURE 5.33. Relationship Between θ and ω

Equation (5.5) can be rewritten as

$$\omega = \frac{\Delta\theta}{\Delta t} \quad . \tag{5.6}$$

The equation to calculate $\bar{\omega}$ is

$$\bar{\omega} = \sum_{i=1}^{N} [(\theta_{i+1} - \theta_i)/\Delta t]/N \tag{5.7}$$

where R is the rate at which the data was taken. In our case, the rate is 2 data/s, so Δt equals 0.5 s. This is a necessary step to obtain the values of the kite motion $l\omega$. Without it the response equation for the kite [Equation (3.12)] cannot be calculated.

Spectral analysis of the kite elevation Runs 2 and 3 data using 80 lags gives the largest spectral density values at about 0.025 Hz for both runs. The spectral density values have been converted and equal about 0.0039 rad/s.

The $\bar{\omega}$ values calculated from Equation (5.7) and the peak value of $\bar{\omega}$ ($\bar{\omega}^*$) obtained from the spectral analysis results are presented in Table 5.7.

Theoretical results of Equation (3.12) are calculated from the tower Runs 2 and 3 wind-speed data. Values of C with respect to the angle of attack or the elevation angle are listed in Table 3.1. Where $C_l = \sin 2\alpha$, $C_d = \sin 2\alpha$, $C_{l,\alpha} = 2\cos 2\alpha$, $C_{d,\alpha} = \sin 2\alpha$, mean and standard deviation of the wind speed U and u can be found in Table 5.2 and values of ω are listed in Table 5.7.

TABLE 5.7. $\bar{\omega}$ and $\bar{\omega}^*$ for Runs 2 and 3

	$\bar{\omega}$, rad/s	$\bar{\omega}^*$, rad/s
Run 2	0.002382	0.0039
Run 3	0.002029	0.0039

Relationships between u, v and uv, $\overline{uv}$ are given by Teunissen (1970) as

$$\frac{v}{U} = 0.52 \frac{u}{U}$$

and

$$\overline{uv} = (-3.1)uv \ .$$

For the tower Runs 2 and 3, the tower information excludes the kite motion ($l\omega$); thus, the kite motion ($l\omega$) was not included in the calculation of the rms string tension t'. The results for the tower run are listed in Table 5.8. However, in order to compare the theoretical results of Equation (3.12) with the experimental kite response results (because the experimental kite response results do include the kite motion), kite motion $l\omega$ should be included in the calculation of Equation (3.12). Since we know the length of the tether (l) is 53.88 m and the values of ω (Table 5.7), results of Equation (3.12) were calculated from the tower data (with the kite motion $l\omega$) and listed in Table 5.9.

The amount of fluctuation in the kite-measured wind speed, as the kite's response to turbulence, can be represented as a fluctuating tension, t', in the string. Therefore, to calculate experimental RMS $t'/\bar{T}$ of the kite, each variable in the kite anemometer wind speed data (Runs 2 and 3) is squared, means and standard deviations of the squared data are calculated, and the ratios of the mean to the standard deviation as the experimental RMS $t'/\bar{T}$ are calculated and listed.

TABLE 5.8. RMS t' for Tower Data

	$\bar{U}$	$\bar{u}/U$	$\bar{v}/U$	$\frac{(\bar{t}^2)^{0.5}}{\bar{T}}$
Run 2	10.612	0.11131	0.0556	0.2116558
Run 3	11.9618	0.12538	0.0629	0.2384000

TABLE 5.9. RMS t' for Kite Anemometer from Equation (3.12)

	$\bar{U}$	u/U	v/U	$\bar{\omega}$	$\frac{(\bar{t}^2)^{0.5}}{\bar{T}}$
Run 2	10.612	0.1113	0.05789	0.002382	0.229963
	10.612	0.1113	0.05789	0.0039(a)	0.241621
Run 3	11.962	0.1254	0.06519	0.002029	0.252400
	11.962	0.1254	0.06519	0.0039(a)	0.265240

(a) The peak $\bar{\omega}$.

The theoretical results for the kite string tension $[(\frac{\bar{t}^2}{\bar{T}})^{0.5}]$ (Table 5.9) were larger than the theoretical results without the kite motion (Table 5.8), and the experimental results (Table 5.10) were greater than the theoretical results with the kite motion (Table 5.9). As has been discussed, the vortex-shedding effect on the bluff-bodied kite is believed to be responsible for the gap between the theoretical and the experimental results (Tables 5.8, 5.9, and 5.10). It is believed that the experimental kite motion contains much more energy than the turbulent wind. The bluff-body kite can extract energy from the wind and sustain the oscillation already created by the turbulence in the wind.

In Chapter 2, it was indicated that Camera A records the kite's position in the Y" and Z" directions and Camera B in the X" and Z" directions. The two Z"s are cross-correlated by

$$R_{ab} = \frac{\sum_{i=1}^{N} (Z''_a(i) - \bar{Z}''_a)(Z''_b(i) - \bar{Z}''_b)}{N\delta_{za}\delta_{zb}} \qquad (5.8)$$

where N is the total number of data points and δ is the standard deviation, defined by Equation (5.2). The correlation results are shown in Table 5.11.

TABLE 5.10. Kite Experiment RMS t' Value

	$\frac{(\bar{t}^2)^{0.5}}{T}$
Run 2	0.27429
Run 3	0.33673

TABLE 5.11. Correlation Between the Two Z"s for Both Runs 2 and 3

	$\sum Z_1''$	$\sum Z_2''$	Z_1''	Z_2'	R_{12}
Run 2	0.125	0.14748	0.03258	-0.07324	0.00188
Run 3	0.124	0.13200	-0.00235	-0.09000	-0.003479

Table 5.11 shows that the vertical kite readings (Z" values) from Cameras A and B are not correlated. A few sources may contribute to the poor correlations. First, the two cameras did not start simultaneously, so the two films are not synchronized. Second, the vibrations of the running camera may cause problems. Third, the kite sometimes left the field of view of the camera. Finally, manual digitizing of the data could cause the bad correlation of the two Z"s. Therefore the averages of the two Z"s were taken and used for Z" when the displacement and velocity of the kite were calculated.

5.3 CONCLUSIONS

On the films that recorded the TALA kite motion, it is clear that the kite moves on an unpredictable path throughout the entire period. There is a great deal of oscillation in the kite movement. Spectral analysis of the kite data indicates that the bluff-body-shaped TALA kite extracts energy from wind flow in the field and sustains oscillation, vibration, and fluctuation of its own generated from the turbulence in the flow. The response equations of the kite presented here and the linear small perturbation analysis of the effect of turbulence on the motion of a kite proved incapable of describing the actual vortex-shedding effect on the kite. Lack of knowledge about the vortex-shedding effect on bluff bodies made it impossible to obtain a satisfactory explanation of how the kite responds to turbulence. Using mathematical

models to predict vortex-induced oscillations on differently shaped objects is a useful method toward solving vortex-shedding problems. However, time and research budget precluded such study at this stage.

6.0 BALLOON EXPERIMENTS AND RESULTS

6.1 INTRODUCTION

In this chapter, the same kind of analysis performed on experimental kite data is now performed on experimental balloon data. A modified TS-1 BR-X™ tethersonde balloon was flown in a field adjacent to the PNL meteorological tower. An anemometer was suspended under the balloon, and wind speed was recorded over a certain period. Figure 4.1 illustrated the balloon, which has an aspect ratio of 4:1. Two balloon runs were performed and the balloon was filmed by two 8-mm cameras simultaneously during each balloon run. The film of the first run was poor; therefore, only the second run film was digitized, and the displacement of the balloon in the X, Y, and Z directions was calculated by using the extended double theodolite theory presented in Chapter 2. Table 6.1 lists all the information on the balloon experiment.

The films and the balloon anemometer data for the first balloon run are not included in Table 6.1 because the films only contained black frames and the anemometer failed to transmit any signals. Therefore only the data for the second run are listed.

The SPSS statistical package was employed to perform spectral analysis on the balloon tower data. The balloon anemometer wind speed was compared with the balloon Run 2 tower wind-speed data. The balloon displacement results calculated from the balloon response theory presented in Chapter 4 are compared with the balloon displacement results generated from the digitized balloon data.

TABLE 6.1. Balloon Data List

Source	Experiment	Start	End	Rate	Data Points
Tower	Balloon Run 1	14:20	14:25	18 data/s	600
	Balloon Run 2	14:44	15:14	2 data/s	3600
Anemometer	Balloon Run 2	14:44	15:14	1 data/10 s	177
Film	Balloon Run 2	14:44	15:14	2 data/s	3600

6.2 ANALYSIS OF THE BALLOON EXPERIMENTAL DATA

The balloon run tower data include the wind speed and direction at 50 ft above the ground, which was also the balloon's altitude during the runs. Figures 6.1, 6.2, and 6.3 are the plots of the tower wind-direction time series of balloon Runs 2 and 3. Figure 6.1 shows that the wind direction ranged mainly in the second quadrant (90° to 180°) and Figures 6.2 and 6.3 show that the wind direction ranged from about 140° to about 330°. By inspection the dominant frequency of the wind direction is estimated from Figure 6.1 at a value of about 0.025 Hz for balloon Run 1. For balloon Run 2 spectral analysis was not able to resolve the lowest frequency peak as can be seen on Figures 6.4 through 6.7. However a secondary peak of 0.025 Hz can be seen on Figures 6.4 through 6.7.

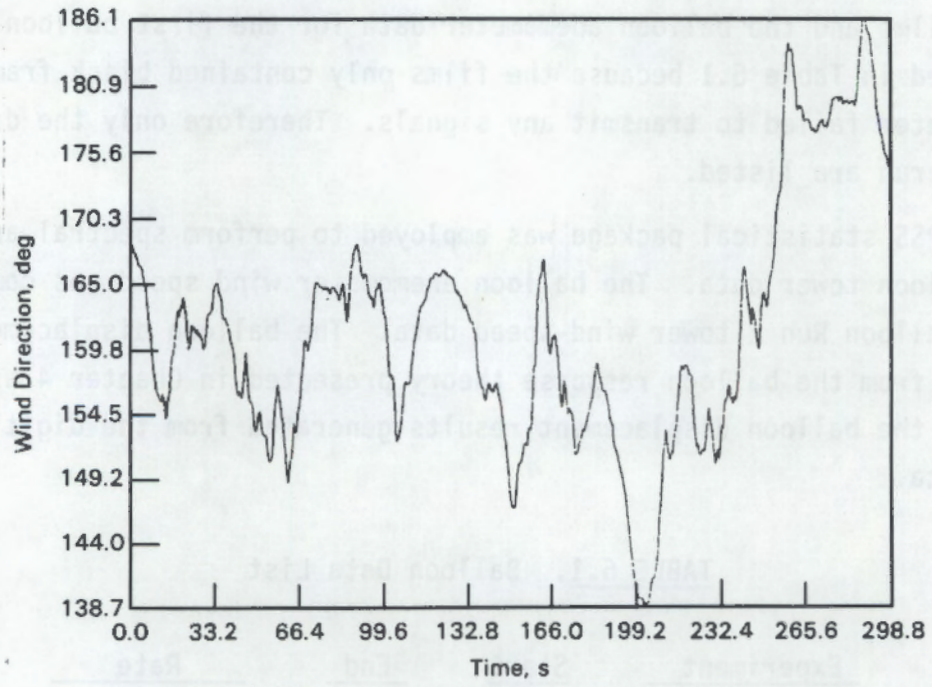

FIGURE 6.1. Wind Direction Time Series for Balloon Run 1

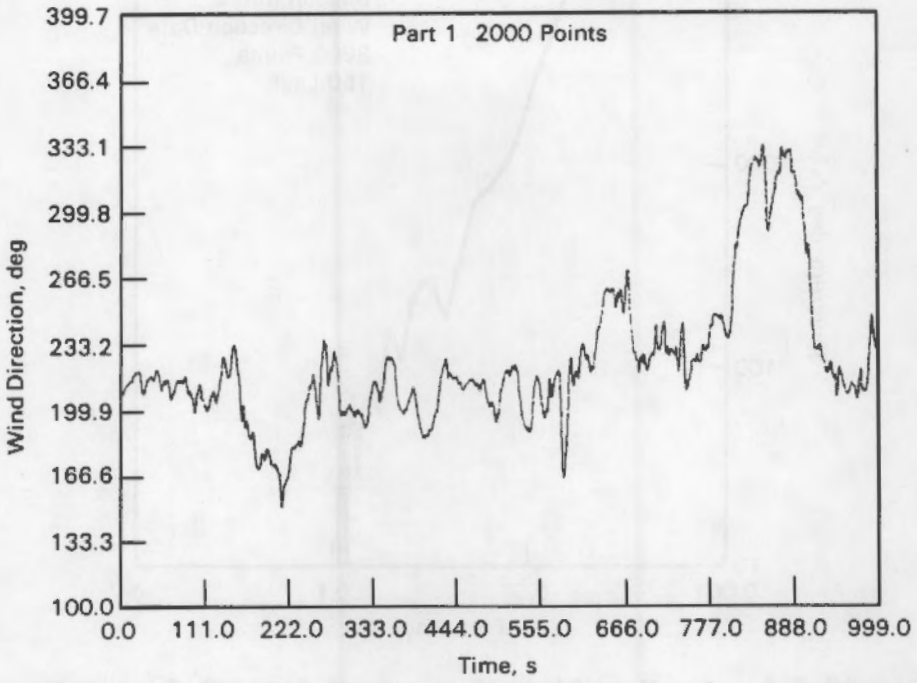

FIGURE 6.2. Wind Direction Time Series for Balloon Run 2; Part 1, 2000 Points

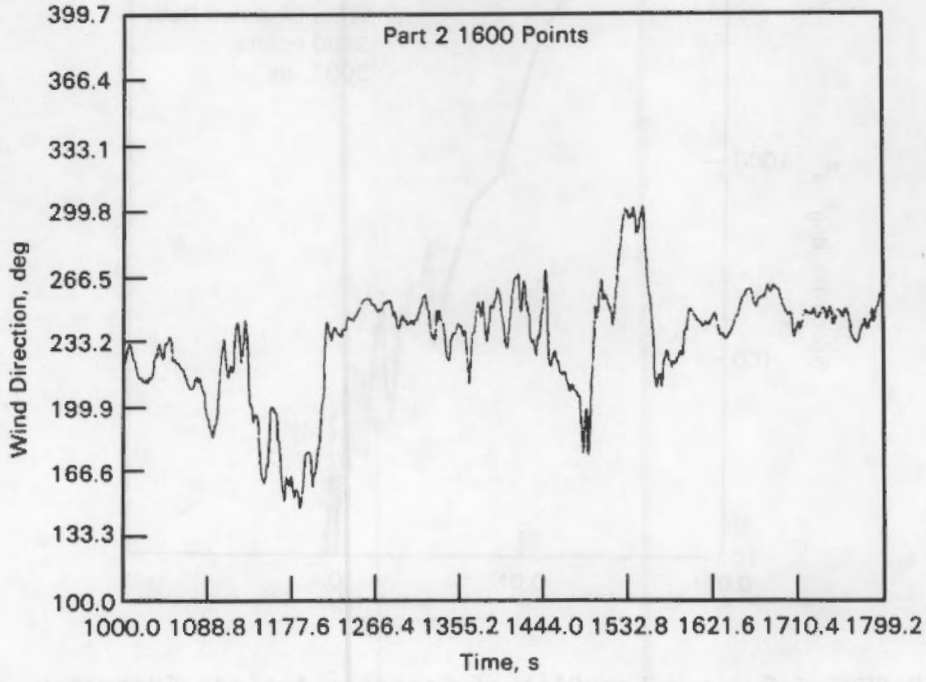

FIGURE 6.3. Wind Direction Time Series for Balloon Run 2; Part 2, 1600 Points

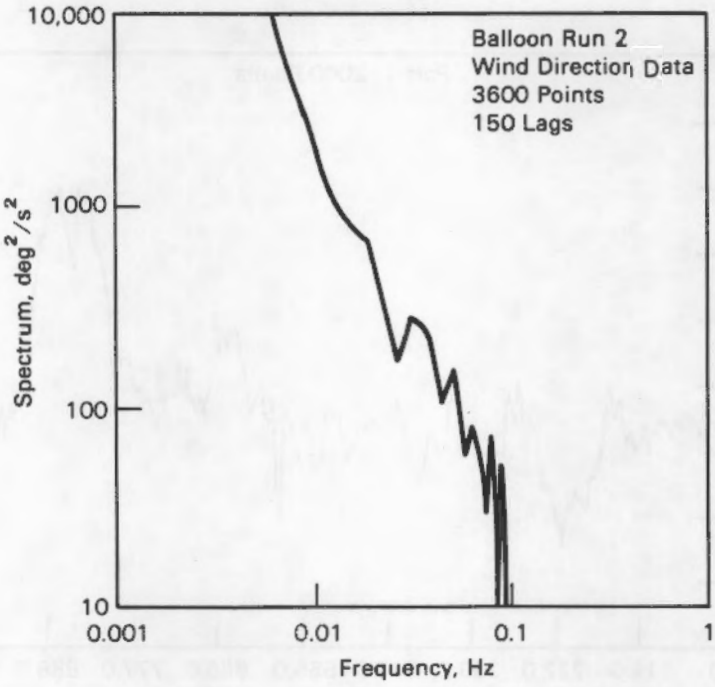

FIGURE 6.4. Log-Log Plot of Spectrum Against Frequency, Balloon Run 2, Wind Direction Data, 150 Lags

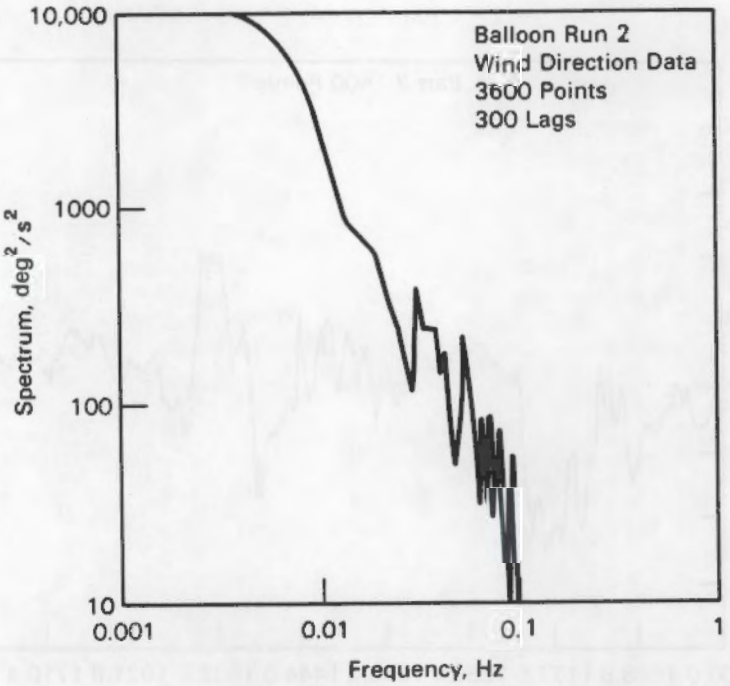

FIGURE 6.5. Log-Log Plot of Spectrum Against Frequency, Balloon Run 2, Wind Direction Data, 300 Lags

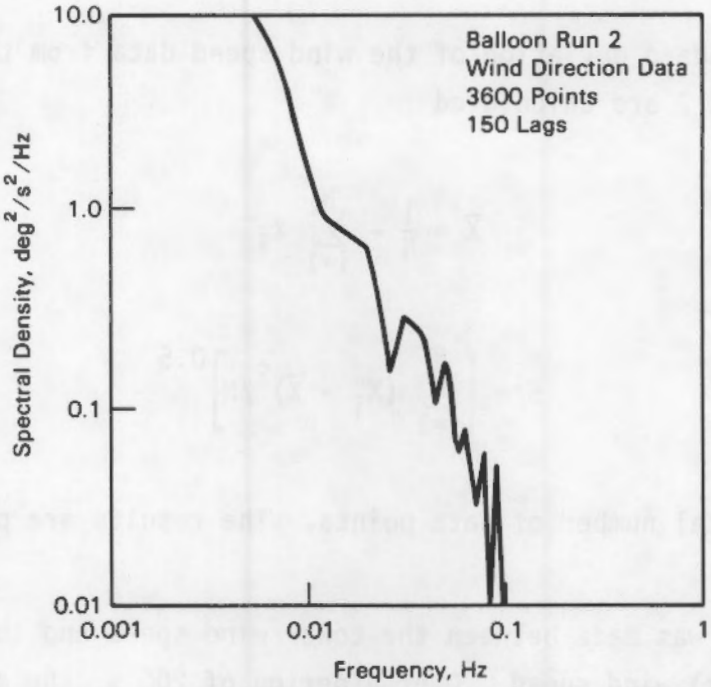

FIGURE 6.6. Log-Log Plot of Spectral Density Against Frequency, Balloon Run 2, Wind Direction Data, 150 Lags

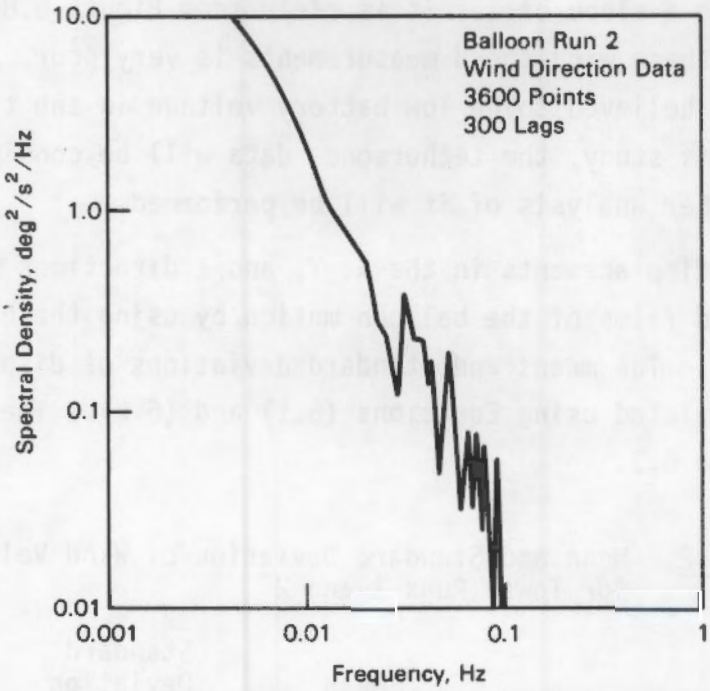

FIGURE 6.7. Log-Log Plot of Spectral Density Against Frequency, Balloon Run 2, Wind Direction Data, 300 Lags

Mean and standard deviation of the wind speed data from the tower during balloon Runs 1 and 2 are calculated

$$\bar{X} = \frac{1}{N} - \sum_{i=1}^{N} X_i \qquad (6.1)$$

$$\delta = \left[\sum_{i=1}^{N} (X_i - \bar{X})^2/N\right]^{0.5} \qquad (6.2)$$

where N is the total number of data points. The results are presented in Table 6.2.

A comparison was made between the tower wind speed and the tethersonde (ballon anemometer) wind speed. Over a period of 200 s, the mean tower wind speed was 5.96 m/s and the mean tethersonde wind speed was 3.3831 m/s. The tower wind speed was plotted against the tethersonde wind speed in Figure 6.8 for a sampling rate of one every 10 s. A perfect correlation would be a straight line with a slope of 1. It is clear from Figure 6.8 that the correlation between these wind-speed measurements is very poor. The source of the difficulty is believed to be low battery voltage in the tethersonde. For the purpose of this study, the tethersonde data will be considered to be in error and no further analysis of it will be performed.

The balloon displacements in the X, Y, and Z directions were calculated from the digitized films of the balloon motion by using the extended double theodolite theory. The means and standard deviations of displacements of the balloon were calculated using Equations (6.1) and (6.2). The results are presented in Table 6.3.

TABLE 6.2. Mean and Standard Deviation of Wind Velocity for Tower Runs 1 and 2

	Mean	Standard Deviation
Tower Run 1	11.46	2.1471
Tower Run 2	5.96	2.7655

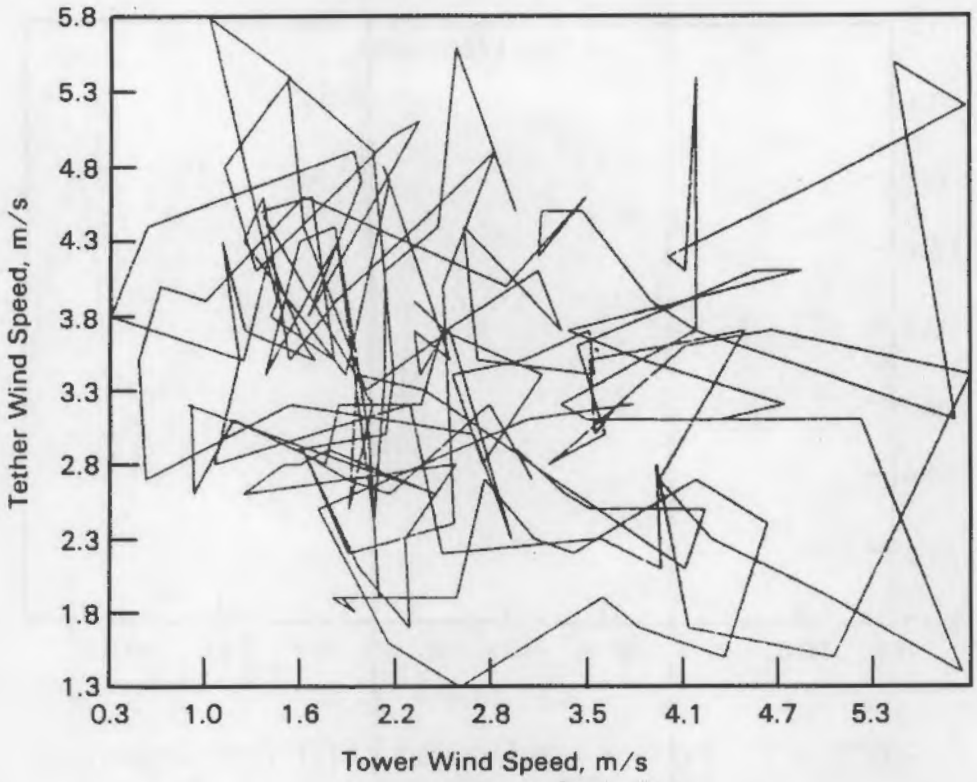

FIGURE 6.8. Balloon Wind Velocity: Tether Versus Tower

TABLE 6.3. Mean and Standard Deviation of the Balloon Displacement from the Digitized Balloon Data

	X(t), m	Y(t), m	Z(t), m
Mean	0.2336	0.1242	0.2414
S.D.	0.1879	0.1333	0.1438

Equation (5.3) was employed to calculate the new zeroed balloon displacement time series X(t), Y(t), and Z(t), and the results are presented in Figures 6.9 through 6.14. The purpose of zeroing the time series is to neglect the D.C. values in the time series. Mean and standard deviation again are calculated for the new zeroed time series and the results are listed in Table 6.4.

The means and the standard deviations of the velocities $V_x(t)$, $V_y(t)$, and $V_z(t)$ were calculated, and their values by vector addition are listed in Table 6.5.

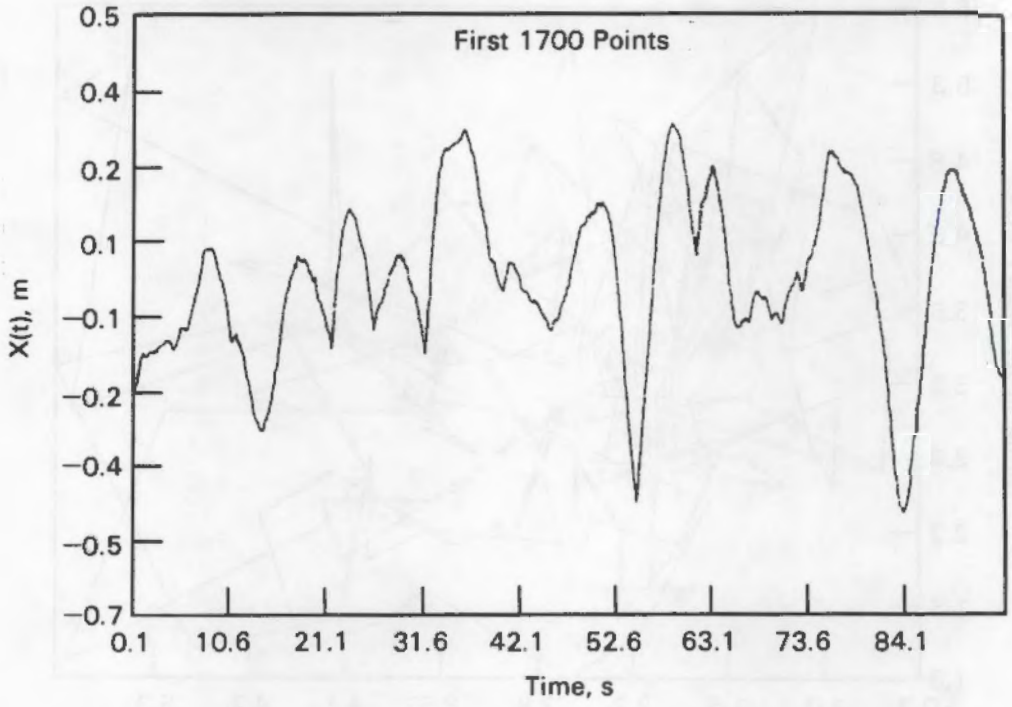

FIGURE 6.9. Balloon Displacement, X(t) Time Series, First 1700 Points

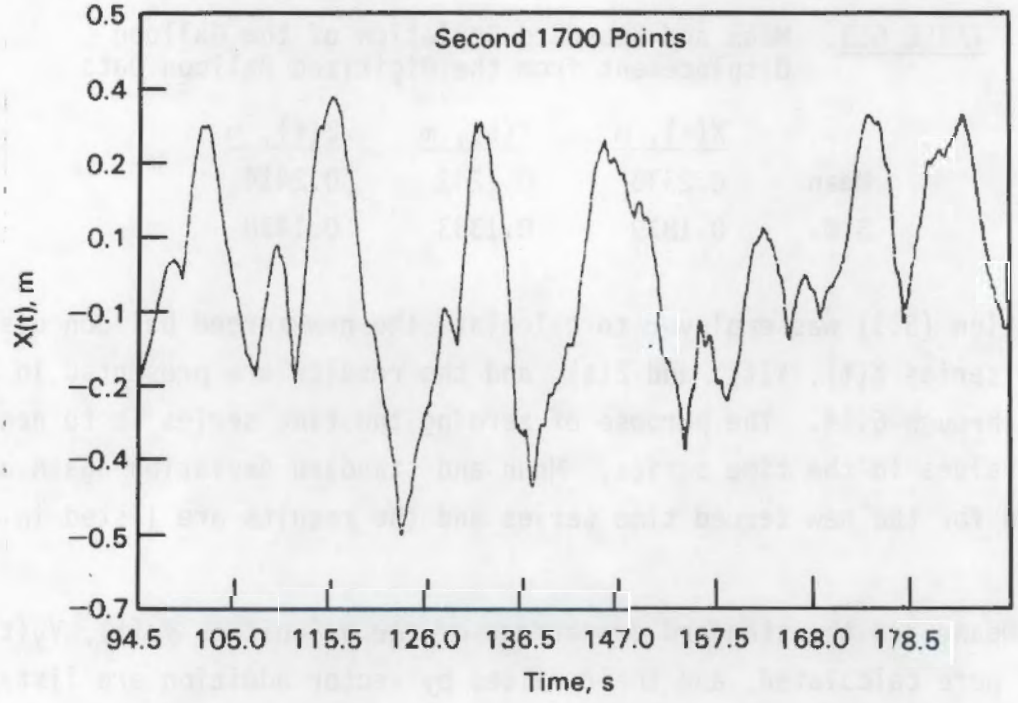

FIGURE 6.10. Balloon Displacement, X(t) Time Series, Second 1700 Points

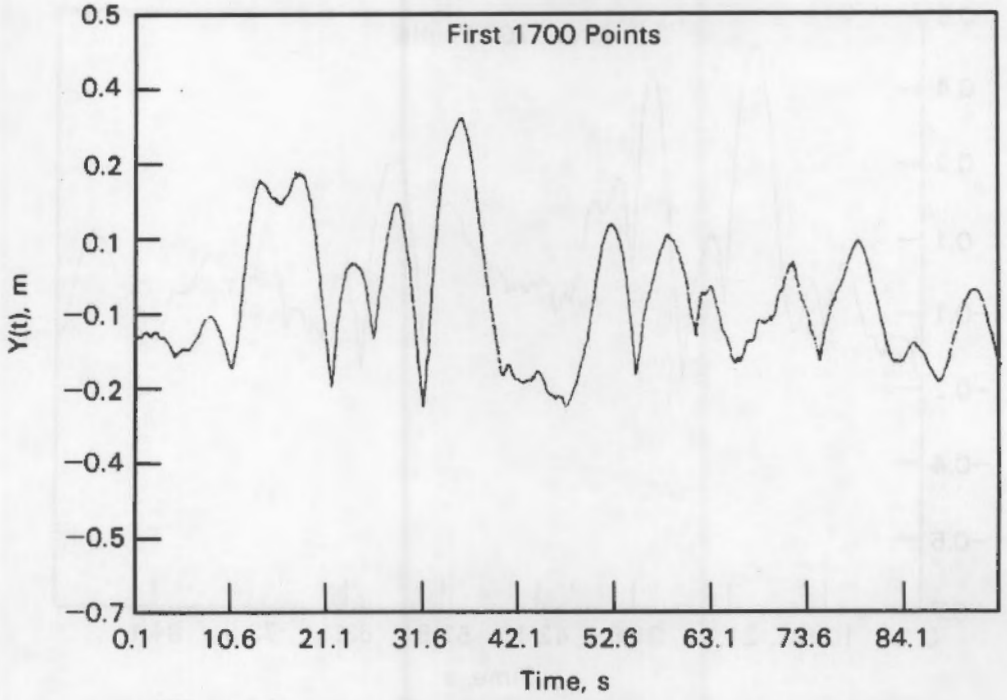

FIGURE 6.11. Balloon Displacement, Y(t) Time Series, First 1700 Points

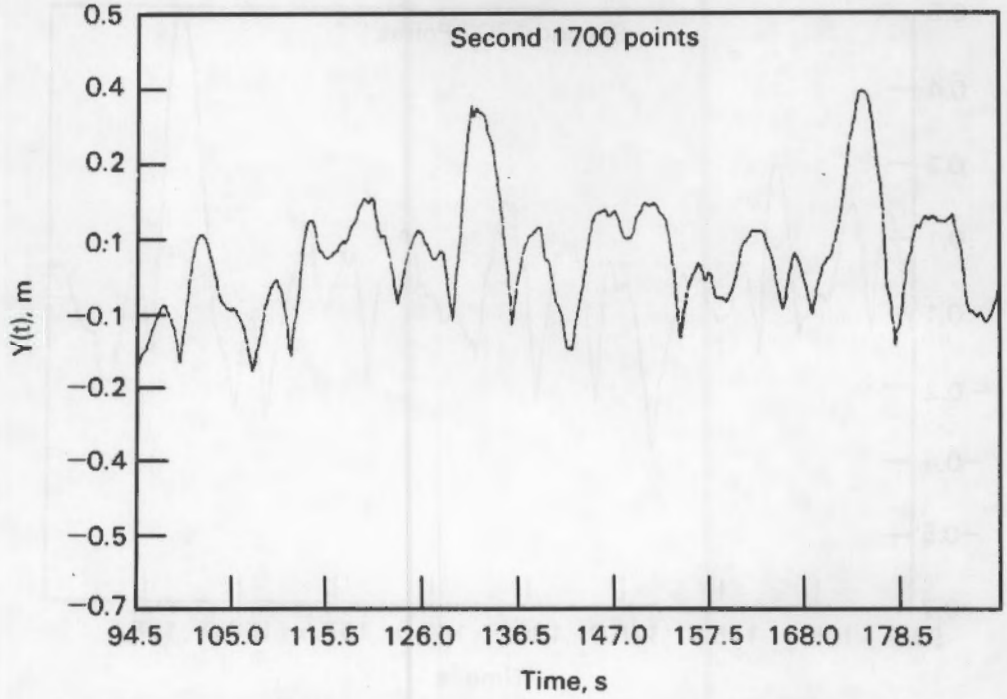

FIGURE 6.12. Balloon Displacement, Y(t) Time Series, Second 1700 Points

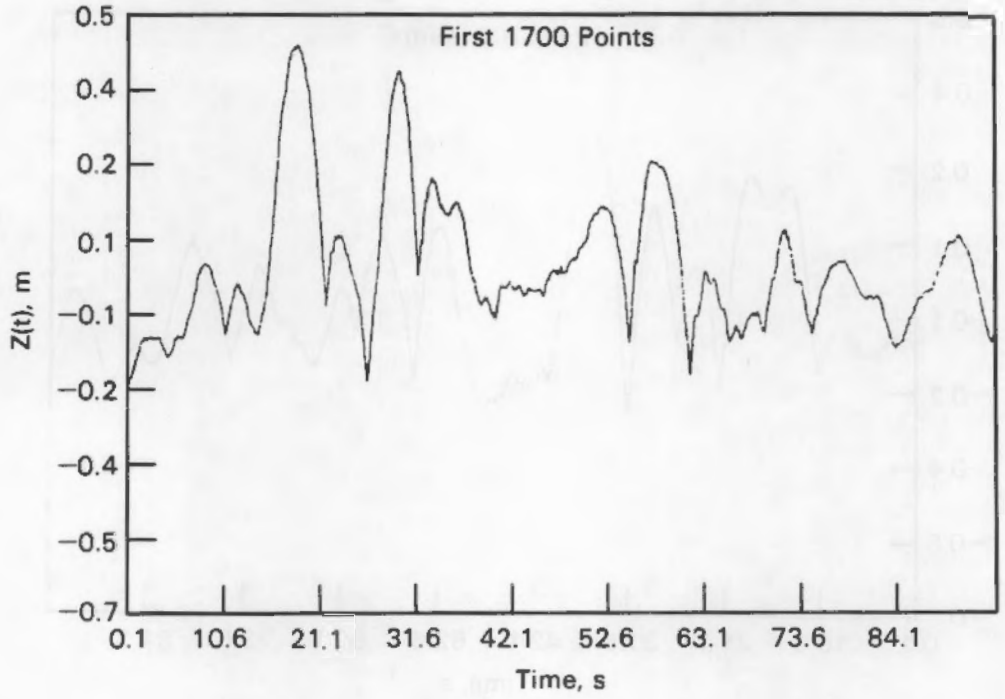

FIGURE 6.13. Balloon Displacement, Z(t) Time Series, First 1700 Points

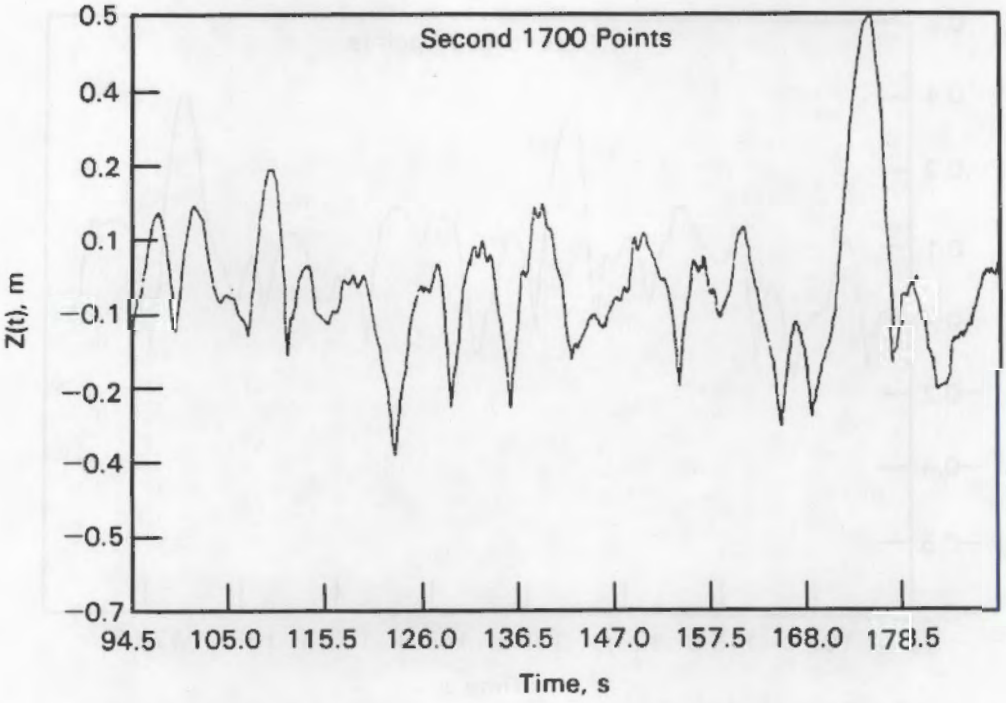

FIGURE 6.14. Balloon Displacement, Z(t) Time Series, Second 1700 Points

TABLE 6.4. Mean and Standard Deviation of New Zeroed Balloon Displacement Series

	X(t), m	Y(t), m	Z(t), m
Mean	0.0000	0.0000	0.0000
S.D.	0.1879	0.1333	0.1438

TABLE 6.5. Mean and Standard Deviation Balloon Velocity

Mean, m/s	Standard Deviation, m/s
0.0007855	0.271576

As mentioned in Chapter 5, the kite sometimes left the field of view of the camera, which affected the values of the kite displacement time series calculated from the digitized kite data. The balloon film also shows that the balloon sometimes left the view of the camera; this fact is considered to be the main reason of having nonzero mean balloon velocity values.

Equation (5.4) was used to find the magnitude of the balloon velocity for each time step, and the results for the run were plotted as time series in Figures 6.15 and 6.16. Figures 6.15 and 6.16 appear to contain much more high-frequency information than did the displacement plots in Figures 6.9 through 6.14.

Figures 6.17 and 6.18 are the spectral analysis results of the new zeroed balloon displacement time series in the X direction. Figures 6.17 and 6.18 have a dominant frequency at about 0.08 Hz. Figures 6.19 and 6.20 are the spectral analysis results of the balloon's velocity, V(t). The peak of 0.18 Hz in both Figures 6.19 and 6.20 is more than twice as much as the peak in Figures 6.17 and 6.18 of the X(t). The comparison in frequency between Figures 6.17, 6.18, 6.19, and 6.20 and the comparison between Figures 6.19 to 6.14 and 6.15 to 6.16 are indicating that the dominant frequency of the balloon velocity is much higher than the dominant frequency of the balloon's displacements.

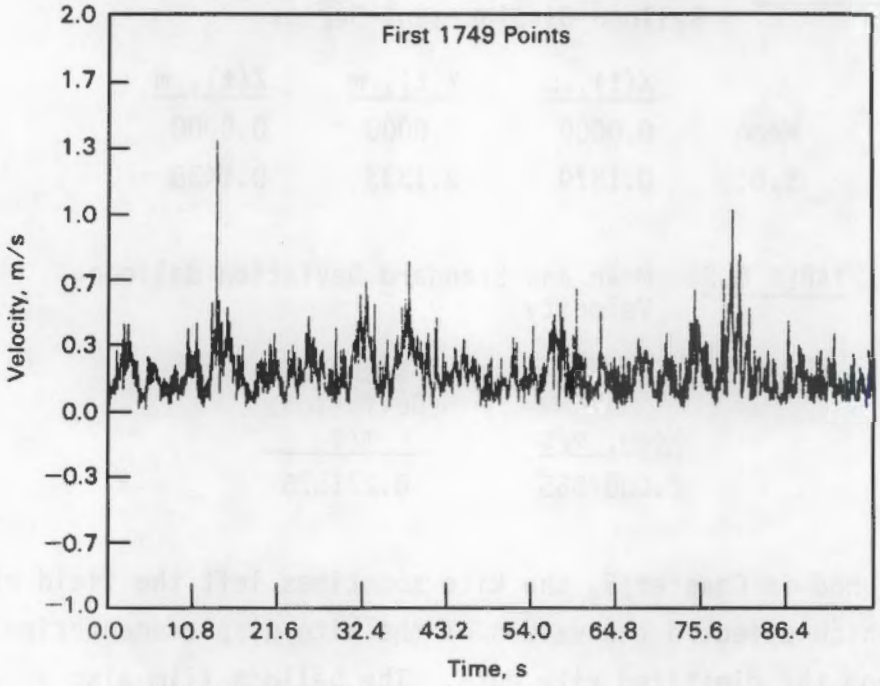

FIGURE 6.15. Balloon Velocity Time Series, First Part, 1749 Points

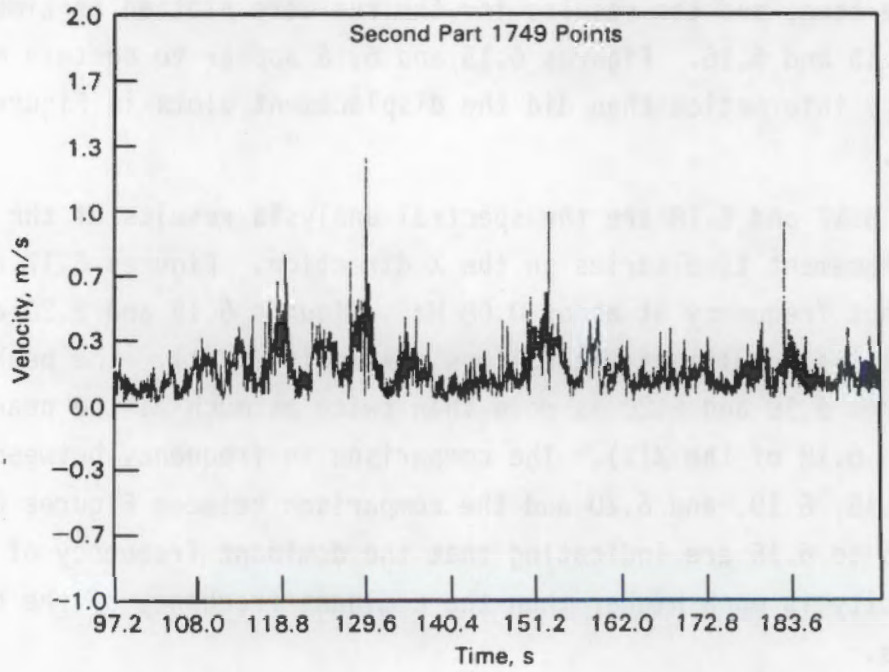

FIGURE 6.16. Balloon Velocity Time Series, Second Part, 1749 Points

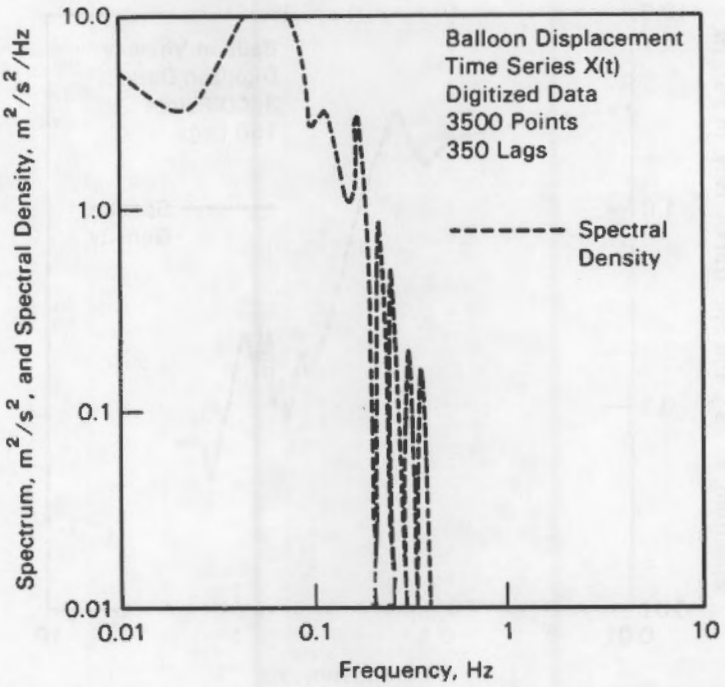

FIGURE 6.17. Log-Log Plot of Spectral Density Against Frequency, Balloon Displacement Time Series X(t), 350 Lags

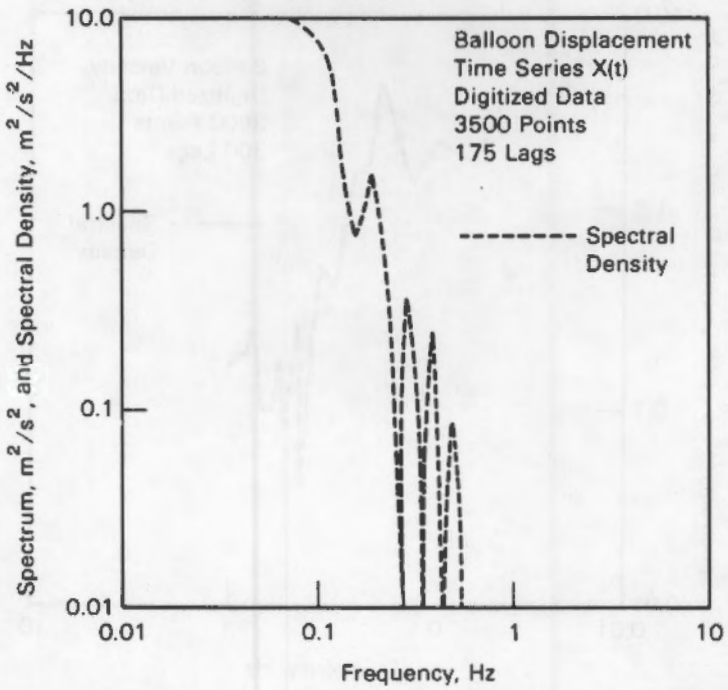

FIGURE 6.18. Log-Log Plot of Spectral Density Against Frequency, Balloon Displacement Time Series X(t), 175 Lags

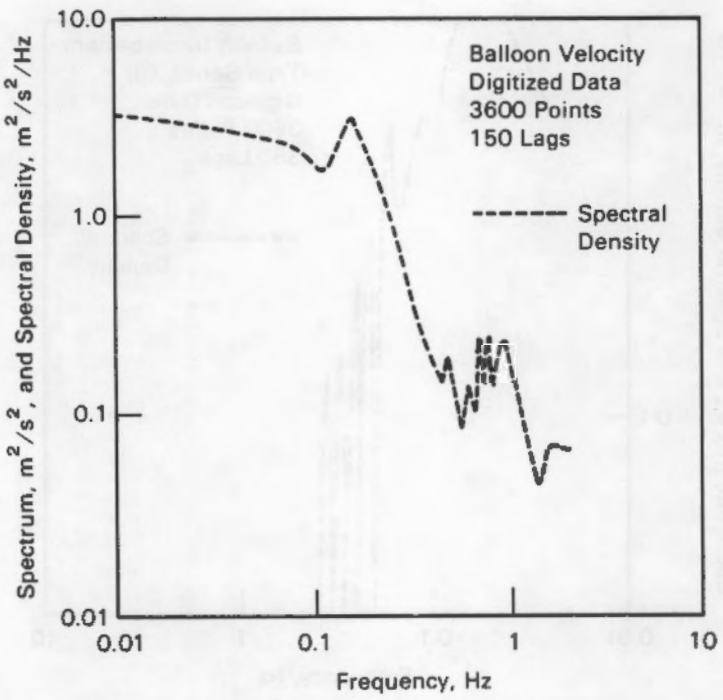

FIGURE 6.19. Log-Log Plot of Spectral Density Against Frequency, Balloon Velocity, 150 Lags

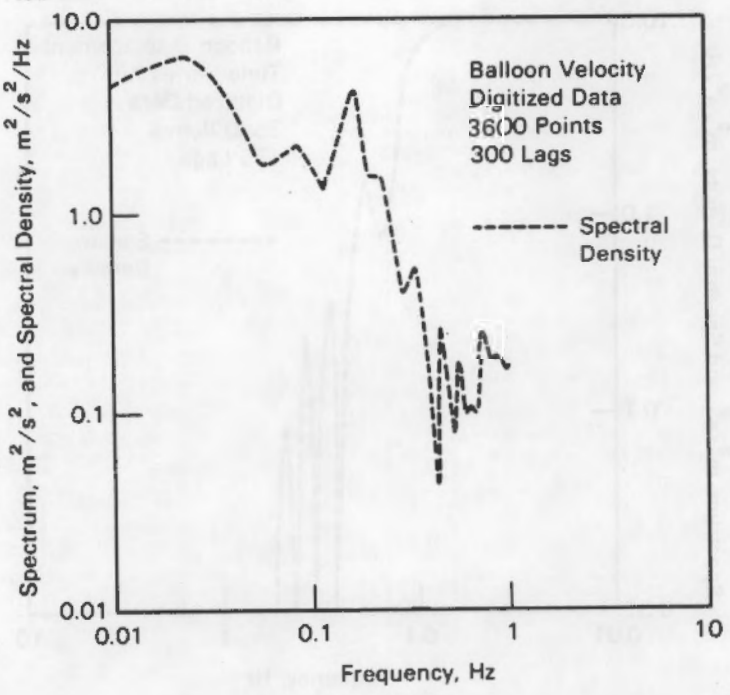

FIGURE 6.20. Log-Log Plot of Spectral Density Against Frequency, Balloon Velocity, 300 Lags

The two films taken at 14:20 (Run 2) were reexamined from Cameras A and B separately to see whether the frequencies observed from the balloon displacements X(t), Y(t), and Z(t) were substantiated by estimating the frequency from the film. The periods of each trip (balloon travel back and forth once) were recorded and the average time over all the trips was calculated for each film (Table 6.6).

The averages of 14.3587 s and 14.436 s were obtained after doing the above exercises. A frequency of 0.07 Hz was then calculated from the time averages; it agrees with the peak frequency of the spectral analysis results of the time series X(t).

The unexpected higher frequency peak, 0.18 Hz, of the balloon velocity was thought to be caused by the combining of the X(t), Y(t), and Z(t) peaks in Equation (5.4). As seen in Figures 6.9 through 6.14 and the mean and standard deviation of the X(t), Y(t), and Z(t) in Table 6.3, the strong dominant motion in X direction is greater than the motion in the mean flow direction, Y(t). This matter is discussed in the conclusion, Section 6.3.

TABLE 6.6. Durations of Average Time for a Balloon Trip

Camera A		Camera B	
Trip No.	Time, s	Trip No.	Time, s
1	10.33	1	10.44
2	15.05	2	16.72
3	12.78	3	13.11
4	16.72	4	11.38
5	14.22	5	12.11
6	12.28	6	17.33
7	12.83	7	12.67
8	12.06	8	10.66
9	16.22	9	12.61
10	12.67	10	19.56
11	16.89	11	13.56
12	24.83	12	22.33
13	9.78	13	15.17

The motion of the balloon is now compared with the theory developed in Chapter 4. As in Figure 4.3a, the angle of attack (α) and the vertical turbulence parameter (v) were assumed to be zero. Equation (4.15) was introduced as the response equation of the balloon under those conditions.

$$\theta_1' = \frac{-2\tan\theta_1 \frac{u}{U}}{\sec^2\theta_1\left(1 + \frac{2u}{U}\right)} . \qquad (4.15)$$

In Figure 4.3b, an angle of attack and a vertical turbulence parameter, v, were included, yielding Equation (4.20).

$$\theta' = \frac{\left(\frac{C_l}{C_d} - \tan\theta_1\right)\left(\frac{2u}{U}\right) + \left(\frac{C_{l,\alpha}}{C_d} - \frac{C_{d,\alpha}}{C_d}\tan\theta_1\right)\left(\frac{v}{U}\right)}{\left(\tan\theta_1 \frac{C_{d,\alpha}}{C_d} + \sec^2\theta_1 - \frac{C_{l,\alpha}}{C_d}\right)\left(1 + \frac{2u}{U}\right) + \frac{C_{d,\alpha}}{C_d}\sec^2\theta_1\left(\frac{v}{U}\right)} . \qquad (4.20)$$

In this analysis, Equations (4.15) and (4.20) are called the simple and the complex equations, respectively; for convenience they are Equations (4.15) and (5.3).

Because the length of the tetherline of the balloon is known and the fluctuating elevation angle could be calculated from Equations (4.15) or (4.20), then the displacement can be determined as the length of the tether multiplied by the fluctuating elevation angle in radians.

Values for C_l, C_d, $C_{l,\alpha}$, and $C_{d,\alpha}$ were obtained from Lang (1948); they are 0.0598, 0.0363, 0.4383, and 0.0845, respectively. The length of the tether and the mean elevation angle were given by PNL as 15.48 m and 88°.

The balloon displacement results calculated from Equations (4.15) and (4.20) are listed in Table 6.7. The balloon displacement results obtained by the simple theory and the complex theory are compared with the displacement calculated from the digitized balloon data. Tables 6.3 and 6.4 showed that the balloon's fluctuating displacement in the mean flow direction, Y, is equal to 0.1334 m, very close to the balloon fluctuating displacement calculated

TABLE 6.7. Balloon Displacement Calculated by the Simple and Complex Balloon Theories

	Displacement, m
Simple Theory	0.14
Complex Theory	0.14

from the theory (0.14 m). The excellent agreement supports the fact that both the simple and the complex theory are capable of predicting the balloon's fluctuating motion in a turbulent wind field.

6.3 CONCLUSIONS

Displacement results of the simple and complex theories of balloon movement presented in Chapter 4 are very close. These theoretical results generally agree with the experimental result. Despite the unexpected high-frequency peak one sees in Figures 6.9 through 6.14 and the huge displacement in the lateral direction in Table 6.3, which are believed to be caused by the combination of the three X, Y, and Z peaks and the wind effect on the side of the balloon, respectively, the small perturbation analysis of the balloon response to turbulence works quite well on a aerodynamically shaped balloon. The agreement between theoretical and experimental balloon displacement results substantiated the result obtained by the extended double theodolite theory.

7.0 REFERENCES

Baker, R., R. L. Whitney and E. W. Hewson. 1979. "A Low Level Wind Measurement Technique for Wind Turbine Generator Siting." Wind Engineering 3(2):107-112.

Bearman, P. W. 1984. "Vortex Shedding from Oscillating Bluff Bodies." Ann. Rev. Fluid Mech. 16:195-222.

Connell, J. R. 1982. "The Spectrum of Wind Speed Fluctuations Encountered by a Rotating Blade of a Wind Energy Conversion System." J. of Solar Energy 29(5):363-375.

Corrsin, S. 1963. "Turbulence: Experimental Methods." Handb. Phys. 8(2):523-590, Berlin, Springer.

Daniels, P. A. 1984. "Turbulence Analysis of Kite Wind Measurements." In Proceedings of the European Wind Energy Conference, pp. 91-95. Hamburg, Federal Republic of Germany.

Hoerner, S. F. 1965. Fluid-Dynamic Drag. Published by Author, Midland Park, New Jersey.

Hoerner, S. F. 1975. Fluid-Dynamic Lift. Published by Mrs. Liselotte A. Hoerner, Midland Park, New Jersey.

Huang, K. H., C. F. Shieh and W. Frost. 1981. Analysis of a Kite Anemometer. Final Report, FWG Associates, Inc., Tullahoma, Tennessee, 62 pp.

Kirchhoff, R. H. 1985. Potential Flow: Computer Graphic Solutions. Marcel Dekker, Inc., New York and Basel.

Kirchhoff, R. H., and F. C. Kaminsky. 1983. "Wind Measurements and Synoptic Weather Categories for Siting Large Wind Turbine." J. of Wind Engineering and Industrial Aerodynamics 15:287-297.

Kirchhoff, R. H., and R. Safarik. 1974. "Turbulence Calibration of a Hot Wire Anemometer." AIAA Journal 12(5):710-711.

Knowles, W. E., and A. F. Spilhaus. 1953. "Meteorological Instruments." University of Toronto Press 3:181-188.

Kunkel, K. E. 1981. Evaluation of a Tethered Kite Anemometer. ASL-TR-0076, U.S. Army Electronic R&D Command, Atmospheric Sciences Laboratory, White Sands, New Mexico.

Lang, G. 1948. "Force and Pressure-Distribution Measurements on Eight Fuselages." National Advisory Committee for Aeronautics Technical Memorandum, Washington, D.C.

Lumley, J. L., and H. A. Panofsky. 1964. The Structure of Atmospheric Turbulence. Interscience, New York.

Shieh, C. F., and Walter Frost. 1980. "Tether Analysis for a Kite Anemometer." Wind Engineering 4(2):80-86.

Teunissen, H. W. 1970. Characteristics of the Mean Wind Turbulence in the Planetary Boundary Layer. Institute for Aerospace Studies, University of Toronto.

Thrall, T., and L. Engelman. 1976. Time Series Analysis. Prentice Hall, Inc., Englewood Cliffs, New Jersey.

APPENDIX A

FEATURES AND APPLICATIONS OF THE TALA KITE

APPENDIX A

FEATURES AND APPLICATIONS OF THE TALA KITE

The Tethered Aerodynamically Lifting Anemometer (TALA)® is a recently patented anemometer. Wind speed is measured as a function of the tension on the tether line of an airfoil or kite. The TALA models in production are hand-held instruments, and the accessory data acquisition system is a highly portable electronic version that records speed, direction, and altitude information. The data acquisition system requires an operator.

It is possible for a single technician to record wind speed, direction, and altitude information up to 250 m above ground level. Data are visually read and dictated into a portable tape recorder. A recording strain gauge in the handle of the TALA model records speed information only.

Many wind measurement applications exist. Periodic profiles at low-level anemometer sites yield statistical data for calculating upper winds. Environmental impact statements for proposed construction sites can economically include information on planetary boundary layers and transport winds. Site evaluation for wind power research is facilitated. Applications possible using multiple field units include: generation of vertical profiles of particular geographic areas; production of visual wind vectors; and mapping of wind vectors in the vicinity of buildings and terrain.

®Approach Fish, Inc., Clifton Forge, Virginia.

APPENDIX B

FEATURES AND APPLICATIONS OF THE TETHERSONDE BALLOON

APPENDIX B

FEATURES AND APPLICATIONS OF THE TETHERSONDE BALLOON

The TS-1BR-X balloon was developed specifically to serve as a vehicle for the TS-1A Tethersonde™ tethered balloon sounding system. It has years of proven field research in every part of the world.

The balloon is fabricated with 1.5 mil (0.038 mm) urethane plastic. The payload-to-volume ratio is about four times that attained with tethered balloons of conventional material. The light, strong construction of the balloon results in fewer handling problems in turbulent launch and recovery situations, and reduces the volume of helium or hydrogen required for inflating. The balloon is designed to automatically compensate for the change in external pressure with normal ascent. The unique internal stretch cord and expansion stinger allow the balloon to maintain its aerodynamic shape and present a low drag coefficient at any rated altitude and wind load.

The inflation tube is mounted in the nose of the balloon. This allows an operator to inflate and deflate the balloon while controlling the tether point in the prevailing wind, a decided advantage for one-person operation in gusty turbulent winds.

The TS-1BR-X can operate in a wide temperature range. It can be flown as high as 1.5 km. The mass of the balloon ranges from 1 to 2 kg.

Potential applications of the tethersonde include:

- portable meteorological tower
- air pollution sensor platform
- radar target platform
- point source (stack) aerosol simulation
- boundary layer research.

APPENDIX C

LITERATURE SEARCH - REFERENCE LIST

(Alphabetized by Reference Title)

APPENDIX C

LITERATURE SEARCH - REFERENCE LIST

(Alphabetized by Reference Title)

1. Lin, J. T., and S. D. Veenhuizen. 1983. Airborne Wind Measurements at Cape Blanco, Oregon. United Industries Corp., Bellevue, Massachusetts.

2. Nierenberg, R. 1983. "An Innovative Wind Measurement Program Using Fixed, Mobile, and Kite Anemometers." In Proceedings of the Wind Expo'83 and AWEA National Conference, San Francisco, California, pp. 175-191.

3. Huang, K. H., C. F. Shieh and W. Frost. 1981. Analysis of a Kite Anemometer. Final Report, FWG Associates Inc., Tullahoma, Tennessee.

4. MacCready, P. B., Jr. 1977. Assessing the Local Wind Field for Siting of Wind Power System. Final Report, Aerovironment Inc., Pasadena, California.

5. Zambrano, T. G. 1980. Assessing the Local Wind Field with Instrumentation. Prepared for Pacific Northwest Laboratory, Richland, Washington, by Aerovironment Inc., Pasadena, California.

6. Vachon, W. A., W. T. Downey and F. R. Madio. 1980. "Case Study of Wind in Complex Terrain." In Proceedings of Annual Meeting of the Am. Sect. Int. Sol. Energy Soc. 3(2):1481-1485.

7. Dionne, J.(a) 1979. "Comparison of Wind Measurements from a Tower and a Balloonborne Sonde." Atmosphere-Ocean, Toronto, Canada, (Special Issue), 17:53-54.

8. Daniels, P. A., and N. E. Oshiro. 1980. Detailed Wind Survey of Kahuku, Oahu. University of Hawaii, Department of Meteorology, Honolulu, Hawaii.

9. Angell, J. K., and A. B. Bernstein. 1976. "Evidence for a Reduction in Wind Speed on the Upwind Side of a Tower." Journal of Applied Meteorology 15(2):186-188.

10. Kunkel, K. E. 1981. Evaluation of a Tethered Kite Anemometer. Atoms. Sci. Lab., University of Massachusetts, Amherst, Massachusetts.

(a) Cannot be located.

11. Kirchhoff, R. H., and F. C. Kaminsky. 1981. "Implementation of a Siting Meteorology for Utility Size WECS in Western Massachusetts and Northwestern Connecticut." AIAA Paper 81-2540.

12. Daniels, P. A., and N. E. Oshiro. 1982. Kahuku Kite Wind Study. I. Kahuku Beach Boundary Layer. Hawaii University, Department of Meteorology, Honolulu, Hawaii.

13. Daniels, P. A., and N. E. Oshiro. 1982. Kahuku Kite Wind Study. II. Kahuku Foothills. Hawaii University, Department of Meteorology, Honolulu, Hawaii.

14. Daniels, P. A. 1982. Kahuku Kite Wind Study. III. Turbulence Analysis. Hawaii University, Department of Meteorology, Honolulu, Hawaii.

15. Baker, R. W., R. L. Whitney and E. W. Hewson. 1979. "Low Level Wind Measurement Technique for Wind Turbine Generator Siting." Wind Engineering 3(2):107-114.

16. Readings, C. J., and H. E. Baker. 1972. "Measurement of Atmospheric Turbulence from a Captive Balloon." Meteorological Magazine 101(1203):286-298.

17. Tapp, R. G., and R. C. Lile. 1978. "New Tethersonde System for Remote Measurement of Wind and Temperature." Boundary Layer Meteorology 15(4):465-479.

18. Daniels, P. A. 1981. Siting a Fertilizer-Producing Windmill in Kahuku, Oahu. Hawaii University, Department of Meteorology, Honolulu, Hawaii.

19. Zambrano, T. G., and P. B. S. Lissaman. 1981. "Site Prospecting Techniques for Large Wind Turbine: Case Example--Southwest Tehachapi Mountain Region, California." In Proceedings of the Fifth Biennial Wind Energy Conference and Workshop, pp. 673-687. Solar Energy Research Institute, Golden, Colorado.

20. Hussan, U. 1980. Special Purpose Anemometry for Wind Power Studies. ERA Technol Ltd., Multi-Sci. Publishing Co. Ltd., London, England, pp. 186-193.

21. Kaimal, J. C., J. E. Gaynor and H. W. Baynton. 1980. Summary of Results. Preprint of WMO Report, Boulder, Colorado, pp. 153-189.

22. Daniels, P. A., B. E. Palmer, T. G. Tarlton and T. A. Schroeder. 1976. Survey of the Wind on the Island of Maui for Potential Wind Power Generation, Part 1, Mobile Sample Program, August 7-26, 1976. Hawaii University, Department of Meteorology, Honolulu, Hawaii.

23. Woodhouse, C. F. 1980. Tethered Aerodynamically Lifting Anemometer (TALA). Approach Fish, Inc., Clifton Forge, Virginia, pp. 33-37.

24. Shieh, C. F., and W. Frost. 1980. "Tether Analysis for a Kite Anemometer." Wind Engineering 4(2):80-86.

25. Morris, A. L., and D. B. Call. 1980. Tethersonde System. Ambient Analysis, Inc., Boulder, Colorado, pp. 117-124.

26. Baker, R. W., and S. N. Walker. 1984. "Wake Measurements Behind a Large Horizontal-Axis Wind Turbine Generator." Solar Energy 33(1):5-12.

27. Lissaman, P. B. S., T. G. Zambrano and G. W. Gyatt. 1983. Wake Structure Measurements at the MOD-2 Cluster Test Facility at Goodnoe Hills. Aerovironment, Inc., Pasadena, California.

28. Baker, R. W., S. N. Walker and P. C. Katen. 1984. Wake Studies at the FloWind Vertical Axis Wind Turbine Generator Site. Oregon State University, Department of Atmsopheric Science, Corvallis, Oregon.

29. Baker, R. W., and S. N. Walker. 1982. Wake Studies at the Goodnoe Hills MOD-2 Site. Oregon State University, Department of Atmsopheric Science, Corvallis, Oregon.

30. Wade, J. E., R. W. Baker and P. C. Katen. 1984. Wind Energy Assessment Studies in the Cape Blanco Area. Progress Report, October 1982 Through September 1983, Final Report, Oregon State University, Department of Atmospheric Science, Corvallis, Oregon.

31. Cromack, D., J. McGowan and R. H. Kirchhoff. 1982. "Wind Energy Siting for the Utilities." Am. Soc. Mech. Engrs., pp. 197-211.

APPENDIX D

PROGRAM FINDLO LISTING

APPENDIX D

PROGRAM FINDLO LISTING

```
00010C*************************************************************************
00020C*   THIS PROGRAM READS TWO SETS OF THE DIGITIZED KITE OR          *
00030C*   BALLOON DATA.  EXTENDED DOUBLE THEODOLITE THEORY IS           *
00040C*   EMPLOYED TO CALCULATE KITE OR BALLOON'S DISPLACEMENTS         *
00050C*   IN X, Y, Z COORDINATES FOR EVERY TIME STEPS THROUGHOUT        *
00060C*   THE WHOLE TIME SERIES.                                        *
00070C*************************************************************************
00080C
00090 PROGRAM FINDLO(INPUT, OUTPUT, TAPE99, TAPE98, TAPE511, TAPE512,
00100+TAPE513)
00110C
00120C*************************************************************************
00130C*  TAPE99 AND TAPE98 ARE THE TWO INPUT DATA FILES AND TAPE 511    *
00140C*  THROUGH TAPE 513 ARE THE OUTPUT DATA FILES FOR X, Y, Z         *
00150C*  RESPECTIVELY.
00160C*************************************************************************
00170C
00180 REAL X(0:3600), Y(0:3600), Z(0:3600)
00190 X(0)=0.0
00200 Y(0)=0.0
00210 Z(0)=0.0
00220C
00230C*************************************************************************
```

```
00240C*   INITIAL ELEVATION AND AZIMUTH ANGLES AT THE TWO OBSERVING     *
00250C*   POINTS AND THE DISTANCE BETWEEN THE TWO POINTS ARE            *
00260C*   BEING READ HERE.
00270C*************************************************************************
00280C
00290 PRINT*,'INPUT ELEVATION AND AZIMUTH ANGLES'
00300 PRINT*,'THI1, THI2, THETAA, THETAB'
00320 PI=3.1415926
00330 THETA1=THETAA*2*PI/360
00340 THETA2=THETAB*2*PI/360
00360 THI1=THIA*2*PI/360
00370 THI2=THIB*2*PI/360
00380 PRINT*,'INPUT DISTANCE BETWEEN THE TWO OBSERVE POINTS'
00390 READ*,L
00400C
00410C*************************************************************************
00420C*  INITIAL KITE OR BALLOON POSITION IN X, Y, Z COORDINATES ARE    *
00430C*  CALCULATED ACCORDING TO THE DOUBLE THEODOLITE THEORY AS         *
00440C*  AG, GOP, OOP RESPECTIVELY (SEE FIGURE 2).  DISTANCE BETWEEN    *
00450C*  OTHER POINTS IN FIGURE 2 ARE ALSO CALCULATED.                   *
00460C*************************************************************************
00470C
00480 AG=L/(1+TAN(THETA1)/TAN(THETA2))
00490 OOP=L*SIN(THETA2)*TAN(THI1)/SIN(PI-THETA1-THETA2)
```

```
00500 GOP=L*SIN(THETA2)*SIN(THETA1)/SIN(PI-THETA1-THETA2)
00510 AOP=(AG**2+GOP**2)**0.5
00520 AO=(AOP**2+OOP**2)**0.5
00530 GB=L-AG
00540 BOP=(GB**2+GOP**2)**0.5
00550 BO=(OOP**2+BOP**2)**0.5
00560 GO=(AO**2-AG**2)**0.5
00570 OMEGA1=ATAN(GO/AG)
00580 OMEGA2=ATAN(GO/GB)
00590C
00600C*************************************************************************
00610C*   ANGLE C BETWEEN X" AND X' IS CALCULATED                             *
00620C*************************************************************************
00630C
00640 AOB=PI-OMEGA1-OMEGA2
00650 IF(AOB.LT.(PI/2)) THEN
00660   C=OMEGA1+OMEGA2-P1/2
00670      ELSE IF(AOB.GT.(PI/2)) THEN
00680         C=PI/2-OMEGA1-OMEGA2
00690            ELSE
00700          C=0.0
00710       ENDIF
00720 ENDIF
00730 PRINT*,'INPUT THE FOCAL LENGTH FL'
00740 READ*,FL
```

```
00750 FACT1=0.0262*(AO-FL)/(23*39.37*FL)
00760 FACT2=0.0262*(BO-FL)/(23*39.37*FL)
00770C
00780C*************************************************************************
00790C*   THE RATIO OF THE OBJECT SIZE ON THE 8 MM (0.0262 M) FILM      *
00800C*   WITH THE DIGITIZING BOARD IS CALCULATED AS FACT1 AND FACT2     *
00810C*   FOR THE TWO FILMS.  23 INCH IS THE WIDTH OF THE DIGITIZING     *
00820C*   BOARD IN THIS CASE.
00830C*************************************************************************
00840C
00850C*************************************************************************
00860C*   ACCORDING TO TABLE 1 IN CHAPTER I, DIGITIZED DATA IN X", Y"    *
00870C*   Z" SYSTEM IS TRANSLATED INTO X', Y', Z' SYSTEM AND THE KITE    *
00880C*   OR BALLOON'S LOCATION IN X, Y, Z COORDINATES IS CALCULATED.    *
00890C*   FINALLY, THE KITE OR BALLOON'S DISPLACEMENT FOR EACH TIME      *
00900C*   STEP IS THEREFORE DETERMINED.                                  *
00910C*************************************************************************
00920C
00930 PRINT*,'INPUT THE NUMBER OF DIGITIZED DATA POINTS, N'
00940 READ*,N
00950 DO 4 I=1,N
00960 READ(99,15)ZPAA,YPA
00970 15 FORMAT(2(F11.3))
00980 YP=ZPAA*FACT1
00990 ZP1=YPA*FACT1
```

```
01000 READ(98,20)ZPB,XPPA
01100 XPP=ZPB*FACT2
01110 XPP=ZPB*FACT2
01120 ZP2=XPPA*FACT2
01130 ZAP=(ZP1+ZP2)/2
01140 IF (XPP.GT.0.0) THEN
01150 XP=XPP/COS(C)-YP*TAN(C)
01160    AJ=AO+XP
01170       ELSE IF(XPP.LE.0.0)THEN
01180           XP=XPP/COS(C)+YP*TAN(C)
01190       AJ=AO-XP
01200     ENDIF
01210 ENDIF
01220 A=ATAN(YP/AJ)
01230 AK=(YP**2+AJ**2)**0.5
01240 B=ATAN(ZAP/AK)
01250 AH=(AK**2+ZAP**2)**0.5
01260 X(I)=AH*COS(THI1+B)*COS(THETA1-A)-X(1)
01270 Y(I)=AH*COS(THI1+B)*SIN(THETA1-A)-Y(1)
01280 Z(I)=AH*SIN(THI1+B)-Z(1)
01290 WRITE(511,50)DT,X(I)
01300 50 FORMAT(5X,2(E13.6))
01310 WRITE(512,51)DT,Y(I)
01320 51 FORMAT(5X,2(E13.6))
01330 WRITE(513,52)DT,Z(I)
```

```
01340 52 FORMAT(5X,2(E13.6))
01350 DT=DT+0.5
01360 4 CONTINUE
01370 STOP
01380 END
```

APPENDIX E

DERIVATION OF EQUATION (3.16)

APPENDIX E

DERIVATION OF EQUATION (3.16)

Steady-state diagram of the kite (Figure 3.1) gives

$$F_l = F_d \tan\theta \tag{3.13}$$

and as declared earlier,

$$F_l = 1/2\rho A C_l (U^2 + 2Uu + u^2 + v^2)$$

$$F_d = 1/2\rho A C_d (U^2 + 2Uu + u^2 + v^2)$$

$$C_l = C_l + C_{l,\alpha}\alpha'$$

$$C_d = C_d + C_{d,\alpha}\alpha'$$

plus,

$$\alpha' = \theta' + \frac{v}{U}$$

$$\theta = \theta + \theta'$$

now substitute all those terms into Equation (3.13), and Equation (3.13) becomes:

$$1/2\rho A C_l (U^2 + 2Uu + u^2 + v^2) + 1/2\rho A C_{l,\alpha} (U^2 + 2Uu + u^2 + v^2)(\theta' + \frac{v}{U}) =$$
$$\tan\theta\ 1/2\rho A C_d (U^2 + 2Uu + u^2 + v^2) + \tan\theta\ 1/2\rho A C_{d,\alpha} (U^2 + 2Uu + u^2 + v^2)$$
$$(\theta' + \frac{v}{U}) + \sec^2(\theta)\theta'\ 1/2\rho A C_d (U^2 + 2Uu + u^2 + v^2) + \sec^2(\theta)\theta'$$
$$1/2\rho A C_{d,\alpha} (U^2 + 2Uu + u^2 + v^2)(\theta' + \frac{v}{U}) \qquad \text{Step 1}$$

divide Step 1 by U^2, Step 1 becomes,

$$1/2\rho AC_l U^2\left(\frac{2u}{U} + \frac{v^2 + u^2}{U^2}\right) + 1/2\rho AC_{l,\alpha} U^2\left(1 + \frac{2u}{U} + \frac{u^2 + v^2}{U^2}\right)\left(\theta' + \frac{v}{U}\right) = \tan\theta$$

$$1/2\rho AC_d U^2\left(\frac{2u}{U} + \frac{u^2 + v^2}{U^2}\right) + \tan\theta\ 1/2\rho AC_{d,\alpha} U^2\left(1 + \frac{2u}{U} + \frac{u^2 + v^2}{U^2}\right)\left(\theta' + \frac{v}{U}\right)$$

$$+ \sec(\theta)\theta'\ 1/2\ AC_d U^2\left(1 + \frac{2u}{U} + \frac{u^2 + v^2}{U^2}\right) + \sec^2(\theta)\theta'\ 1/2\ AC_{d,\alpha}$$

$$U^2\left(1 + \frac{2u}{U} + \frac{u^2 + v^2}{U^2}\right)\left(\theta' + \frac{v}{U}\right) \qquad \text{Step 2}$$

high order term $\frac{u^2 + v^2}{U^2}$ is dropped from Step 2,

$$1/2\rho AC_l U^2\left(\frac{2u}{U}\right) + 1/2\rho AC_{l,\alpha} U^2\left(1 + \frac{2u}{U}\right)\theta' + 1/2\rho AC_{l,\alpha} U^2\left(\frac{v}{U} + \frac{2vu}{U^2}\right) =$$

$$\tan\theta\ 1/2\rho AC_d U^2\left(\frac{2u}{U}\right) + \tan\theta\ 1/2\rho AC_{d,\alpha} U^2\left(1 + \frac{2u}{U}\right)\theta' + \tan\theta\ 1/2\rho AC_{d,\alpha}$$

$$U^2\left(1 + \frac{2u}{U}\right)\frac{v}{U} + \sec^2(\theta)\theta'\ 1/2\rho AC_d U^2\left(1 + \frac{2u}{U}\right) + \sec^2(\theta)\ 1/2\rho AC_{d,\alpha}$$

$$U^2\left(1 + \frac{2u}{U}\right)(\theta'^2) + \sec^2(\theta)\ 1/2\rho AC_{d,\alpha} U^2\left(\frac{v}{U} + \frac{2uv}{U^2}\right)\theta' \qquad \text{Step 3}$$

similar terms are added, and Step 3 becomes

$$1/2\rho AC_l U^2\left(\frac{2u}{U}\right) + 1/2\rho AC_{l,\alpha} U^2\left(\frac{v}{U} + \frac{2uv}{U^2}\right) - \tan\theta\ 1/2\rho AC_d U^2\left(\frac{2u}{U}\right) - \tan\theta$$

$$1/2\rho AC_{d,\alpha} U^2\left(1 + \frac{2u}{U}\right)\frac{v}{U} = \tan\theta\ 1/2\rho AC_{d,\alpha} U^2\left(1 + \frac{2u}{U}\right)\theta' + \sec^2(\theta)\theta'$$

$$1/2\rho AC_d U^2\left(1 + \frac{2u}{U}\right) + \sec^2(\theta)\ 1/2\rho AC_{d,\alpha} U^2\left(1 + \frac{2u}{U}\right)\theta'^2$$

$$+ \sec^2\theta\ 1/2\rho AC_{d,\alpha} U^2\left(\frac{v}{U} + \frac{2uv}{U^2}\right)\theta' \qquad \text{Step 4}$$

from here, high order term $\frac{2uv}{U^2}$ will be droped and the terms $1/2\rho AC_l U^2$ and $1/2\rho AC_d U^2$ will be called as ${}^{U^2}F_l$ and F_d, respectively,

$$F_l \frac{2u}{U} + F_l \frac{C_{l,\alpha}}{C_l} \left(\frac{v}{U}\right) - F_d \tan\theta \frac{2u}{U} - \tan\theta\, F_d \frac{C_{d,\alpha}}{C_d} \left(\frac{v}{U}\right) = F_d \tan\theta \frac{C_{d,\alpha}}{C_d}$$

$$(1 + \frac{2u}{U})\theta' + F_d \sec^2\theta (1 + \frac{2u}{U})\theta' + F_d \frac{C_{d,\alpha}}{C_d} \sec^2\theta (1 + \frac{2u}{U})(\theta'^2)$$

$$+ F_d \frac{C_{d,\alpha}}{C_d} \sec^2\theta (\frac{v}{U})\theta' - F_l \frac{C_{l,\alpha}}{C_l} (1 + \frac{2u}{U})\theta' \qquad \text{Step 5}$$

drop H.O.T. $F_d \frac{C_{d,\alpha}}{C_d} \sec^2\theta (1 + \frac{2u}{U})(\theta'^2)$, Step 5 becomes,

$$\left(F_l + F_d \tan\theta\right) \frac{2u}{U} + \left(F_l \frac{C_{l,\alpha}}{C_l} - F_d \frac{C_{d,\alpha}}{C_d} \tan\theta\right)\frac{v}{U} = \qquad \text{Step 6}$$

$$\left[F_d \tan\theta \frac{C_{d,\alpha}}{C_d} \left(1 + \frac{2u}{U}\right) + F_d \sec^2\theta \left(1 + \frac{2u}{U}\right) + F_d \frac{C_{d,\alpha}}{C_d} \sec^2\theta \frac{v}{U} - F_l \frac{C_{l,\alpha}}{C_l} \left(1 + \frac{2u}{U}\right)\right]\theta'$$

now, take Step 6 and divide F_d from both sides, we have Equation (3.16).

$$\theta' = \frac{\left(\frac{C_l}{C_d} - \tan\theta\right) \frac{2u}{U} + \left(\frac{C_{l,\alpha}}{C_d} - \frac{C_{d,\alpha}}{C_d} \tan\theta\right)\left(\frac{v}{U}\right)}{\left(\tan\theta \frac{C_{d,\alpha}}{C_d} + \sec^2\theta - \frac{C_{l,\alpha}}{C_d}\right)\left(1 + \frac{2u}{U}\right) + \frac{C_{d,\alpha}}{C_d} \sec^2\theta \left(\frac{v}{U}\right)} \qquad (3.16)$$

APPENDIX F

DERIVATION OF EQUATION (4.20)

APPENDIX F

DERIVATION OF EQUATION (4.20)

As stated in Equation (4.17),

$$F_b - mg + F_l = F_d \tan\theta_1$$

and

$$F_l = 1/2\rho A(C_l + C_{l,\alpha}(\theta' + \frac{v}{U}))(U^2 + 2uu + u^2 + v^2)$$

$$F_d = 1/2\rho A(C_d + C_{d,\alpha}(\theta' + \frac{v}{U}))(U^2 + 2Uu + u^2 + v^2)$$

$$\tan(\theta_1 + \theta_1') = \tan\theta_1 + \sec^2(\theta_1)\theta_1'$$

Since F_b and the weight mg of the balloon is constant, then if one drops the D.C. terms F_b and mg from Equation (4.17) and insert the three terms right above into Equation (4.17), one will have the same equation as Step 1 presented in Appendix E.

Following the same steps shown in Appendix E, one shall obtain Equation (4.20) without any troubles.

$$\theta' = \frac{\left(\frac{C_l}{C_d} - \tan\theta_1\right)\left(\frac{2u}{U}\right) + \left(\frac{C_{l,\alpha}}{C_d} - \frac{C_{d,\alpha}}{C_d}\tan\theta_1\right)\left(\frac{v}{U}\right)}{\left(\tan\theta_1 \frac{C_{d,\alpha}}{C_d} + \sec^2\theta_1 - \frac{C_{l,\alpha}}{C_d}\right)\left(1 + \frac{2u}{U}\right) + \frac{C_{d,\alpha}}{C_d}\sec^2\theta_1\left(\frac{v}{U}\right)} \qquad (4.20)$$

DISTRIBUTION

No. of Copies

OFFSITE

C. I. Aspliden
Battelle Memorial Institute
Washington Office
2030 M Street, NW
Washington, DC 20036

J. Cadogan
U.S. Department of Energy
Wind/Ocean Technologies Division
1000 Independence Avenue
Forrestal Building, Room 5F064
Washington, DC 20585

G. P. Tennyson
U.S. Department of Energy
Albuquerque Operations Office
P.O. Box 5400
Albuquerque, NM 87110

10 DOE/Office of Scientific and Technical Information

S. M. Chan
Systems Control, Inc.
1801 Page Mill Road
P.O. Box 10025
Palo Alto, CA 94303

R. L. George
TERRA Sciences, Inc.
7555 W. 10th Avenue
Lakewood, CO 80214

R. H. Kirchhoff
Department of Mechanical Engineering
University of Massachusetts
Amherst, MA 01003

P. Klimas
Sandia National Laboratories
Division 6225
Albuquerque, NM 87185

No. of Copies

P. M. Moretti
Oklahoma State University
Mechanical and Aerospace Engineering
Engineering North 218
Stillwater, OK 74074

D. C. Reda
Sandia National Laboratories
Division 6225
Albuquerque, NM 87185

R. B. Schlueter
Department of Electrical Engineering
Michigan State University
East Lansing, MI 48824

D. Spera
NASA/Lewis Research Center
21000 Brookpark Road
Cleveland, OH 44135

J. P. Sullivan
Aeronautics & Astronautics
Grissom Hall
Purdue University
W. Lafayette, IN 47907

R. M. Sundar
Embry-Riddle Aeronautical University
3200 N. Willow Creek Road
Prescott, AZ 86301

R. W. Thresher
Solar Energy Research Institute
1617 Cole Boulevard
Golden, CO 80401

V. A. Vachon
P.O. Box 149
Manchester, MA 01944

No. of
Copies

P. Veers
2700 Del Medio Court #304
Mountain View, CA 94040

S. N. Walker
Department of Mechanical
Engineering
Oregon State University
Corvallis, OR 97331

ONSITE

DOE Richland Operations Office

E. C. Norman/D. R. Segna

No. of
Copies

37 Pacific Northwest Laboratory

J. C. Barnard
J. R. Connell (10)
C. E. Elderkin
D. L. Elliott
J. W. Falco
M. J. Graham
J. M. Hales
P. C. Hays
R. A. Keefe (7)
V. R. Morris
E. L. Owczarski
D. C. Powell
J. A. Stottlemyre
L. L. Wendell
R. E. Wildung
Publishing Coordination
Technical Report Files (5)